CHAPTER 6: CORONAL MASS EJECTIONS AND CORONAL STRUCTURES

E. Hildner, J. Bassi, J. L. Bougeret, R. A. Duncan, D. E. Gary, T. E. Gergely, R. A. Harrison, R. A. Howard, R. M. E. Illing, B. V. Jackson, S. W. Kahler, R. Kopp, B. C. Low, P. Lantos, K. J. H. Phillips, G. Poletto, N. R. Sheeley, Jr., R. T. Stewart, Z. Svestka, P. W. Waggett, S. T. Wu.

6.1 INTRODUCTION

The coronal portion of the solar atmosphere consists of a wide variety of structures which exhibit a similarly wide variety of dynamical processes and kinds of activity. The launch of the SMM presented an opportunity to study the low and intermediate corona from space with multiple instruments for protracted periods of time. This opportunity had been lacking for years, and it was enthusiastically awaited by those interested in coronal studies. The research performed during the SMM Workshop and reported here shows how successfully the SMM and collaborative observations have been used to advance our knowledge of the corona and how these observations have stimulated our theoretical understanding of why the corona is the way we observe it to be.

This chapter intends to present the work occurring during, and as a result of, the SMM Workshop. While we have made an effort to put this work in context, not all researchers participated in the SMM workshop; it is beyond the scope of this chapter to summarize the entirety of the research performed elsewhere and to summarize the current state of knowledge of coronal mass ejections and coronal structures. For additional information, the interested reader is referred to a recent review of coronal mass ejections by Hundhausen *et al.* (1984b) and by Wagner (1984) and to the references cited therein.

Early in the Workshop, it was apparent that members of the Coronal Structures Team were interested in a variety of coronal structures and processes; however, the team members' interests centered predominantly on the coronal response to flares and, especially, the phenomenon of coronal mass ejections (CMEs). The research described in this chapter reflects the team's distribution of interests. Modelling of post-flare arches, the reconnection theory of flares, and the slow variation of coronal structure indicate the diversity of topics considered. Some team members were interested in the interplanetary detection, evolution, and consequences of mass ejections after they had propagated through the corona. The remainder of the research was focussed on the origins of CMEs and how they propagate through the corona.

Post-flare arches (Section 6.4.4) are a newly discovered phenomenon, wherein a very large coronal loop appears to undergo energization after a flare, thus allowing it to shine more brightly in X-rays. Some post-flare arches seem to be re-energized in nearly homologous fashion after each of a sequence of flares, without suffering significant disruption. The reconnection theory of flares (Section 6.4.5), in all its variants, has been a mainstay of solar physics for quite some time, but it was pointed out during the Workshop that if one analytically describes the coronal magnetic structures involved in a flare, it is possible to estimate the amount of magnetic energy available for liberation by a two-ribbon flare. Another non-CME topic was the slow variation of coronal density structures (Section 6.6.3) in the context of how the architecture of the corona slowly evolves.

Research on coronal mass ejections took a variety of forms, both observational and theoretical. On the observational side there were: case studies of individual events (Section 6.2.1), in which it was attempted to provide the most complete descriptions possible, using correlative observations in diverse wavelengths; statistical studies of the properties of CMEs (Section 6.2.2) and their associated activity; observations which may tell us about the initiation of mass ejections (Section 6.3); interplanetary observations of associated shocks and energetic particles (Section 6.5.3) — even observations of CMEs traversing interplanetary space (Section 6.5.2); and the beautiful synoptic charts which show to what degree mass ejections affect the background corona and how rapidly (if at all) the corona recovers its pre-disturbance form (Section 6.6.3).

In the five sections which follow, these efforts are described in capsule form with an emphasis on presenting pictures, graphs, and tables so that the reader can form a personal appreciation of the work and its results. The Summary, Section 6.7, highlights some of the notable results contained in earlier sections of the chapter.

6.2 OBSERVATIONS

6.2.1 Case Studies

A number of coronal transient events from the SMM period are individually of sufficient interest to be included here. These range from new observations of transients in the inner corona as low as 1.2 R_0 with the Mauna Loa (MLO) K-coronameter to reconstructions of transient brightness distributions at 0.3 AU with the Helios spacecraft. Two events observed with the HAO coronagraph/polarimeter (C/P) on SMM (MacQueen *et al.*, 1980) show unusual features that may offer insight into the physical structure and processes occurrring in transients. One of these is a "disconnection" event that has been interpreted as a pinching-off of a transient loop, so that the magnetic fields threading the transient no longer connect to the Sun. The other shows features that expand in a self-similar fashion, as predicted by Low (1982) (See Section 6.4.3). For five events, good metric radio observations exist. Such observations are important because they indicate the presence of energetic electrons and/or shock waves at the same range of coronal heights as traversed by the transient. For the first time, it is possible to associate the radio sources with identifiable distinct features within transients, enabling workers to set stricter limits on physical parameters within the sources of metric bursts of Types I, II, and IV.

6.2.1.1 5 August 1980 — An Event Observed From 1.2 to 6 R_0

Space-based coronagraphs employ an occulting disk to block the overwhelmingly bright light of the solar disk. A larger occulting disk reduces the scattered light in the outer part of the field of view so that coronal features can be observed to great heights, at the price of cutting off the inner edge of the field of view at greater height. The inner edge of the field of view of HAO's C/P was the lowest yet, down to nearly 1.5 R_0. Still, coronal transients observed with SMM appear fully formed as they emerge from below the occulting disk. During the SMM period, however, the question of how transients evolve low in the corona, near their sites of initiation, could be answered for the first time, thanks to the newly completed Mark III K-coronameter at HAO's Mauna Lao Observatory (MLO), Hawaii. The event of 5 August 1980 is one of the best observed with both MLO and SMM. The MLO event, between 1.2 and 2.2 R_0 from Sun center, is discussed by Fisher, Garcia, and Seagraves (1981, henceforth FGS). The synthesis of the MLO and SMM observations, outlined below, is described in detail by Illing, Hundhausen, and Fisher, (1985).

The MLO Mark III K-coronameter is a conventional, internally occulted coronagraph. A full description of the coronameter and associated H-alpha prominence monitor coronagraph may be found in Fisher and Poland (1981) and Fisher *et al.* (1981).

Figure 6.2.1 shows trios of pictures taken simultaneously from the SMM and MLO coronagraphs at three times early in the event. The C/P direct intensity image, the MLO polarization × brightness (pB) image, and the MLO difference (event minus pre-event) image are shown at each time. MLO's difference image at 1829 UT shows the transient as a deficit of brightness (hence, material); successive differences show the depletion to be moving outward. Although the transient was well underway in the lower corona, the SMM images show no change from the pre-event image at this time. By 1915 UT the outward-moving depletion has developed a "rim" of enhanced brightness at its flanks and top (see Figure 6.2.1b); this enhancement is a combination of additional mass from lower in the corona and pushing aside of the pre-existing streamer. The small bright feature within the depleted region (associated by FGS with the rising prominence) is seen in the MLO difference images as early as 1834 UT, and continues to rise with the surrounding depleted volume.

Figure 6.2.1c shows the event at 1959 UT, when the top has passed out of the MLO field of view but is fully within the C/P's field. Figure 6.2.2a, a schematic drawing of the transient at this time, shows that a bright loop now forms the "front" of the transient. The loop is followed by a conspicuous dark space and central bright region (P in Figure 6.2.2a). Further development of the event is shown in the lower panels of Figure 6.2.2.

The central core, P, is the remnant of the eruptive prominence seen in the prominence monitor. The dark shell seems to be the prominence cavity (as suggested by Low, Munro, and Fisher 1982), while the bright rim in the MLO field of view appears to become the bright outer loop in the C/P field of view.

A time-height plot of the important parts of the transient, as seen by both instruments, is shown in Figure 6.2.3. The lines drawn through the SMM data are least squares fits. The velocities derived from the loop data are 345 km s^{-1} for the leading edge, and 334 km s^{-1} for the trailing edge; within the experimental uncertainties, these are identical. The velocity of the prominence is considerably lower, 194 km s^{-1}. Also shown in Figure 6.2.3 are the times of occurrence of disk activity. No flares were reported in association with the eruptive prominence observed from Mauna Loa.

The initiation of the transient is consistent with the model of Low, Munro, and Fisher (1982) of an underdense volume that has become magnetically buoyant. The bright front is then presumably material swept up from the background corona. We know from the MLO data that the only mass that rises from below the occulting disk is the erupting prominence. Since the bright rim is first seen high in the MLO field of view, it cannot have originated below the occulting disk; that is, the mass must be due only to the material previously present in the background corona. We can estimate the amount of this pre-existing mass from the coronal model of Saito, Poland, and Munro (1977). The amount of mass available in a wedge 30° in latitude, 30° in longitude, and extending from 1.2 to 2 R_0, is 4.6×10^{15}g. Since the loop mass is only 0.95×10^{15}g, there is support for the the suggestion of Hildner *et al.* (1975a) that the excess material seen being ejected through a spaceborne coronagraph's field of view originated in the corona and was at coronal temperatures when the ejection began (see also Hildner *et al.*, 1975b; Schmahl and Hildner, 1977).

6.2.1.2 15-16 March 1980 — A "Disconnection" Event

This event, described in detail by Illing and Hundhausen (1983), is the first published observational evidence of an effect of magnetic reconnection suggested by many authors and summarized by MacQueen (1980) — the "pinching off" of a transient loop or bubble from the Sun. Figure 6.2.4 is a sequence of images, taken with the C/P, of a region within 45° of the solar east limb. Figure 6.2.5 shows the orientation of the images and the outlines of features of interest.

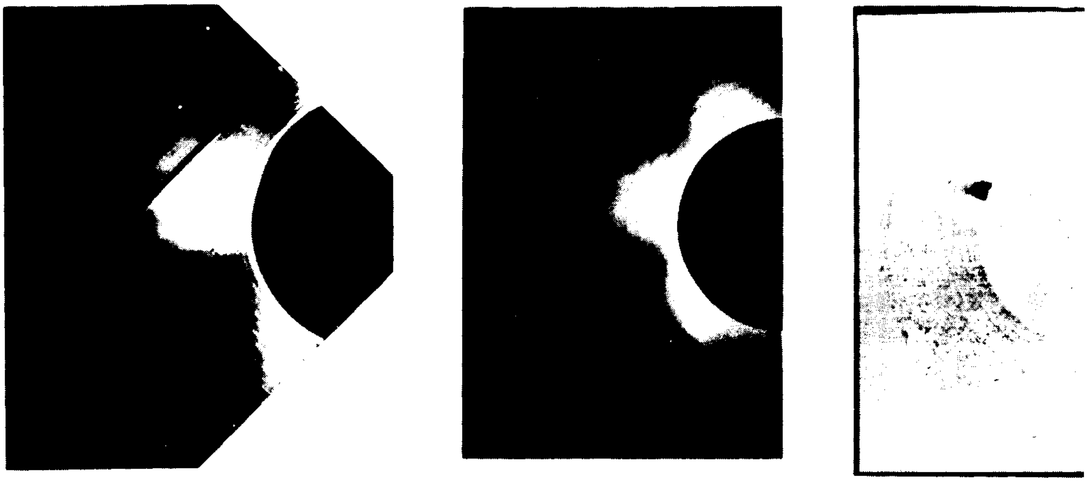

(a) 1829 UT

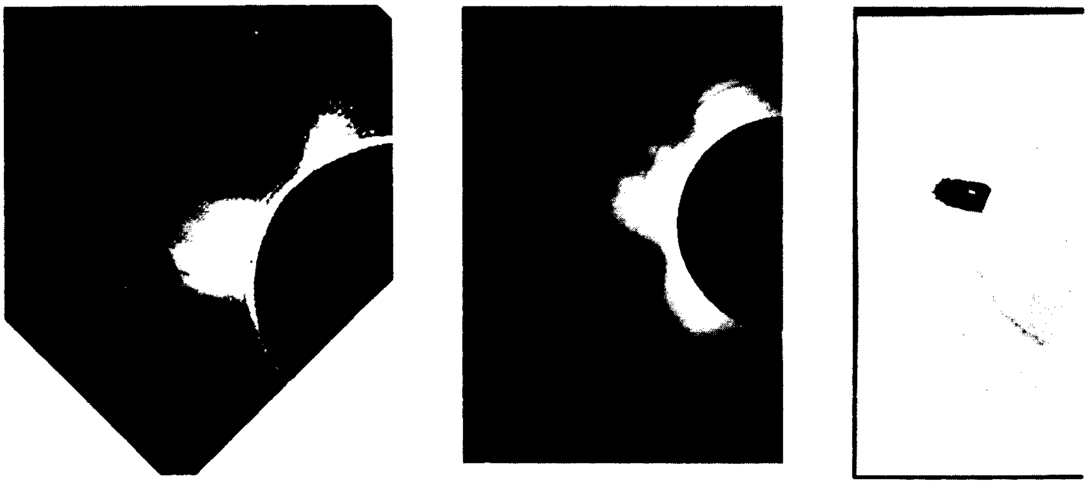

(b) 1915 UT

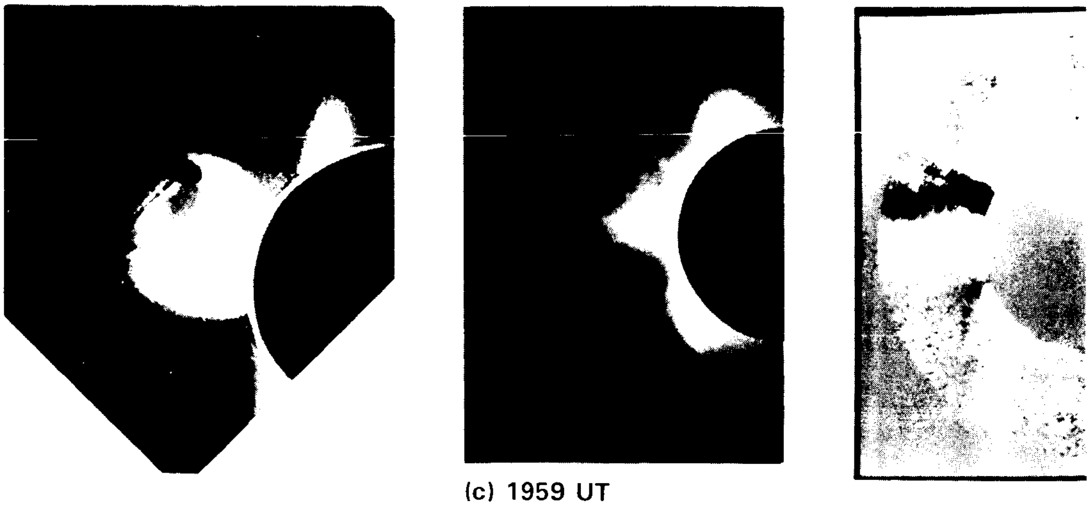

(c) 1959 UT

Figure 6.2.1 Early development of the coronal mass ejection of 5 August 1980. Images from the SMM coronagraph appear at the left of each set of three. MLO direct intensity images are given in the center of each triplet. MLO difference images with base frame at 1800 UT are shown in the rightmost of each trio. The time for each set of three images is indicated below the pictures. North is up, east to the left. All images are printed to the same scale. SMM images at 1829 and 1959 UT are through the green broadband filter.

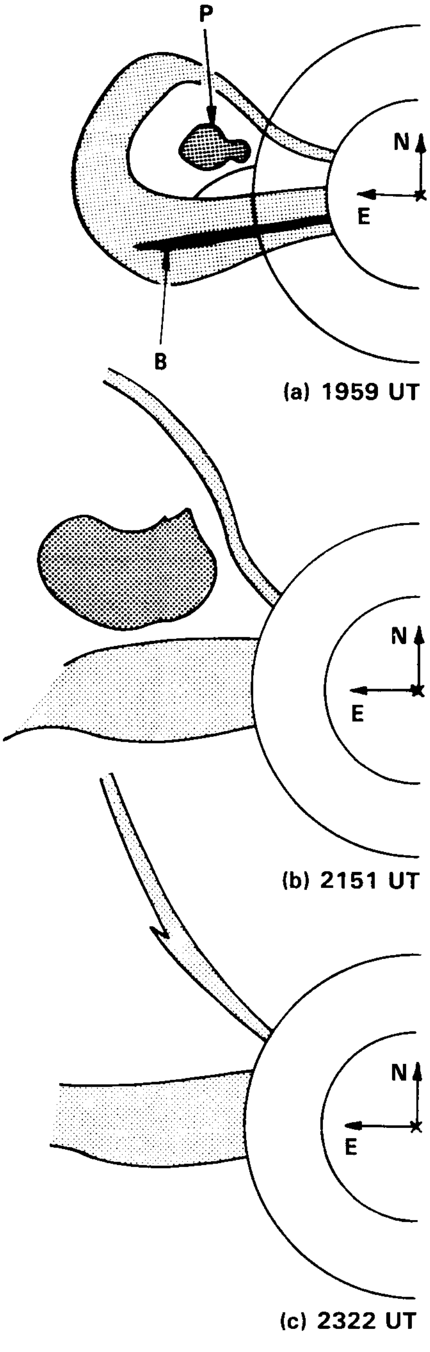

Figure 6.2.2 Schematic representation of the 5 August 1980 coronal transient at several times during the event. P is the remnant of an erupting prominence; B is a narrow, bright spike within the leg of the CME. (a) 1959 UT; (b) 2151 UT; (c) 2322 UT.

The observations suggest three "phases" in the evolution of the transient and its propagation through the corona.

Phase 1. The ejection of bright (dense) coronal material with loop-like structures visible within the ejecta.

Phase 2. Outward motion of a bright front that is concave away from the Sun. This front evolves from an "inverted arch" shape to a semi-circular annulus as its center moves outward at 175 km s^{-1}, three to four times faster than the radial velocities of structures seen in phase 1.

Phase 3. The rapid contraction of a fan-shaped bright region that appeared beneath the bright front. This contraction seems to occur from the bottom to the top of the structure and leads to a single narrow, bright ray in the region previously filled with bright transient material.

Illing and Hundhausen (1983) interpret these observations as a direct indication of magnetic reconnection at an X-type neutral point. The pinch-off point must be below 1.6 R_0 since no features are seen moving *toward* the occulting disk (as was expected by MacQueen 1980).

How common are such events within the SMM data set? An initial examination of 68 CME's reveals features similar to that described above in seven events; only additional study of these ejections (most of which are seen on fewer images than the 1980 March 15-16 transient) will reveal whether this interpretation can be applied to them. Detailed examination of SMM data from another two-day interval (27-28 March 1980) has revealed a similar structure that evolves in the manner described above, indicating that this disconnection event is not unique.

6.2.1.3 23 March 1980 — Self-Similar Expansion

Many CMEs appear to expand into the corona rather like an inflating balloon. This behavior, or more exactly, self-similar expansion, has been discussed theoretically by Low (1982). The 23 March 1980 event, described in detail by Illing (1984), is the first to be examined critically for quantitative evidence of self-similar behavior. Selected frames of the event are shown in Figure 6.2.6. Schematic drawings of these frames are given in Figure 6.2.7, with the major parts of the transient labeled.

Figure 6.2.8 gives the time-height plots for these structures. The lines shown are least squares fits to the data points, with velocities and intercepts (together with standard errors) given in Table 6.2.1. The CME's velocity is rather low, 55 to 220 km s^{-1}. Also given in Table 6.2.1 are the extrapolated times at which the features would have been at 1 R_0, with uncertainties derived from the linear fit.

Table 6.2.1 Best Fit Lines

Feature	v(km/s)	r(t = 0100) (R_0)	t(1 R_0)
D	200 ± 18	−0.28 ± 0.33	0215 ± 20
F	110 ± 5	0.02 ± 0.10	0237 ± 14
a	73 ± 1	0.54 ± 0.04	0213 ± 6
b	66 ± 3	0.47 ± 0.07	0234 ± 13
c	55 ± 4	0.54 ± 0.12	0237 ± 26

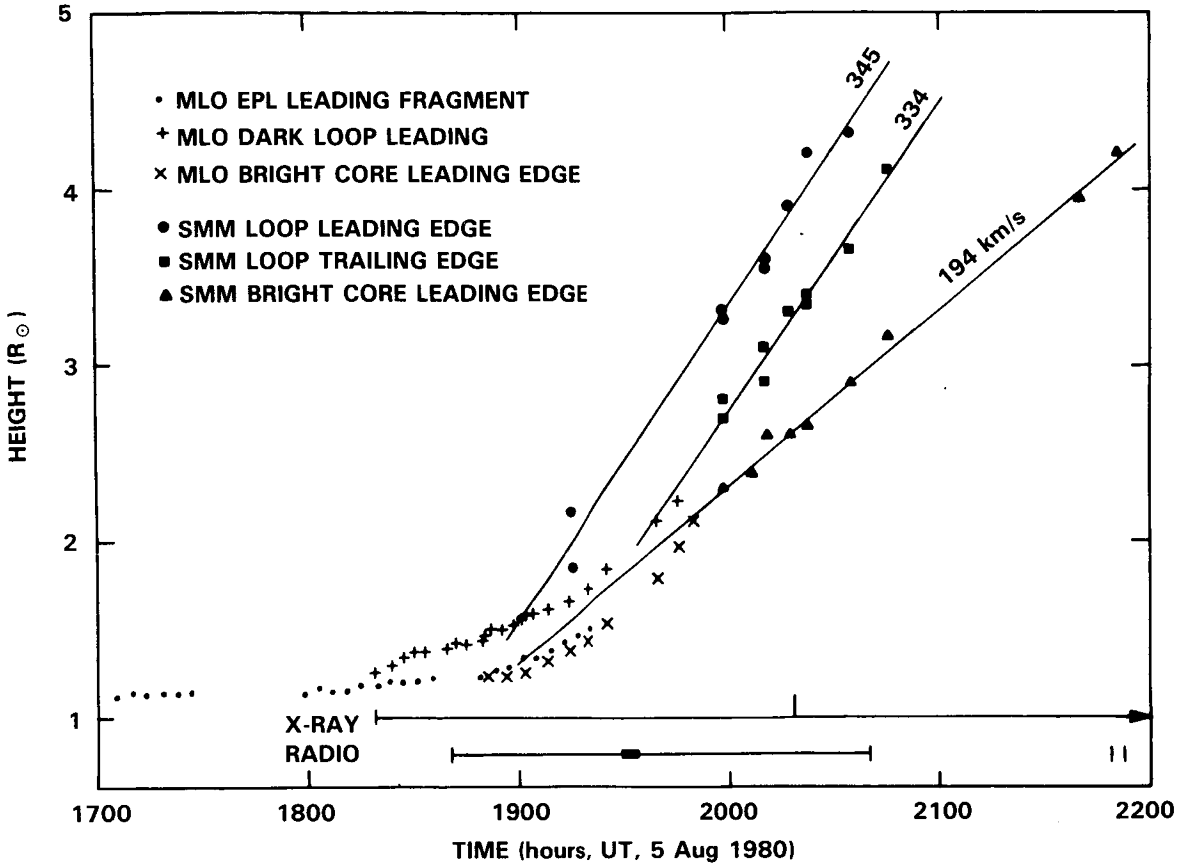

Figure 6.2.3 Height as a function of time for distinct features of the mass ejection as seen in both the C/P and MLO data. The line marked X-ray indicates the duration and peak (vertical mark) of the GOES X-ray event. The line marked Radio shows the duration of the 2800 MHz event; the thick portion indicates the continuum burst, and the two vertical bars the IIIG,W bursts.

The apparent divergence of the substructures from a common point, as shown in Figure 6.2.8, allows a test of Low's (1982) theory, described in Section 6.4.3 of this chapter. A dynamical system is said to evolve self-similarly in time if its motion can be described in terms of a variable that relates its spatial and temporal dependences. The system is then coupled in a very particular way; all forces acting on any mass element in the system have constant relative magnitudes throughout all time and space. This restrictive condition is not met, in general, for an arbitrary dynamical system. A result of self-similar motion is that distinct substructures are related such that at a given time their individual velocities are a function only of height. In Figure 6.2.9 we plot the velocities of all the substructures against their respective heights at 0700 UT. The vertical bars represent the velocity uncertainties given in Table 6.2.1. Within the errors, the points appear to lie on a straight line; the line shown is a least squares fit to the points. Since we have selected several distinct substructures in the event, Figure 6.2.9 suggests that the *entire* structure is a self-similar dynamic system.

6.2.1.4 29 June 1980

a. The Type II association. Many CMEs depart the Sun at speeds exceeding the typical Alfven speed in the corona. From magnetohydrodynamical considerations, such rapidly moving disturbances must be or be preceded by shock waves. That shock waves actually exist in the inner corona is amply shown by the observation of metric Type II bursts, which are due to plasma emission from electrons accelerated locally by the shock. The advantage of simultaneous observations of transients and spatially resolved Type II bursts is obvious — such observations are the only way to determine the exact spatial relationship between CMEs and shock waves and, given good fortune, to determine the electron density in the Type II-emitting source. All during the Skylab era, however, no simultaneous observation was successfully made. The 29 June 1980 event, described by Gary *et al.* (1985), is one of only four events observed during the SMM period accompanied by a spatially resolved Type II burst.

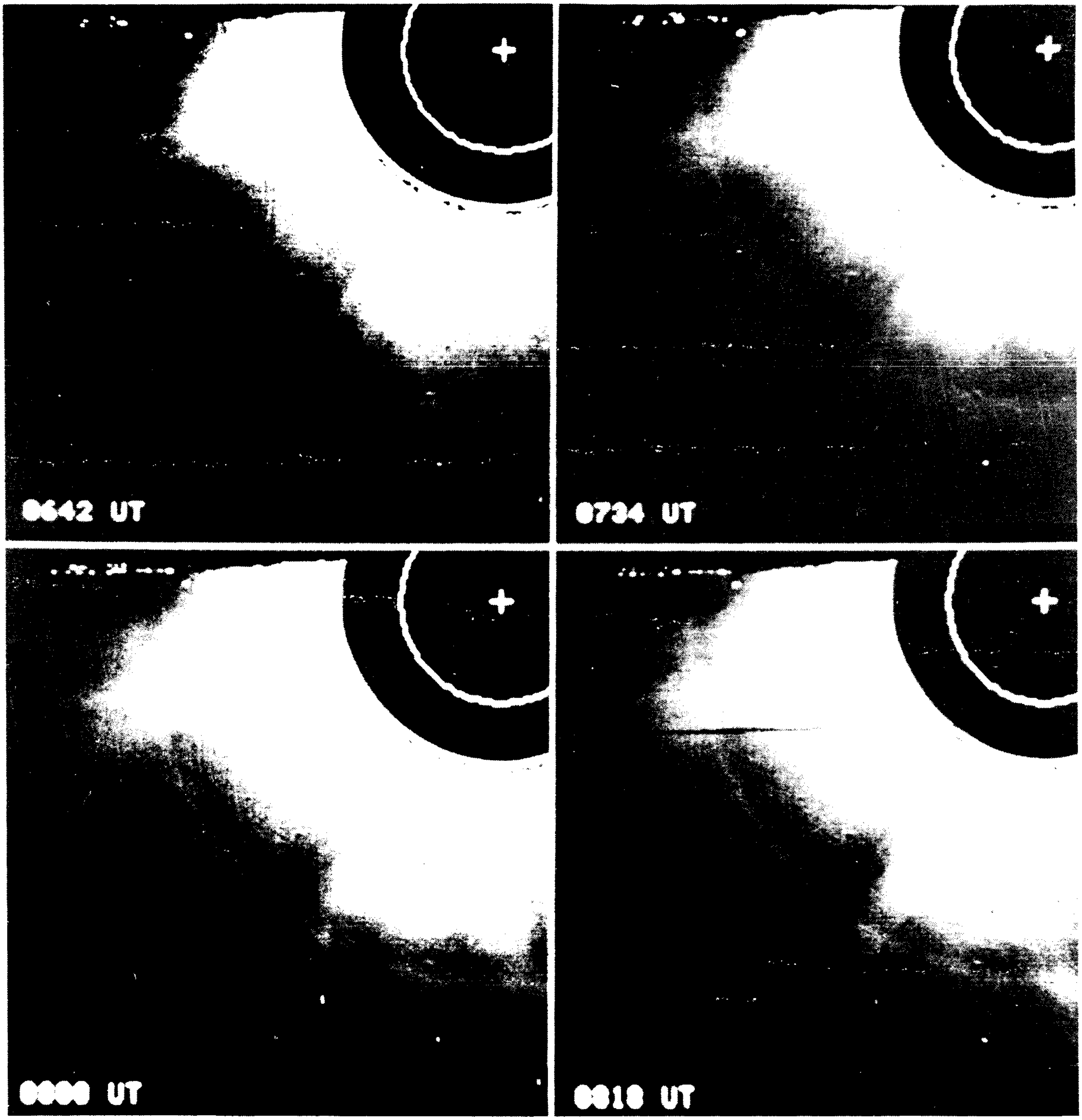

Figure 6.2.4 Coronagraph/Polarimeter images showing the progress of the concave upward structure on 16 March 1980. The time for each frame is indicated at the lower left. North is to the upper left, east to the lower left. The radius of the first, brightest diffraction ring surrounding the occulting disk is 1.61 R_0. The length of one side of a frame is approximately 5.5 R_0. The center and limb of the Sun are surrounded on each image.

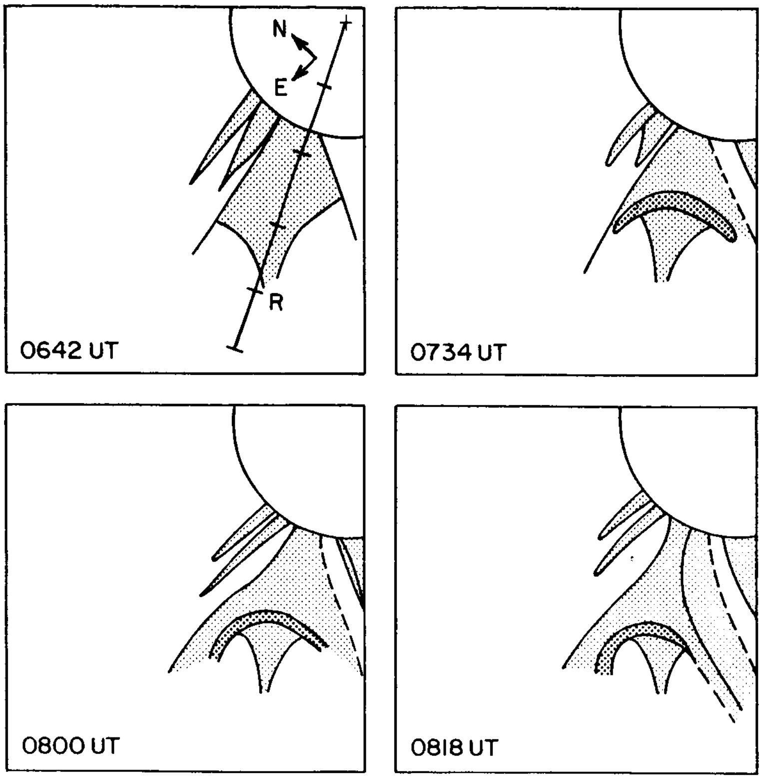

Figure 6.2.5 Schematic diagram of the 16 March 1980 images in Figure 6.2.4, showing the major parts of the event. The position of the front has been measured along the radius indicated R, about 27° south of the projected equator. The center of the occulting disk is again shown by a cross, and radius R is marked in units of R_o.

The CME was associated with the first of three limb flares that occurred in Hale Region 16923 on 29 June 1980. The initiation of the coronal mass ejection and the timing of the X-ray bursts associated with it are discussed in Section 6.3.2.

The CME appears initially as two loops that move radially outward at about the same speed, ~ 600 km s^{-1} (see Figure 6.2.10). A third loop is located northward from the original loops, a faint halo leads all three loops and a remarkable arc-like feature stands off to the north of the loop complex, extending from about PA 250° to PA 280°. (Each of these features is shown schematically in Figure 6.2.10c.) The faint arc does not resemble the loops of the CME, but appears as a circular arc whose center of curvature is very near the position of the flare. The arc moves at an approximately constant velocity of about 900 km s^{-1}. Note that the faint arc is quite easily seen in the SOLWIND image taken at 0322 UT and presented as Figure 6.5.1b.

Simultaneous observations of radio spectra, polarization and positions were obtained with the instruments of the CSIRO Division of Radiophysics at Culgoora, Australia. Type III/V bursts mark the start of the flare at 0233 UT, and a strong fundamental/harmonic Type II (shock wave related) burst begins at about 0241 UT.

It is possible that the faint arc marks the density enhancement (compression region) immediately behind a shock wave. Its position ahead of the loops of the transient, its faster speed, and its circular arc shape are all suggestive of this. To see whether the arc is the site of Type II emission, we determine the electron density within the enhancement, averaged over the length of the arc, and display it in Figure 6.2.11 as a function of height for two cases. The maximum density suggests that emission at the second harmonic of the plasma frequency should have been visible near 20 MHz, and higher frequency emission should have been visible at earlier times when the arc was traversing higher density layers lower in the corona. No such emission is seen. We conclude that the faint arc was not a source of radio emission. The observed Type II emission was, instead, associated with the loops, as demonstrated in Figure 6.2.12.

To determine whether the faint halo of enhanced density shown in Figure 6.2.10 is a forerunner, we adopt the Jackson and Hildner (1978) definition of the leading edge of the

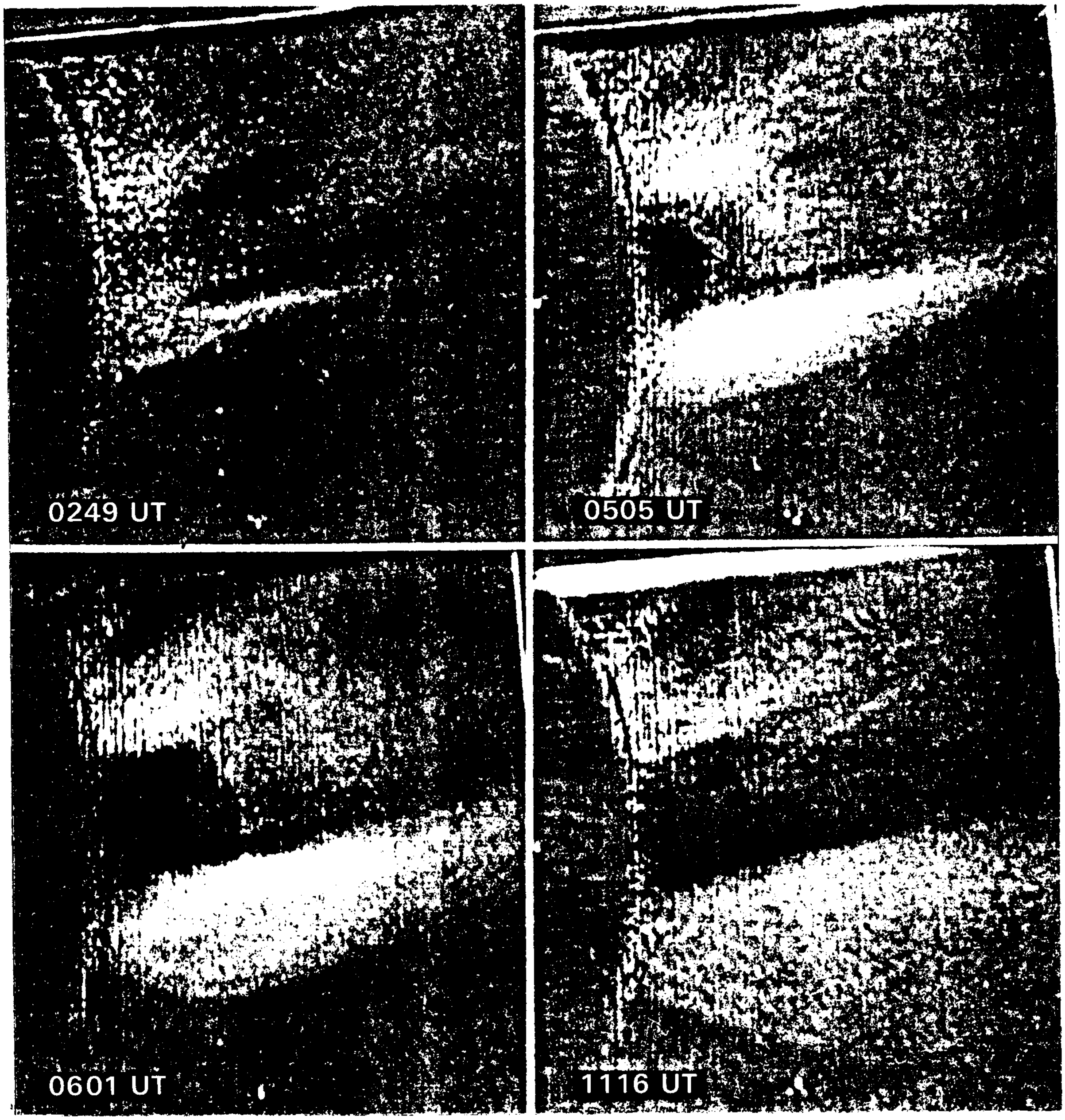

Figure 6.2.6 SMM Coronagraph/Polarimeter difference images showing the development of the 23 March 1980 depletion CME. Frames are oriented with north to the upper left and west to the upper right. The brightest diffraction ring of the occulting disk occurs at 1.61 R_o. All times are UT. The reference frame was observed at 0113 UT; scaling is identical for all frames.

forerunner as the point where the excess columnar density falls below the 2σ noise level (1.15×10^{-8} g cm^{-2}); we set the second contour level at 1.3×10^{-7} g cm^{-2}, to delineate the boundary between the transient and the forerunner. The similar appearance of the forerunner in Figure 6.2.13 and the ATM forerunners shown by Jackson and Hildner (1978) leads us to conclude that this is the same phenomenon.

Also visible in Figure 6.2.13 are portions of the faint arc ahead of both the CME and forerunner. The arc extends to position angles far to the north of the forerunner and there is no indication of a forerunner behind that portion of the arc. However, at other position angles the density enhancement seems to extend from the arc to the loop transient.

The relationships among the faint arc, forerunner and CME loops shown in Figure 6.2.13 find a natural explanation if the faint arc and the forerunner are the compression region behind a shock front. In this picture, the loop-shaped CME is the piston that drives the shock; a piston that con-

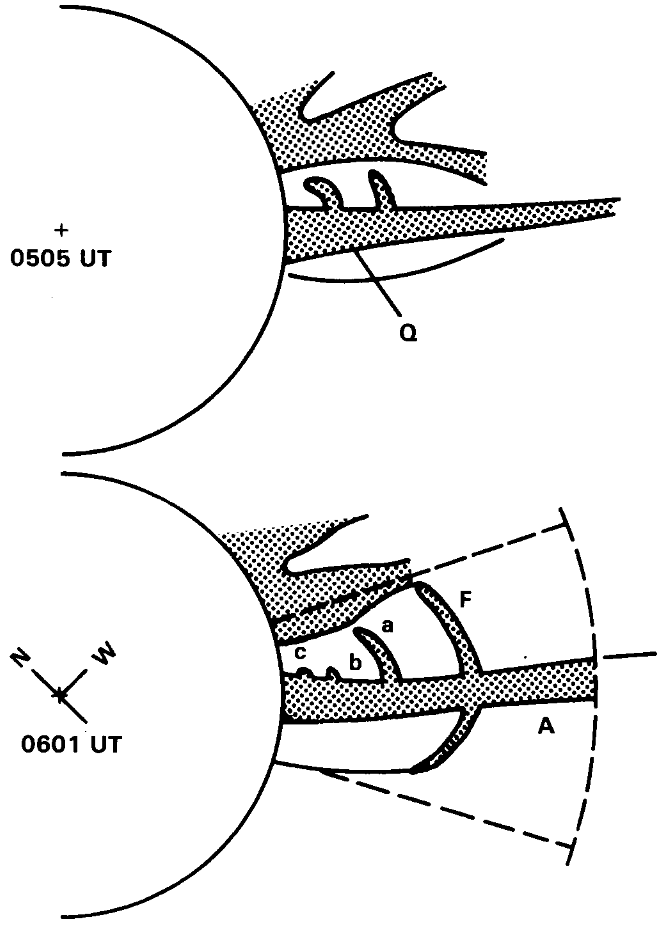

Figure 6.2.7 Schematic representation of the 23 March 1930 event shown in Figure 6.2.6. Streamers and substructures are labeled as they are referred to in the text. The dotted line in the drawing for 0601 UT indicates the area covered by the excess mass calculation for the entire event. The radial line protruding from the outer dotted line marks position angle 230°.

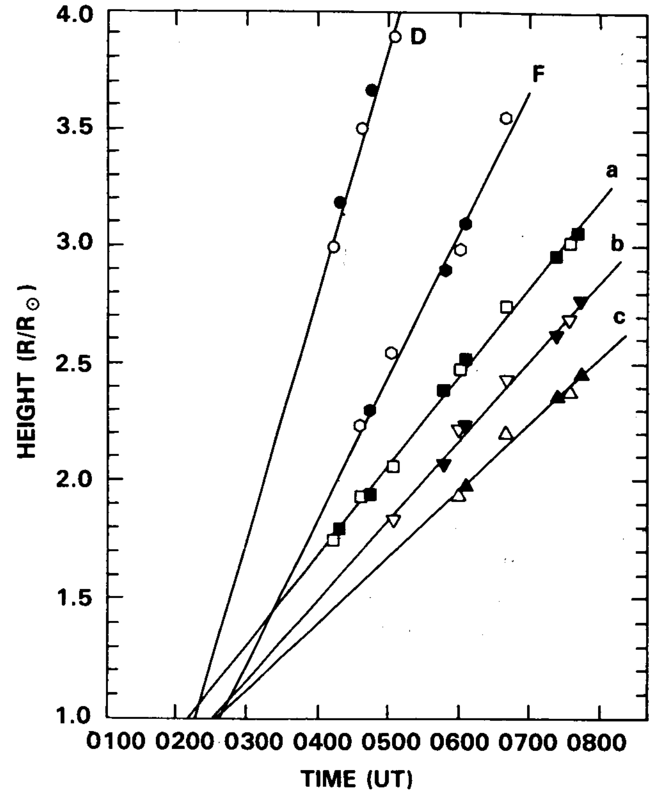

Figure 6.2.8 Height-time plots for several substructures in the 23 March 1980 event shown in Figures 6.2.6 and 6.2.7. Positions for features F, a, b, and c are measured from scans at position angle 229°, verified by inspection of the direct frames. Positions of the diffuse front D are measured from radial scans at position angle 242.5°, where D is seen moving through a relatively dim background. Open symbols indicate measurements from a south sector frame, filled symbols, from a west sector frame. Parameters of the least-squares fit lines shown are given in Table 6.2.1.

sists of material originating in the low corona. This is the same picture that was proposed by Dulk *et al.* (1976) to explain the CME and forerunner of 14-15 September 1973 (although the term forerunner was not used by them).

If we assume that the density enhancement in the faint arc is due to compression of material passing through a shock front, we can estimate the range of Mach numbers for the shock from the two extremes of density given in Figure 6.2.11. At $R=3\ R_0$, Figure 6.2.11 shows the excess density $\Delta n = n_2 - n_1$ of the shock front to be $0.3n_1 < n < 2n_1$ where n_1 is the background density also shown in the figure. The density ratio across the shock is then $1.3 < n_2/n_1 < 3$, giving a range in Mach number [from the Rankine-Hugoniot jump relation $n_2/n_1 = 4M_A{}^2/(3+M_M{}^2)$] of $1.2 \leq M_A \leq 3$. From the observed speed of the arc ($\sim$900 km s^{-1}) and assuming an ambient solar wind speed of $\sim$150 km s^{-1} at 3 R_0 (Parker, 1958), the corresponding range of Alfven speed and magnetic field strength in the ambient medium can be obtained. The results are in Table 6.2.2. The parameters for $d=1.5\ R_0$ seem to be most consistent with other observations.

Table 6.2.2 Parameters for shock wave (at $R = 3\ R_0$)

	Line of Sight Depth	
	$d = 0.2\ R_\odot$	$d = 1.5\ R_\odot$
n_2/n_1	3.0	1.3
Mach Number	3.0	1.2
v_A (km s)	250	625
B (gauss)	0.05	0.12

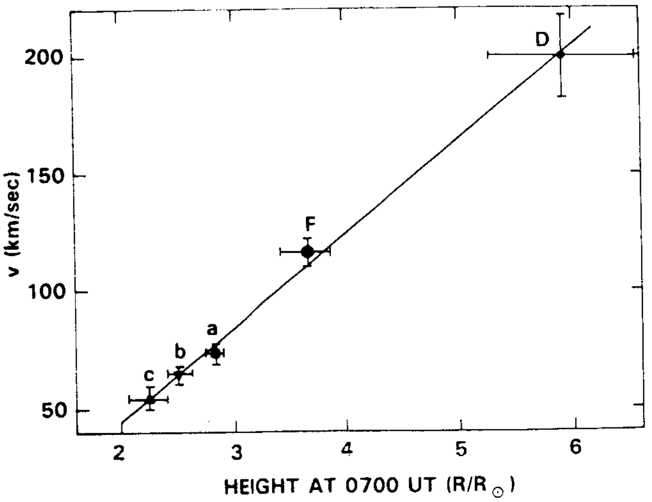

Figure 6.2.9 Velocity of substructures as a function of radial distance at 0700 UT 23 March 1980. Symbols and labels correspond to similarly labeled features in Figures 6.2.7 and 6.2.8 and in Table 6.2.1.

An idealized sequence of events that is consistent with the data is as follows: The magnetic configuration in the corona above the active region becomes unstable and begins to expand, eventually forming a loop-shaped CME. A quasi-parallel, piston-driven shock wave develops in the upper corona above the transient, which does not generate radio emission. Accompanying the expansion are alterations to the low coronal environment that lead, a few minutes later, to the impulsive flare. The resultant thermal pulse initiates a blast wave that evolves into a shock, generating Type II radiation as it moves quasiperpendicularly to the magnetic field lines in the lower corona and in the ejected material of the transient. As it progresses farther into the confused corona — into faster moving material — its velocity relative to the surroundings becomes smaller, finally becoming sub-Alfvenic, ceasing to be a shock and quenching the Type II emission. We note that Cane (1984) presents further evidence of the existence of two shocks in some CME events, based on the continuation of Type II bursts to low frequencies observed by the ISEE-3 spacecraft.

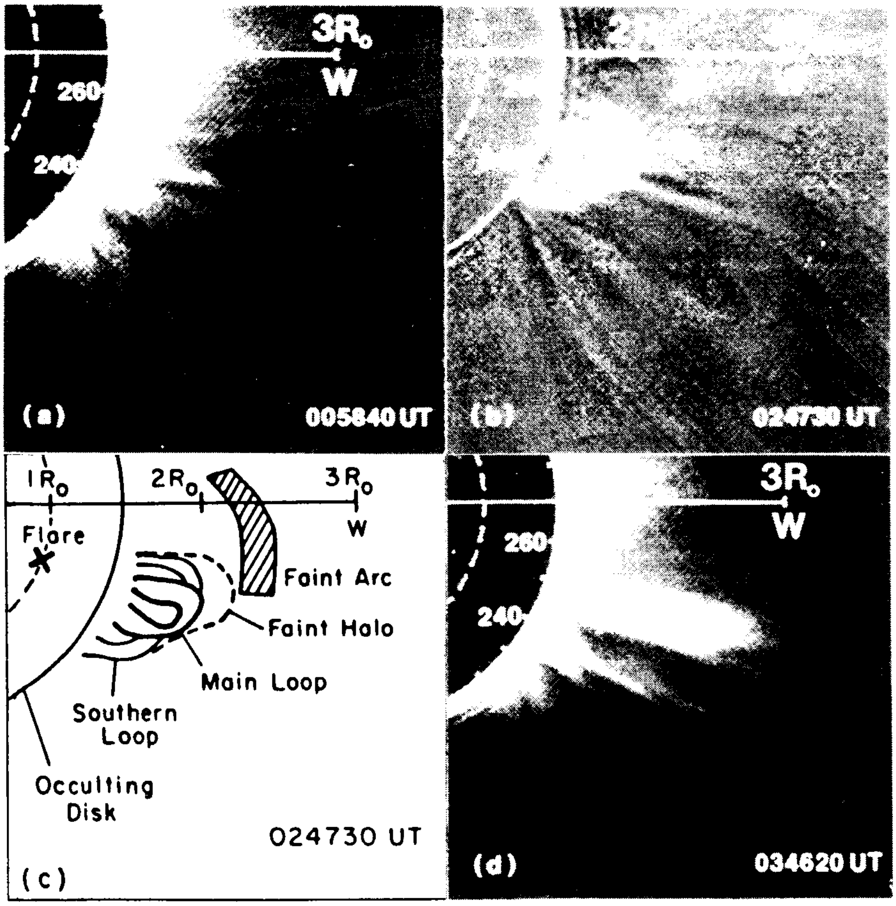

Figure 6.2.10 (a) Pre-event C/P image taken 0059 UT 29 June 1980, before the beginning of the transient. (b) A subtracted image in which the image shown in (a) was subtracted from an image taken during the transient at 0248 UT. (c) A schematic drawing of the image of (b) illustrating the main features discussed in the text. (d) the appearance of the corona at 0346 UT after the transient, showing the bright central streamer flanked by thin legs.

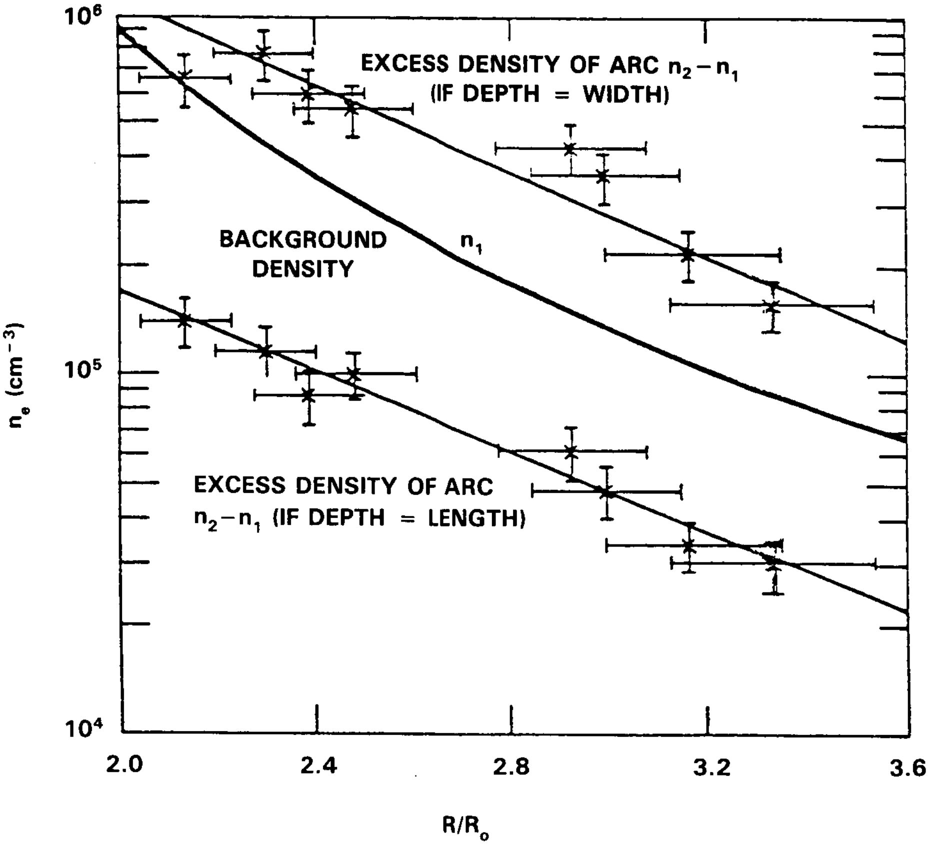

Figure 6.2.11 Comparison of the excess density of the arc n_2-n_1 with background density n_1 (heavy line) for two cases: (1) depth of the arc same as arc width (upper points) and (2) depth of the arc same as arc length (lower points). Horizontal bars represent the width of the front. Vertical bars represent measurement uncertainties. Uncertainty in n_1 due to our choice of F-coronal brightness ranges from 8% at 2 R_0 to 40% at 3.6 R_0.

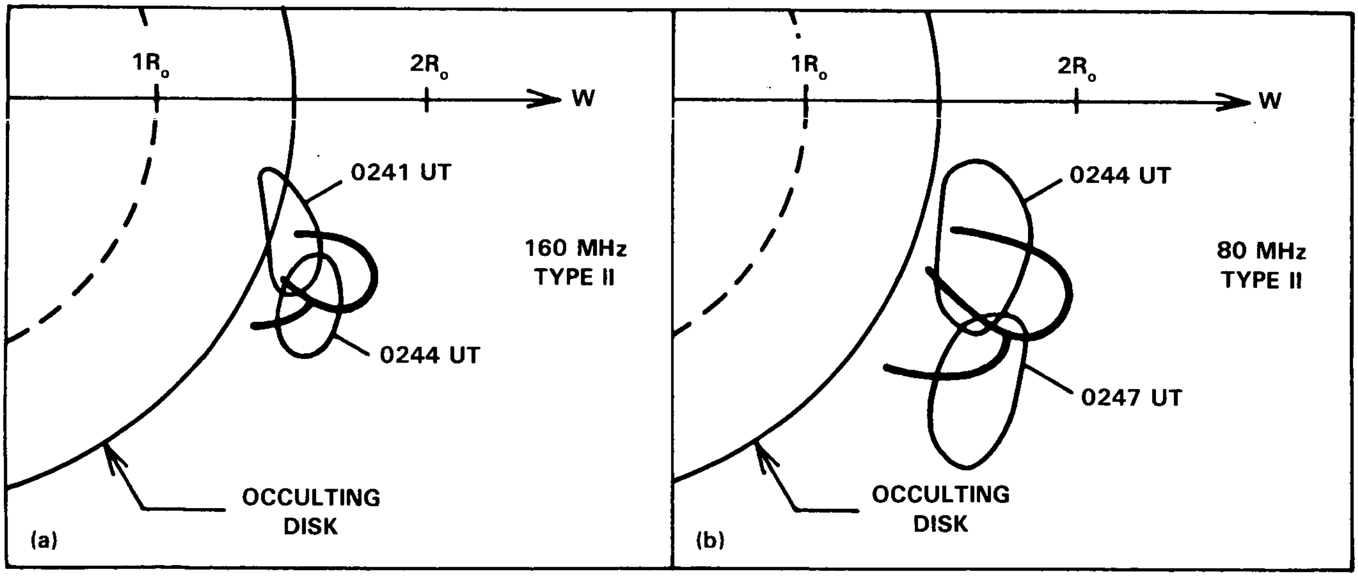

Figure 6.2.12 Schematic diagrams of the early 29 June 1980 CME at two times (a) 0244 UT and (b) 0248 UT, and comparison with the 160 and 80 MHz Type II burst positions.

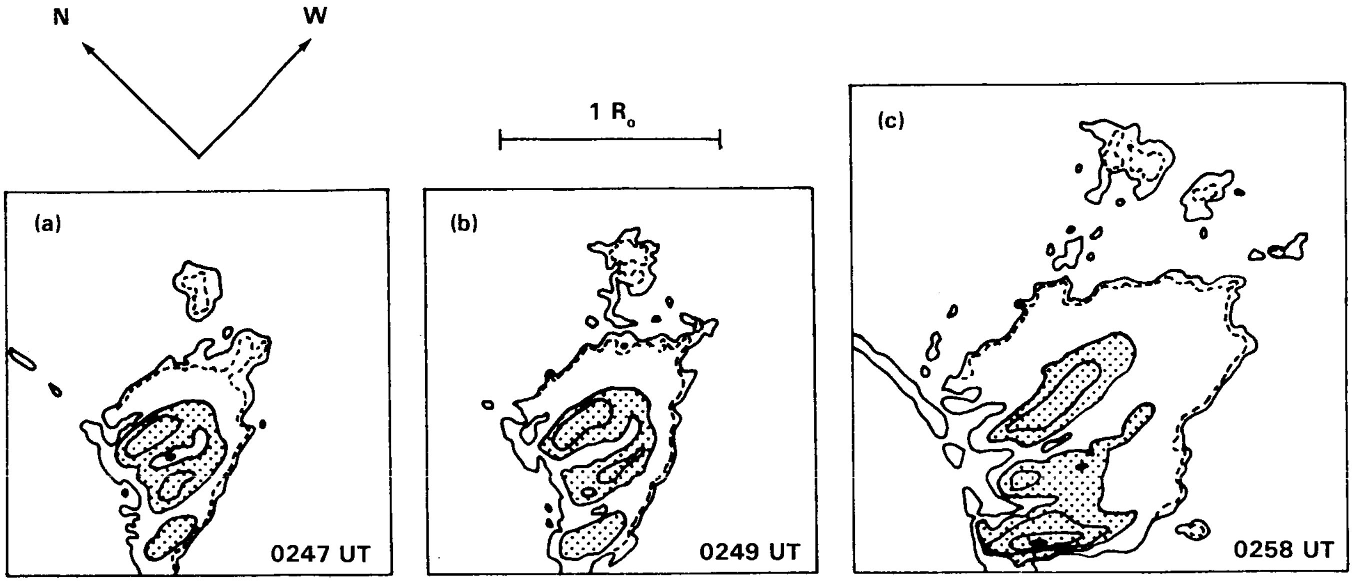

Figure 6.2.13 Contour plot of loops and forerunner at three times on 29 June 1980: (a) 0248 UT, (b) 0249 UT, and (c) 0257 UT. The lowest contour corresponds to the 2σ noise level of 1.15×10^{-8} g cm^{-2}. The hatched area denotes the brightest (densest) parts of the transient above 1.3×10^{-7} g cm^{-2}. The areas of slightly enhanced density outside the forerunner are parts of the faint arc. The dashed contour at 2×10^{-8} g cm^{-2} is included to show the faintness of the arc.

b. The Type IV association. The discussion above concerned the radio emission produced at the leading portions of the CME. The interior region behind the transient is also of interest in understanding what becomes of the electrons accelerated during the disruption, and how the corona relaxes into its post-ejection state. The study of metric Type I and Type IV sources is potentially a direct way to quantify conditions within CMEs, but only when the mechanism responsible for these emissions are known. The 29 June 1980 event, described in detail by Gary *et al.* (1984), offers a chance to determine the emission mechanism for at least one kind of Type IV burst, a burst observed at Culgoora at 80 and 43 MHz.

The appearances of the CME at 0258 UT during the transient, and at 0346 UT after the CME reaches the edge of the field of view of the C/P, are shown in Figure 6.2.14. By 0346 UT, a bright streamer remains where the northern leg of the loops had been. Subsequent images show this streamer decreases slowly in brightness. It is with this streamer that the late Type IV sources are associated. The time behavior of the transient and the Type IV sources at 80 and 43 MHz are shown schematically in Figure 6.2.15.

There are two possible emission mechanisms that can account for Type IV radio emission — plasma emission (either fundamental or harmonic) and gyrosynchrotron emission. These were examined in detail by Gary *et al.* (1984), with the following results:

The sources at 80 and 43 MHz showed characteristics expected of harmonic plasma emission:

1. The 80 MHz source moves along the densest part of the transient in conjunction with rising of the relevant (40 MHz) plasma level.
2. Both 80 and 43 MHz sources are associated at all times with features whose density is probably high enough to account for the emission as harmonic plasma emission.
3. The polarization of the 80 MHz source is consistent with harmonic plasma emission.
4. At times the spectrograph shows weak Type II-like bursts that imply acceleration of electrons from lower in the corona to energies of a few keV. The source of these electrons could be the source of the electrons producing the continuum emission.

Gyrosynchrotron emission is found to be less likely, especially when Razin-Tsytovich suppression is taken into account; about 10% of the electrons in the source region would need to have energy greater than 10 keV, with the average energy of emitting particles being ~40 keV. Another requirement, which seems unlikely to be met, is that the magnetic field strength at 2.5 R_0 be ~2.8 gauss.

It is also found that the emission at 80 and 43 MHz is probably not due to optically thick gyroresonance emission at low harmonics of the gyrofrequency. If it were, the highest harmonic that is optically thick for reasonable numbers of energetic electrons is $s=5$, for which a magnetic field strength of 5.7 gauss is required.

In conclusion, it seems more likely that the 80 and 43 MHz sources are due to harmonic plasma emission than to

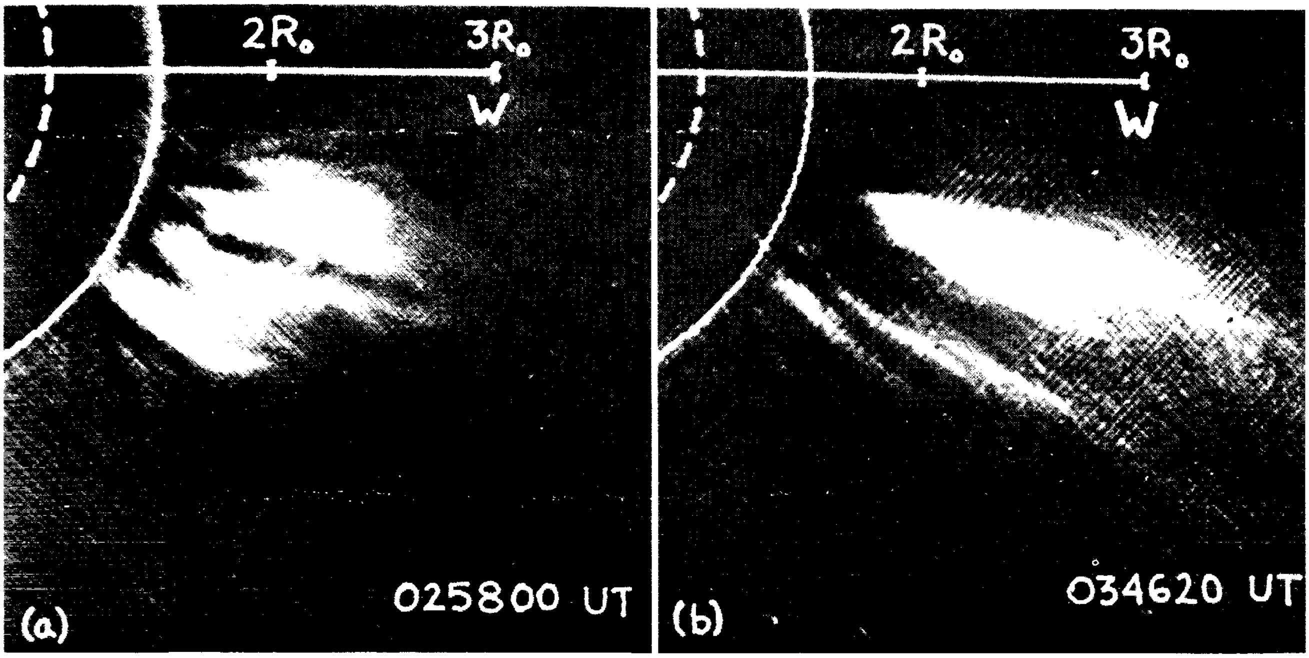

Figure 6.2.14 Subtracted C/P images of the 29 June 1980 transient at (a) 0258 UT and (b) 0346 UT, identifying the northern leg of the loop in (a) with the remnant streamer in (b).

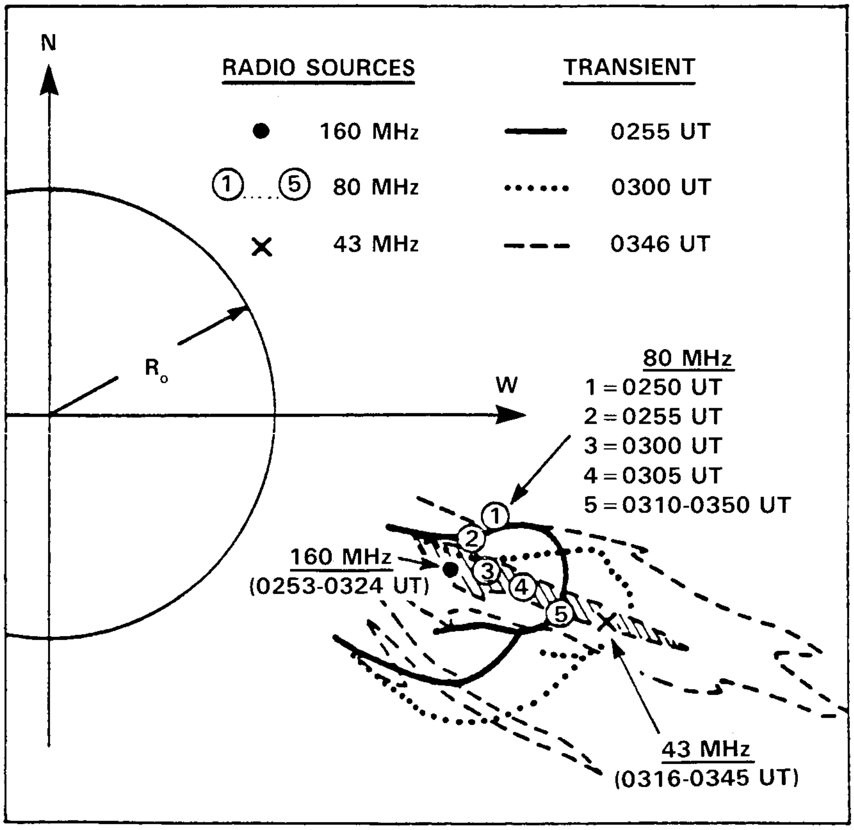

Figure 6.2.15 Comparison of corrected radio source positions with visible-light features in the C/P images of 29 June 1980. The 80 MHz Type IV source (circled numbers 1-5) is always associated with the densest part of the transient.

gyrosynchrotron emission. If so, the radiation could be due to ~ 1 to 3 keV electrons continuously accelerated lower in the corona and having a plateau distribution in velocity space.

6.2.1.5 30 March 1980 — A Type I Noise Storm Associated Event

Another type of continuum emission localized below some transients is the metric Type I noise storm. Type I emission differs from Type IV emission in that, although its intensity can increase during a coronal transient, it is generally independent of the CME itself, existing both prior to and after the event. This CME, described in a series of papers by Lantos *et al.* (1981), Lantos and Kerdraon (1984) and Lantos (1984), is a loop-shaped event that occurs in a region where there already existed a weak Type I source, observed at 169 MHz by the Nancay Radioheliograph.

On 30 March, active region 2363 was situated at 25° N and 25° E and consisted of two main spots of the same polarity bordered on their east and south sides by a chain of H-alpha filaments. The southern filament began to dissipate before 0938 UT, but the radio and X-ray events began only around 1300 UT. Region A in Figure 6.2.16 was a source of Type I continuum emission from before 0510 UT. Beginning at 1310 UT, the brightest point of the emission left source location A and followed the trajectory indicated in Figure 6.2.16, again becoming stationary at location B after 1330 UT.

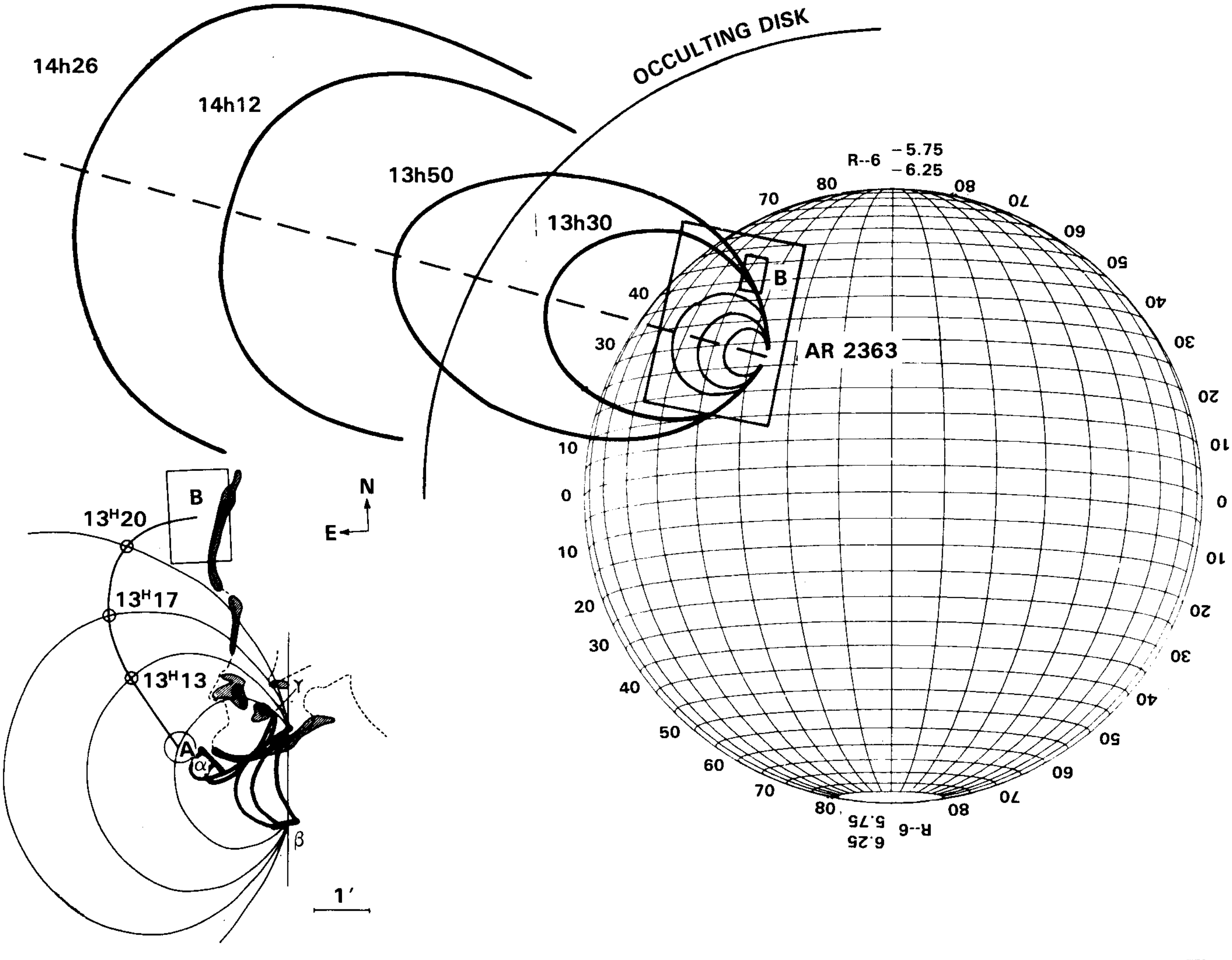

Figure 6.2.16 The coronal mass ejection of 30 March 1980. Inset is a schematic of the active region. The loop features at lowest height are derived from soft X-ray data (after Lantos *et al.,* 1981). The line joining A and B is the path of a type I metric noise storm. Based on this, Lantos and Kerdraon, (1984), constructed the ascending loops as shown in the small figure; these expand into the corona in a way which is consistent with the coronal transient observations shown in the larger figure. H-alpha ribbons are connected as shown α with δ, β with γ.

The source at point A is large (about $4' \times 5'$), with at least two components, indicating that the continuum emission probably originates from an arcade of loops rather than from a single loop. The apparent velocity of the 169 MHz source from point A to B is ~ 300 km s^{-1}. A CME (sketched in Figure 6.2.16) is observed at 1412 UT and 1426 UT with the C/P instrument. The ejection appears loop-like, with a lateral width about half the radial height above active region 2363. If we assume radial motion of the transient, the observed velocity corresponds to a true speed of 600-800 km s^{-1}. This seems too high for a CME associated with a disappearing filament in the absence of an H-alpha flare (Gosling *et al.*, 1976). Thus, it is likely (and we shall assume) that the motion was not radial but inclined somewhat $\sim 30°$) from the local meridian toward the east.

The emission mechanism for the noise storm in this event will be assumed to be due to plasma waves excited by ~10-30 keV electrons (Melrose 1980, Benz and Wentzel, 1981). According to plasma wave theories, the radio emission occurs near the plasma frequency level defined by

$$\omega_p^2 = \frac{4\pi\, n_e\, e^2}{m_e} .$$

The radio emission at a given frequency takes place at a constant electron density which, for 169 MHz, is $n_e = 3.5 \times 10^8$ cm^{-3}. The motion of the noise storm is thus a trace of this density level during the evolution of the involved coronal structure.

The event can be modeled with a simple loop geometry to determine whether the radio emission could have occurred in the CME itself. The initial loop is taken to be circular, isothermal, in hydrostatic equilibrium, and with a top altitude of 10^5 km. The foot points are anchored (like the X-ray emitting loops) on H-alpha ribbons β and δ (see Figure 6.2.16). The top of the loop in the model rises with a velocity of 370 km s^{-1} as suggested by the coronagraph observations. We increase the ellipticity of the model loop during its expansion to fit the CME observations. Comparison of the model with observation gives reasonable agreement when the initial loop has a density of 3.1×10^8 cm^{-3} at the top and a temperature of 4.5×10^4 K. The density gradient inside the initial loop is the main parameter that determines the trajectory of the constant density level during the motion. Thus, temperature in the model is directly dependent on the hydrostatic equilibrium assumption.

The noise storm motion could be fit with a model assuming a loop velocity of 370 km s^{-1}; extrapolation of the motion until 1412 and 1426 UT coincides with the location of the CME observed with the C/P instrument (Figure 6.2.16). Thus, our model of the displacement of the source is consistent with the idea that the emission arose in the CME itself during its early phases. Placing the Type I source in the leg of a CME recalls a similar feature of stationary type IV bursts such as the 29 June 1980 event we have just seen. We will see this same phenomenon in the next two events as well.

6.2.1.6 7 April 1980 — A Type IV Associated Event

This event, described in a preliminary way by Wagner *et al.* (1981), contains a moving Type IV radio burst — that is, a source of continuum emission that moves outward. The event also contains a more typical *stationary* Type IV burst, similar to the event of 29 June 1980 just described. The stationary Type IV in this event differs from that of the previous event, however, because the 43 MHz source early in this event is associated not with a density enhancement, but rather with a void. The following description is based on work by Bassi, Dulk, and Wagner (1985).

The CME appears in visible light as a large loop extending from near the solar equator to the north pole. The associated meter wave radio sources cover a similar range of positions. At the time of the first SMM coronagraph image (0405 UT), the ejection is already well developed with a very bright leg to the west and a smoothly northward curving arc, as shown in Figure 6.2.17. During the loop's expansion, blobs of brighter material part way up the loop move non-radially in a direction perpendicular to the loop with speeds on the order of 450 km s^{-1}. In contrast, a "kink" feature (a discontinuity in the curvature of the loop) moves radially outward with a speed of about 550 km s^{-1}, i.e., it does not participate in the whip-like motion evidenced by the blobs.

Radio observations with the Culgoora radioheliograph show both moving and stationary Type IV sources at 80 MHz and 43 MHz. No Type II burst was observed at any time during the transient.

The 80 MHz source moves almost radially outward from the Sun (Figure 6.2.17), with the last observed position of the source centroid being coincident with the kink rather than with a bright blob proposed by Wagner *et al.* (1981). Analysis of subsequent images shows that the kink movement is at approximately the same speed and direction as the previously observed 80 MHz Type IV source. This spacial coincidence between the kink and the moving source leads us to speculate that the dynamic phenomenon that produces the kink also is an exciting mechanism for the 80 MHz emission. It is possible that the radio source is due to plasma emission as the kink moved up the leg, and that the emission stopped at 0405 UT because the kink travelled to a region of density that is too low to support 80 MHz emission. In support of this idea, we find that the density in the loop below the kink at 0405 UT is 10^7 cm^{-3}, resulting in a plasma frequency of ~ 30 MHz. The inferred density is somewhat greater if the brightness contribution from the background corona is taken into account. Thus, the result appears consistent with the hypothesis that the observed radiation at 80 MHz was produced by second-harmonic plasma emission,

ORIGINAL PAGE IS
OF POOR QUALITY

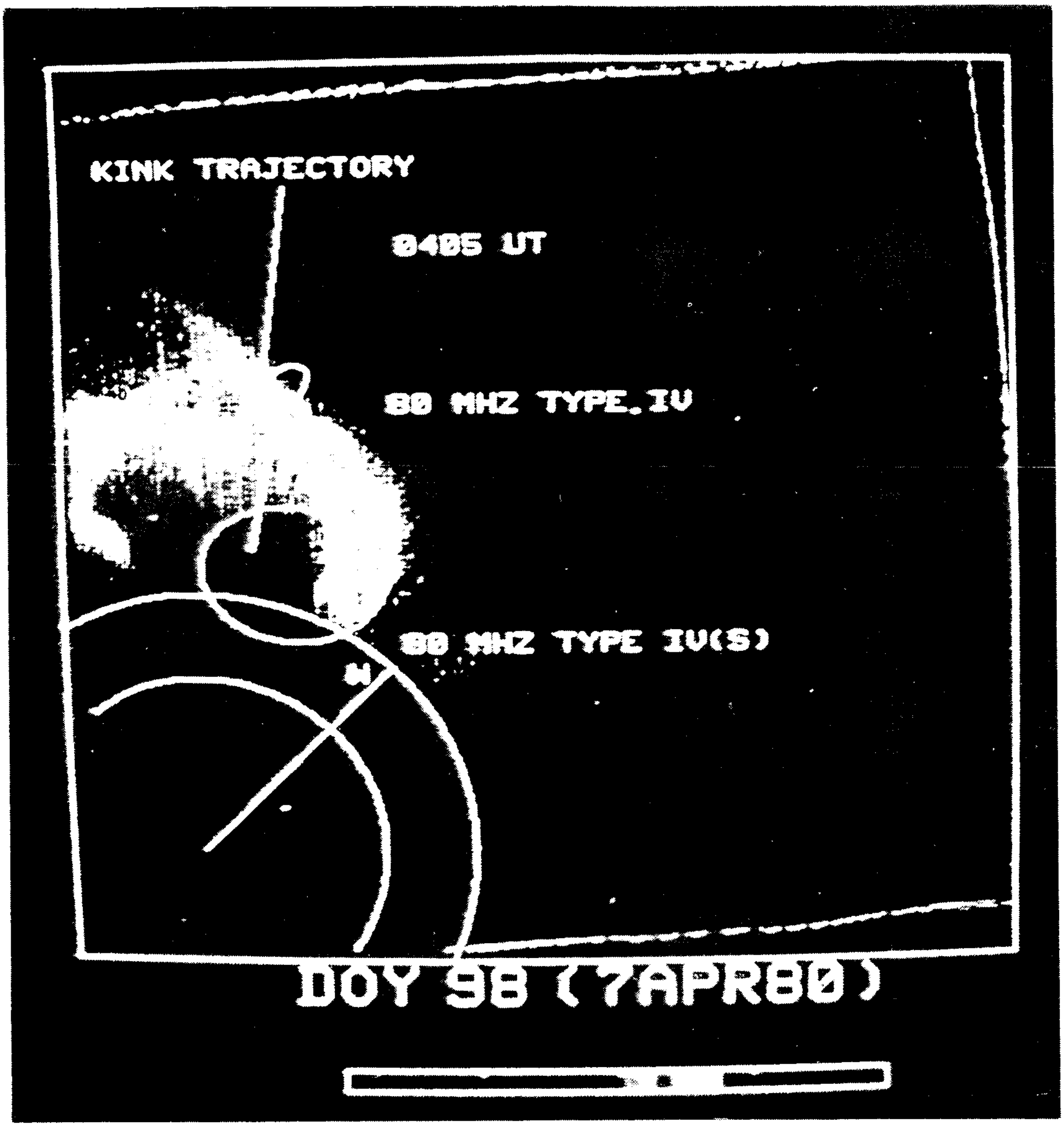

Figure 6.2.17 A difference image showing the south leg of the loop-shaped CME of 7 April 1980, the trajectory of the 80 MHz Type IVM radio source until 0405 UT, and the trajectory of the kink in the loop after 0405 UT. Also shown are the positions and sizes of the 80 MHz Type IV stationary and moving sources at 0405 UT.

which requires a plasma frequency ~40 MHz (density ~2 × 10^7 cm^{-3}).

The 43 MHz emission at 0405 UT could be interpreted either as coming from a single large, elongated source or from a double source. The more northerly part of the source lies over the void below the loop; the other part is coincident with the west leg of the CME. As time progresses, the part of the source coincident with the void fades, while the other part becomes coincident with the leg (Figure 6.2.18) and elongated in the direction of the leg. The association of stationary Type IV sources with the legs of transient loops seems a common feature (as in the 29 June 1980 event of Section 6.2.1.4b).

6.2.1.7 9 April 1980 — A Type II (Shock Wave) and Type IVM Associated Event

This event is described by Gergely *et al.* (1984). The event was comprehensibly observed; in H-alpha at the Haleakala Observatory of the University of Hawaii, in visible light by the Coronagraph/Polarimeter (C/P) experiment aboard SMM, as well as the coronagraph aboard the US Air Force P78-1 satellite, and at meter-decameter radio wavelengths by Clark Lake (CLRO) and Culgoora Radio Observatories. As for the 29 June 1980 event, both Type II and Type IV radio emissions were observed with this event. However, the first C/P image was after the Type II burst

Figure 6.2.18 The position of the later 43 MHz Type IV source at 0421 UT. The evolution of the source at 43 MHz suggests that the component in the void below the loop has faded, and a new source has appeared over the dense leg of the transient.

ceased at CLRO, so no firm conclusions about the relative locations of the transient and the shock can be reached. The moving Type IV burst (Type IVM), however, can be associated with an overdense feature in the transient.

Observations at Haleakala show the development of an eruptive prominence in the low corona in association with the event. The evolution of the CME observed by the C/P is shown in the sequence of Figure 6.2.19. The complex structure suggests multiple loops with some similarity to the arcade of loops seen at the same position angle ten hours earlier.

A bright blob, which we believe to be a genuine density enhancement, moves with a velocity similar to that of the other features; it appears to be situated within a loop, and is most clearly seen in Figure 6.2.19c as the brightest part of the outer loop.

CLRO observed a Type II (shock related) burst that lasted from about 2236 to 2243 UT. The Culgoora radioheliograph went into operation at 2255 UT, after the Type II burst had ceased. From 2255 UT until ~0000 UT, a complex of six distinct sources were observed at positions shown in Figure 6.2.20. After correcting for ionospheric effects by using the known Type I noise storm source A as a reference, it is found that all of the sources remain stationary to within a source diameter, except for one (source E), which moves outward from ~2.4 to ~3.0 R_0 with a projected speed 500 km s^{-1}. We thus identify the sources as follows: A and B are persistent sources, most likely of Type I; C and D are very intermittent and may be Type I sources also; E is a moving Type IV source; the nature of source F is not clear.

The Type II burst, observed with the CLRO arrays and with the Culgoora spectrograph, evolves as shown in Figure

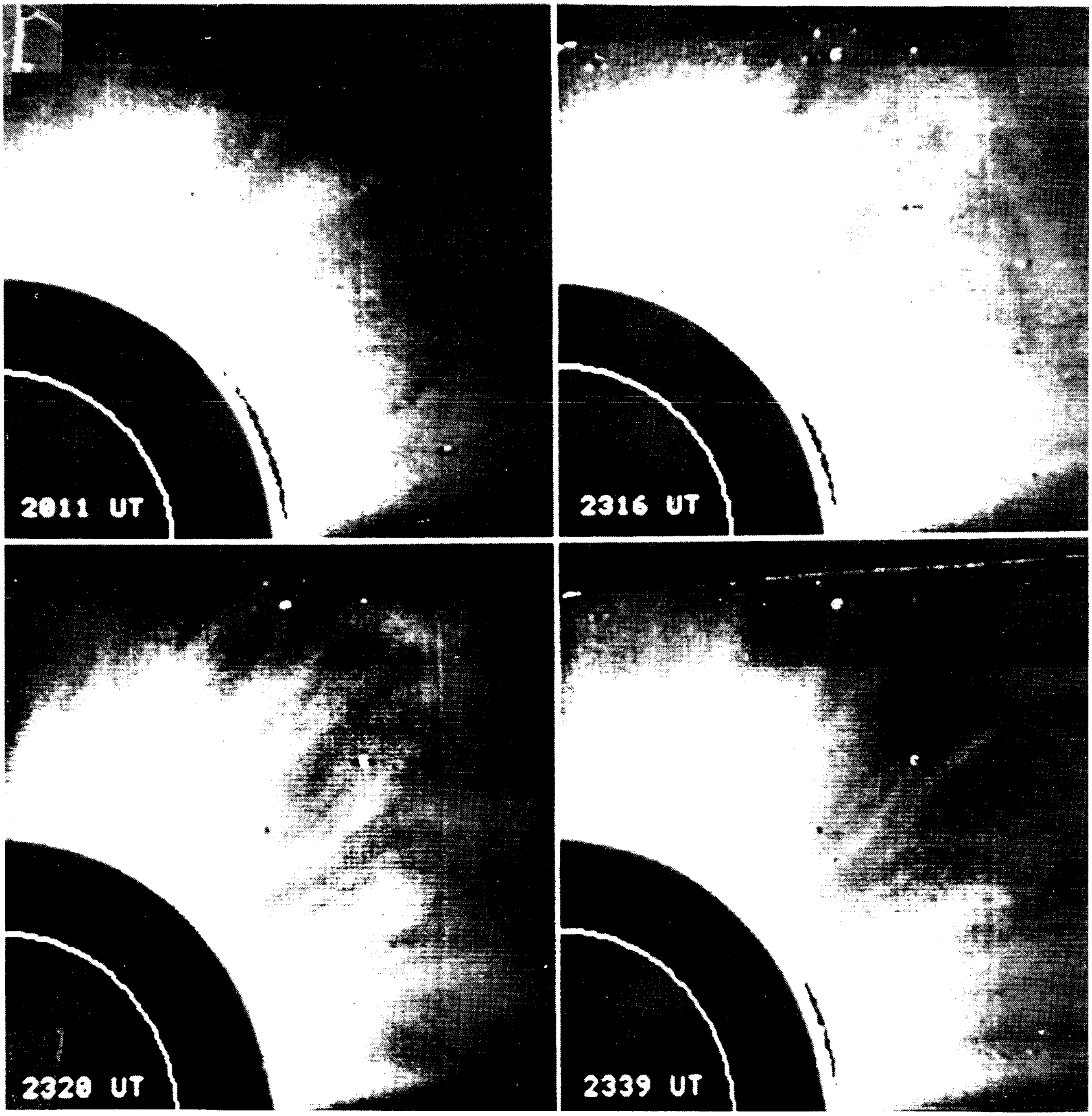

Figure 6.2.19 The evolution of the 9 April 1980 CME coronal transient as observed by the C/P aboard SMM. The images have been obtained at: (a) 2011 UT; (b) 2316 UT; (c) 2320 UT; (d) 2339 UT.

6.2.20. At any given frequency, the source moves toward the disk; the lower frequencies are displaced further to the south.

The Type II burst had large tangential source motions and its frequency drifted at a very low rate. The joint occurrence of low drift rates and large tangential motions in some Type II bursts was first pointed out by Weiss (1963). The slow drift and large tangential motion of the burst sources may be attributable to a shock wave propagating transverse to open magnetic field lines in the corona, possibly along the axis of the arcade of loops seen later in whitelight.

The moving Type IV burst at 80 MHz at 2252 and 2307 UT is also shown in Figure 6.2.20 as source E, associated with the bright blob observed by the C/P in visible light at 2316 UT. We estimate for the blob a plasma frequency of ~23 MHz. On the basis of Figure 6.2.20, we associate the

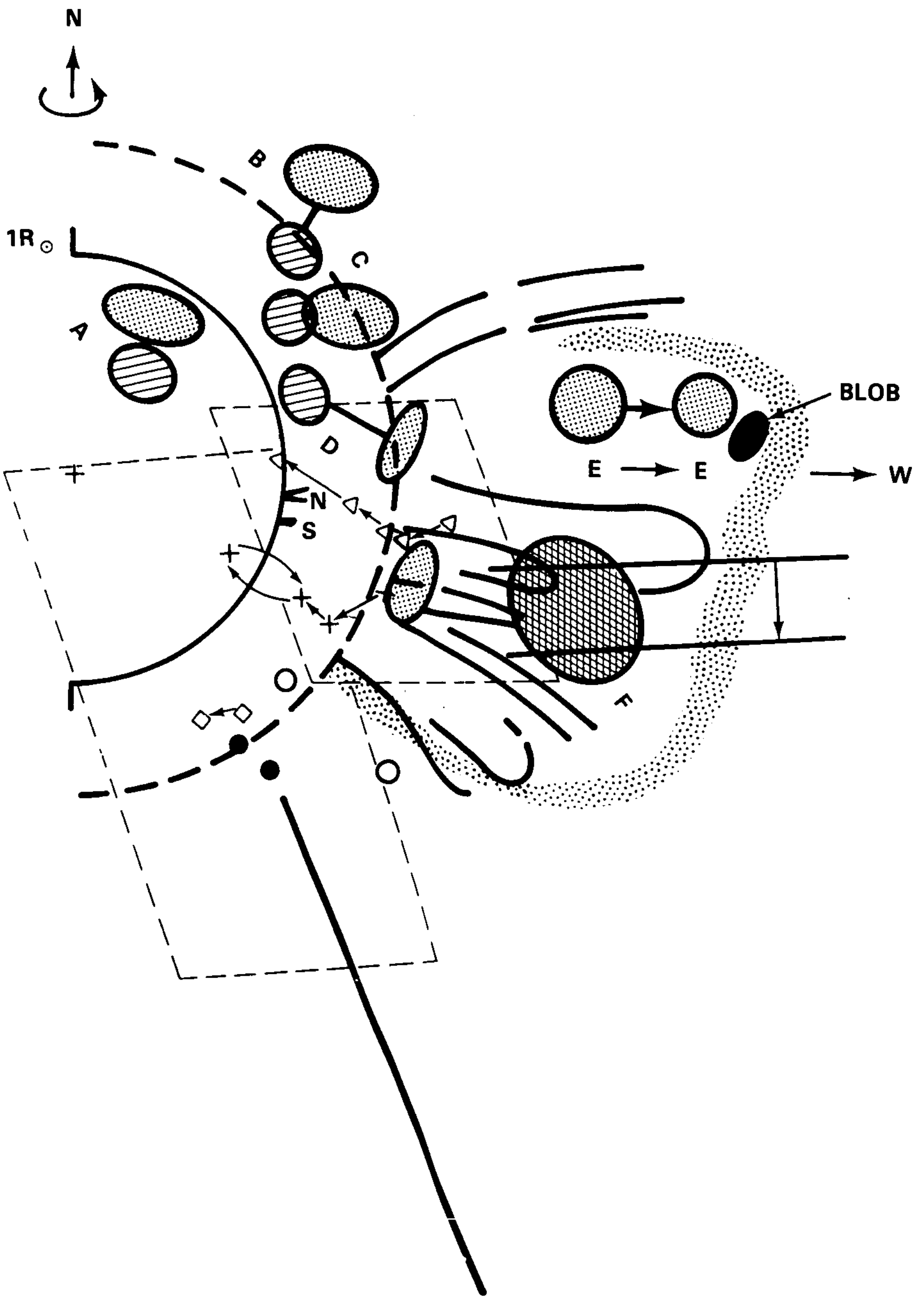

Figure 6.2.20 Composite sketch of the visible light features and radio sources observed during the 9 April 1980 transient. The stationary radio sources A, B, C, and D observed at 160 and 80 MHz with the Culgoora heliograph are shown. The motion of the centroid of the Type II burst at frequencies between 60-50, 50-40, and 40-30 MHz is represented by the triangles, crosses, and squares, respectively. We also show typical source sizes in the 60-50 and 40-30 MHz ranges and the position of the moving source, E (at 2252 and 2307 UT) and F observed at Culgoora and at Clark Lake. The location of one prominence on the limb (N and S), of the whitelight loops, the white light blob (at 2316 UT), the outer edge of the transient, and the streamer south of the transient are all indicated. The open and full circles show the approximate location of the Type II bursts which started at 44 and 55 MHz, respectively.

moving Type IV source with the excess matter contained in the bright blob. Unfortunately, simultaneous observations of the white light CME and moving Type IV source are not available.

We discuss now possible radiation mechanisms for the Type IVM source E. The high degree of polarization of the source (~ 30% RH) rules out second harmonic plasma emission (Dulk and Suzuki 1980). This leaves the possibility of fundamental plasma or gyrosynchrotron radiation. The source was not bright enough to rule out the latter. However, if the plasma frequency was ≥ 40 MHz, then Razin suppression would apply. Since the white light source may have expanded and the true size of the IVM source might be smaller than the 60% contour size, it is reasonable to conclude that the plasma frequency must have exceeded 40 MHz at the time of the 80 MHz observations. Hence, the source may have been due to emission at the fundamental plasma frequency.

6.2.1.8. Helios Spacecraft Observations of Mass Ejection Transients

Prior to the SMM era, when a coronal transient left the outer field of view of a coronagraph, its subsequent evolution could only be guessed at. Yet, knowledge of this evolution is crucial if we are to relate CMEs at the Sun to interplanetary disturbances measured with *in situ* spacecraft, or to the interaction of the ejected plasma with the magnetosphere of Earth. Fortunately, Jackson and Leinert (1985) recognized that the zodiacal light photometers on board the Helios spacecraft, although constructed for another purpose, can be used to "image" mass ejection transients far from the Sun. Because the two Helios spacecraft orbit the Sun, rather than Earth, comparison of their observations with those from Earth-orbiting coronagraphs allows stereoscopic views of the outer solar atmosphere. At least three major CMEs with loop-like characteristics — as observed in Earth-orbiting coronagraphs — were observed with the Helios photometers. An example is shown in Figures 6.2.21-6.2.22 and 6.5.1-6.5.2. The observational technique for Helios is explained in Section 6.5.2.

Figure 6.2.22a is a Helios 2 contour plot obtained at approximately 0936 UT, 25 May 1979. The spacecraft was then 60 degrees behind the west limb of the Sun as seen from Earth. The ejection, which traveled northeast (Figure 6.2.21) as seen from Earth, is observed to the solar north and northwest in Figure 6.2.22a. Helios observations confirm that a depletion followed the ejection. The 15-hour Sun-spacecraft transit time of the leading material gives an outward speed of approximately 750 km s^{-1}. In Figure 6.2.22b, 1.8 days later, more mass is observed to move outward in two features of fairly narrow angular extent — possibly the legs of the loop. The speed of this material is approximately 400 km s^{-1}.

This example is one of three CMEs later observed from Helios that had loop-like characteristics as viewed from Earth. From the Helios observations, we find that either the three ejections have large dimensions along the line-of-sight from Earth (i.e., large extent in heliocentric longitude), or the Helios spacecraft did not observe these features edge on. The shapes of ejections evolve as they move outward from the Sun. For instance, in the 24 May 1979 ejection, general features of what was once a prominence can be distinguished, while the outermost portion of the event was probably not observed in the Helios photometers. There is little evidence of structure in the loop legs even though there are several Helios photometer positions within each leg. The complex loop ejection of 29 June 1980 (shown in Figures 6.5.1 and 6.5.2) can be discerned as at least two outward-moving features when viewed from Helios, although from an Earthly perspective the two overlap and thus do not give rise to an apparently broad angular extent.

6.2.2 Statistical Studies

6.2.2.1 Introduction

Since the discovery of optical manifestations of coronal mass ejections (CMEs), they have been intensively studied to determine their significance, their cause, and their effects on the solar wind. The whitelight coronagraphs on OSO-7 and Skylab observed and documented many properties of CMEs; both operated during the declining phase near the minimum of solar cycle 20. Thus their measurements of, for example, the frequency of occurrence, speeds, and associations to eruptive prominences and/or flares may have been influenced by phase in the solar cycle.

More recently, the solar corona has been monitored nearly continuously by a combination of two coronagraphs and a coronameter for the period prior to the maximum of sunspot cycle 21, through the maximum, and on into the declining phase. The SOLWIND coronagraph on the P78-1 satellite began routine observations in April 1979, followed a year later by the C/P instrument on the SMM satellite. In the summer of 1980, the ground-based Mark-III coronameter on Mauna Lao in Hawaii began routine observations of the inner corona. The combination of these three instruments has produced far more observations of CMEs than were obtained during the previous solar cycle. In addition to studies of individual CMEs, a number of statistical studies have produced some very general conclusions about CMEs. These studies can be divided into three areas: (1) properties of CMEs themselves, (2) properties of the associations of CMEs with solar radio events, and (3) properties of the associations of CMEs with solar X-ray events. In the next three sections, we summarize the results of team members in these three areas.

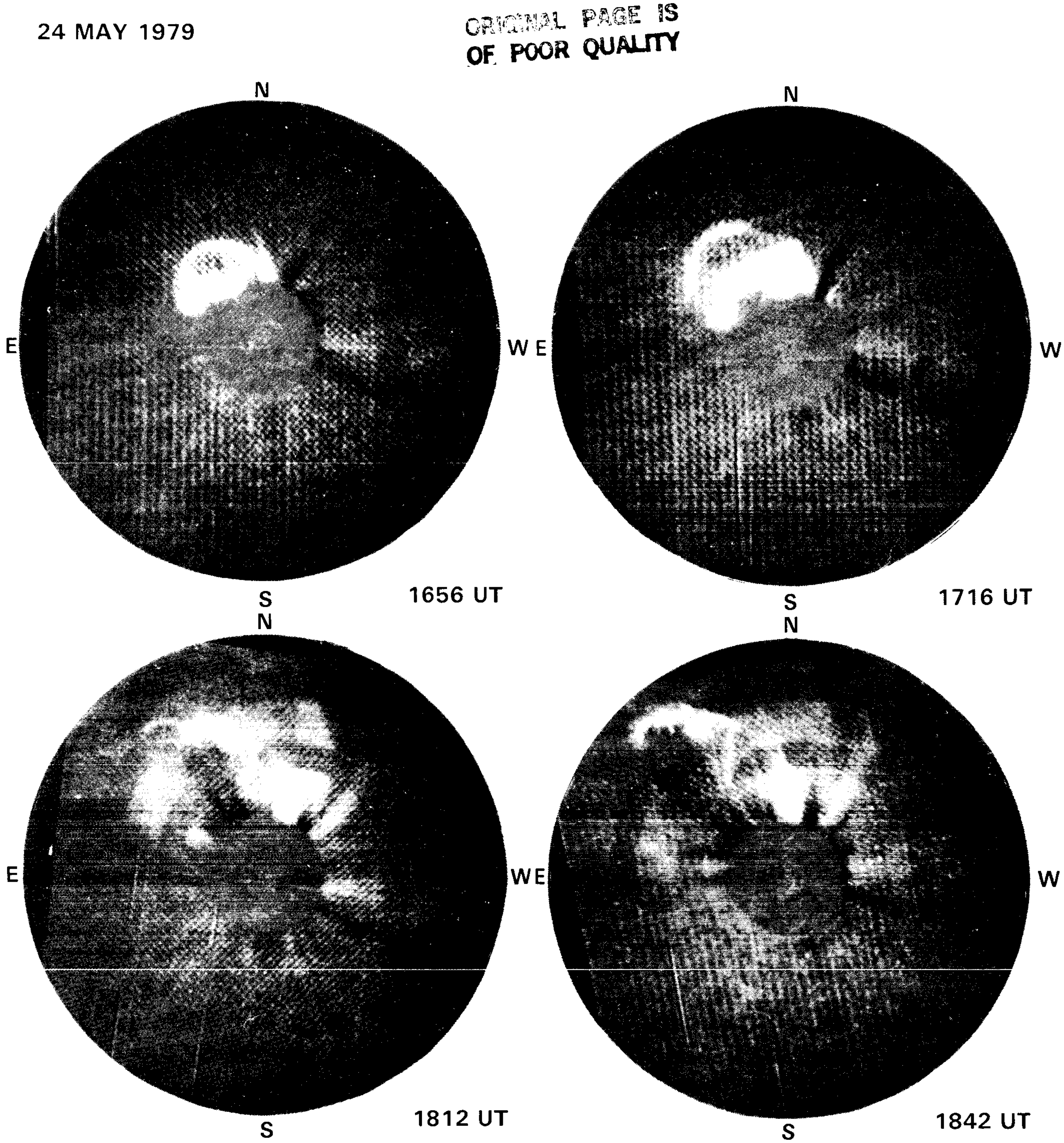

Figure 6.2.21 SOLWIND coronagraph observations of the great solar mass ejection of 24 May 1979. Coronal material forms the loop-like structure ahead of the erupting prominence. The coronagraph's occulting disk is at 2.6 R_0, the outer field of view at 8 R_0. In these difference images a dark void trails the prominence material. These features accelerate to 900 km s^{-1} before leaving the field. A narrow, bright structure moves out very slowly to the north.

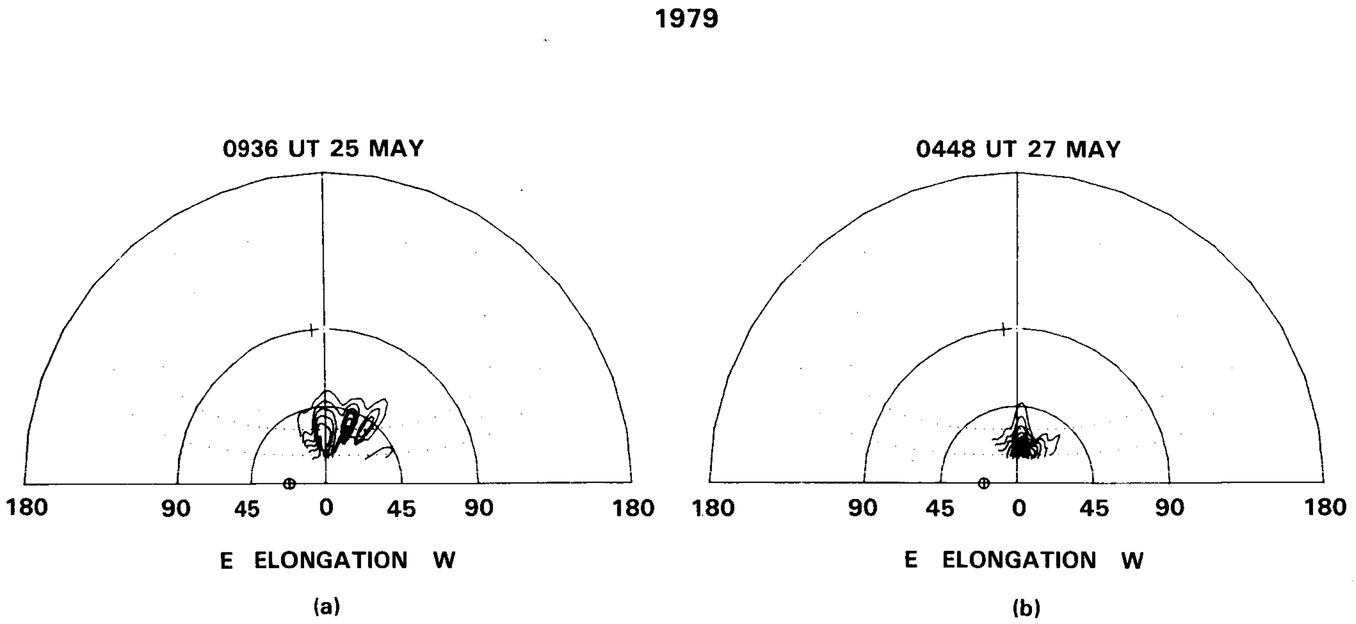

Figure 6.2.22 Helios 2 observations of the 24 May 1980 mass ejection. Visual intensities are converted to excess mass contours which form a coarse image of the ejection (contour interval is 6 × 10^{12} g deg^{-2}). In this presentation the Sun is centered, and the point behind the observer on the spacecraft, i.e., at 180° elongation is represented as the outer circle. The position of the earth (⊕) and the solar pole are indicated relative to the ecliptic plane (horizontal line). (a) Observations of the loop at 0936 UT 25 May. (b) Observations of the legs of the ejection at 0447 UT 27 May. At this late stage of the ejection the high-speed material is well beyond the outer bins of the 31° photometers.

6.2.2.2 Properties of CMEs

The major properties — speed, mass, and energy — of CMEs derived from the Skylab era observations are summarized in a review by Rust, Hildner *et al.* (1980). On average, these properties of CMEs during the solar maximum era have remained the same — the only change appears to be that the maximum and minimum values appear to be more extreme. This difference is presumably due to the increased numbers of CMEs observed rather than any solar cycle dependence. In Figure 6.2.23, from Howard *et al.* (1984), we present distributions of the various CME properties during the period 1979-1981, a period spanning solar activity maximum.

Perhaps the most striking difference between the low-activity and the maximum epochs is the occurrence of CMEs at high latitudes during solar maximum; during the 1973-1974 period, only 10% of the CMEs were observed above 30° latitude and no CME was observed above 48° latitude (Munro *et al.*, 1979). In contrast, both SOLWIND observations (Sheeley *et al.*, 1980; Howard *et al.*, 1985) and SMM observations (Hundhausen *et al.*, 1984a; Wagner, 1984) reveal CMEs appearing at position angles excluded during the earlier epoch. In the SOLWIND set of observations, the average angular span or extent in the plane of the sky is 45° compared to 28° for the Skylab CMEs. In comparing the absolute numbers, it should be noted that the SOLWIND observations of angular span were made higher in the corona than were the Skylab and SMM observations. Nonetheless, the trend toward larger CMEs during the solar maximum is clearly present. We speculate that the presence of the large polar coronal holes excluded CME emission from high-latitude position angles during the near-minimum Skylab and OSO-7 missions.

The most extreme example of CMEs with large angular spans is the class of "halo" CMEs (Howard *et al.*, 1982). This class of CMEs, about 2% of all of the SOLWIND CMEs, is distinguished by emission surrounding the occulting disk. The interpretation of these events is that the brightness enhancements seen at nearly all position angles around the occulting disk are due to CMEs emitted nearly Earthward from somewhere near the center of the solar disk; the excess brightness is projected onto a large range of position angles in the plane of the sky.

The frequencies of occurrence of CMEs inferred from the C/P and the SOLWIND coronagraphs differ from the solar minimum value and from each other. From an analysis of C/P data, Hundhausen *et al.* (1984a) obtain an average rate of 0.9 CMEs/day for 1980, whereas Howard *et al.* (1985) analyze SOLWIND data to obtain an average rate of 1.8 CMEs/day for 1979-1981. Recall that Hildner *et al.* (1976) obtain a rate of 0.34 CME/day for the Skylab data.

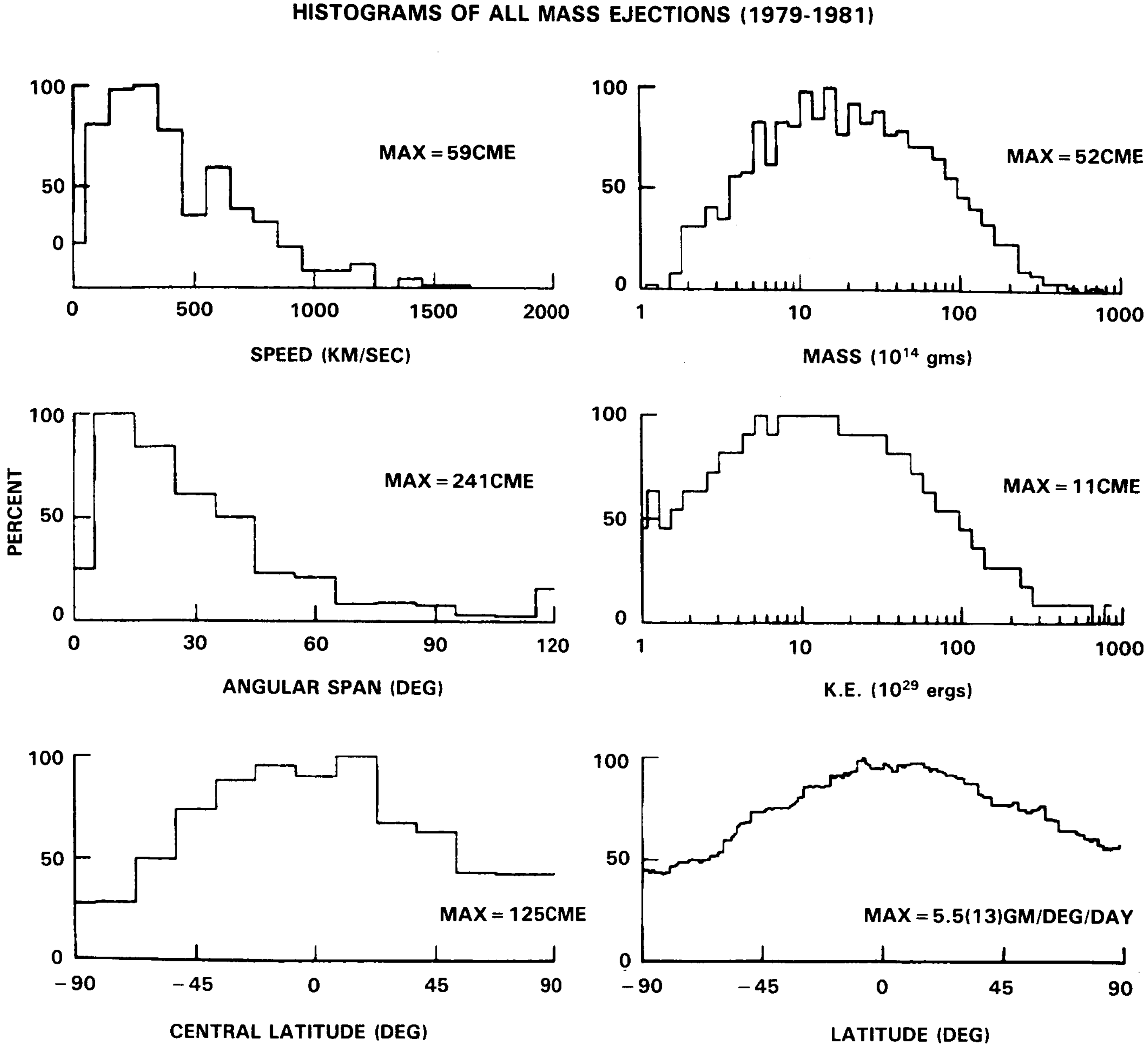

Figure 6.2.23 Properties of all CMEs during the interval surrounding the maximum of the solar cycle, 1979-1981. The distributions of speed, spread, central latitude, mass and kinetic energy are plotted as histograms. Each plot has been normalized to 100% of the maximum number of CMEs. The maximum values used in the normalizations are indicated on the plots. The sixth distribution gives the average mass ejected into each degree of latitude. Also, the plot is normalized to an average daily ejected mass of 5.5 × 10^{13} gm/deg/day. To derive the daily ejected mass distribution, the correction for instrumental duty cycle has been applied. Note that all angular measurements are made projected in the plane of the sky.

Hundhausen *et al.* recompute the Skylab rate as 0.7 CME/day, using the same criteria used for the SMM analysis. From this, they conclude that the CME rate had not increased in direct proportion to the change in Zurich sunspot number. Howard *et al.*, while finding a higher rate of CME occurrences, also do not find an obvious correlation between fluctuations in the sunspot number and fluctuations in the CME rate.

Though a detailed comparison of the rates inferred from the C/P and SOLWIND instruments during the period of overlapping observations has not been completed, useful comments can be made about the difference between the rates. SOLWIND observers used a differencing technique, subtracting an earlier image from the one being considered, to search systematically through the data and identify the occurrence of CMEs; C/P observers used the direct coronal images to identify the occurrence or non-occurrence of a CME. The direct images were also used by the Skylab observers. Thus, SOLWIND results are biased to include fainter events than might be included in C/P and Skylab result. On the other hand, since the SOLWIND observations extend from 2.5 to 10.0 R_0, one could envision that, because CMEs fade with height, the contrast of a CME above the background K+F coronal emission for SOLWIND might be less than the contrast of the same CME in the Skylab and C/P observations which extend from approximately 1.6 R_0. Thus, the Skylab and C/P analyses using direct images of the inner corona might include fainter CMEs than detected in undifferenced SOLWIND images covering the outer corona.

6.2.2.3 Association of CMEs with Type II and IV Solar Radio Bursts

A meter-wave Type II radio burst is generally believed to indicate the presence of a shock front in the corona. The speeds of many CMEs in the corona exceed the local Alfven velocity and therefore are expected to drive shocks. Prior to the recent observations at solar maximum, the shocks were generally assumed to occur at appropriate standoff distances ahead of the leading edges of CMEs (e.g., see reviews by MacQueen, 1980; Maxwell and Dryer, 1982). For Skylab-era CMEs, Gosling *et al.* (1976) find that about 85% of the CMEs with speeds greater than 500 km s^{-1} are associated with Type II and/or Type IV radio bursts, and that these bursts are associated only with those CMEs whose speeds are greater than 400 km s^{-1}. From another statistical study of the associations of Skylab CMEs to other solar phenomena, Munro *et al.* (1979) find that nearly all Type II or Type IV bursts occurring within 45° of the limb are associated with CMEs.

Interestingly, these close statistical associations found for the Skylab era are not confirmed by the recent observations (Sheeley *et al.*, 1984 and Kahler *et al.*, 1984a). Thus, the pre-maximum picture of the relationship of CMEs to Type II and IV radio bursts is, at least, confused. Sheeley *et al.* (1984) and Kahler *et al.* (1984a, 1985a), in comparing SOLWIND CMEs with metric Type II bursts, find that about 60-70% of Type II bursts were associated with CMEs and 30-40% were not. On the other hand, about 40% of all CMEs whose speeds exceeded 450 km s^{-1} had no associated Type II. Thus, a class of Type II bursts exists for which no visible CME was produced, and, conversely, a class of fast CMEs exists for which no associated metric Type II emission was observed. One is tempted to speculate that backside events might obscure about half of the Type II bursts. However, Sheeley *et al.* (1984) find 5 cases in the Culgoora time zone and Kahler *et al.* (1985a) find 15 cases in all time zones, in which an H-alpha and 1-8A flare can be associated with the CME, but for which no Type II was observed.

The association of Type II bursts with fast CMEs argues for a piston-driven model of Type II shocks. Both Sheeley *et al.* and Kahler *et al.* suggest that variations in the ambient magnetic field might give rise to variations in local characteristic speeds; such variations might enable a fast CME to be travelling locally sub-Alfvenic, and, therefore, be ineffective in producing Type II emission. However, as Kahler *et al.* point out, in the piston-driven model, CMEs of larger angular width would pass through larger regions of the corona and thus be more effective than smaller CMEs in finding local regions in the corona where the Alfven speed was appropriate for producing Type II emission. No correlation between CME size and Type II emission is found, though a correlation is found between CME brightness and Type II burst association.

Arguing against a model which suggests that Type II bursts come from shocks driven by CMEs are several studies of speeds, timing, and other associations. For at least two events for which simultaneous, or near simultaneous, observations of a Type II burst and its associated CME are available (Gergely, 1984; Gary *et al.*, 1984) the speed of the CME is lower than that of the Type II burst source. Wagner and MacQueen (1983) note that in some events the Type II is seen well below the top of the CME; they propose to account for this disparity by suggesting that the CME starts to rise first. Then, somewhat later, the impulsive phase of energy liberation generates a shock which propagates up through the CME causing Type II emission when the shock encounters the high-density regions associated with the legs of the CME. Cane (1984) extended the Wagner-MacQueen hypothesis to account for the observations of interplanetary Type II bursts and interplanetary shocks. Kahler *et al.* (1985) find the peak strength of the accompanying 3-cm burst is as important as the CME speed in determining the Type II burst association. These studies support the hypothesis of Wagner and MacQueen that the CME does not drive the shock which, in turn, is responsible for any associated Type II burst. In this view, the CME is simply a result of the big flare syndrome (Kahler, 1982) in which large, energetic events are more likely to be associated with other large, energetic phenomena, but without a direct cause and effect relationship.

Additional evidence is offered by Gergely (1984), who compares the velocity distributions of Type II associated CMEs observed with the Skylab and P78-1 coronagraphs (Rust, Hildner *et al.*, 1980; Sheeley *et al.*, 1984) to the velocity distribution of all Type IIs observed during the period 1968-1982 (Gergely, 1984). Figure 6.2.24 shows the distributions for CMEs from Skylab (shaded) and for CMEs from SOLWIND, while Figure 6.2.25 shows the distribution of speeds of Type II bursts. Some representative parameters of the distributions are given in Table 6.2.3.

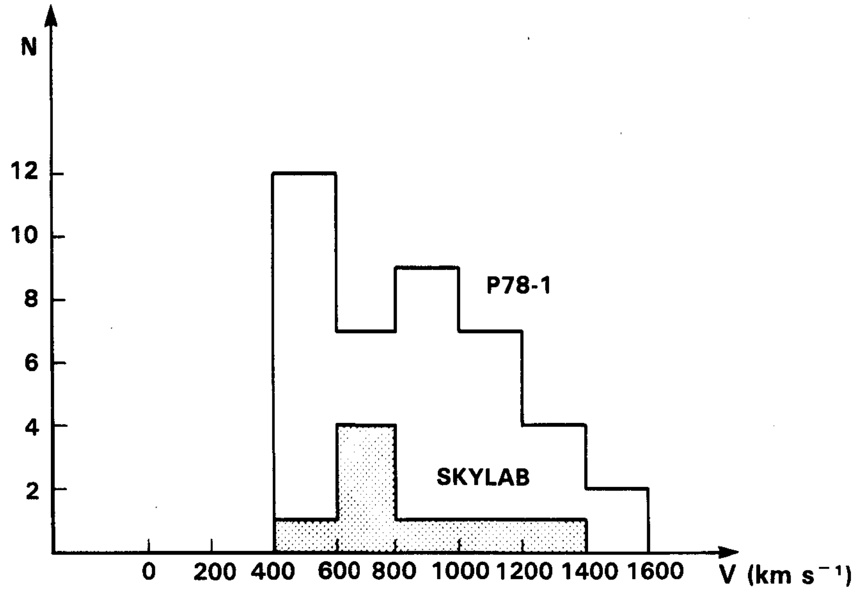

Figure 6.2.24 Speed distributions of the leading edge of CMEs accompanied by Type II bursts. The shaded distribution indicates the speeds of CMEs observed with the Skylab coronagraph; the unshaded distribution indicates the speeds of CMEs observed with the P78-1 coronagraph. Note the absence of any speeds slower than 400 km/s and the similarity of the distributions during solar minimum and solar maximum.

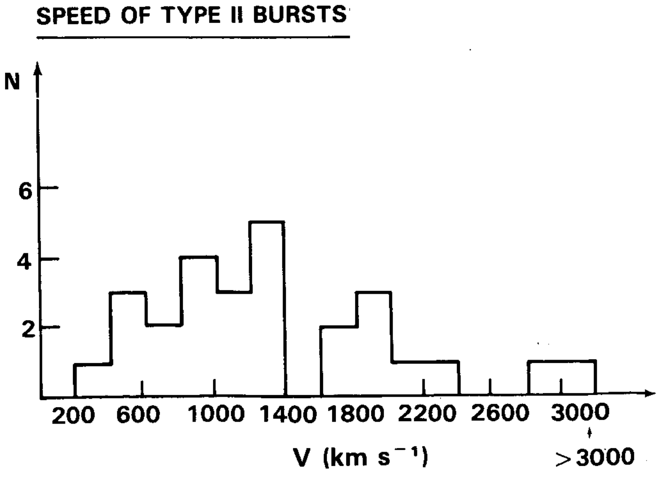

Figure 6.2.25 Distribution of Type II velocities. The Type II speeds were compiled from a literature search of all Type II speeds. Note the very large spread in speeds, and the maximum in the 1200-1400 km/s bin.

Table 6.2.3 Comparison of Speeds of CMEs, Type II and Type IV

	CMEs Observed With		Metric Radio Bursts	
	Skylab	P78-1	II	IV
Number of Events	8	40	26	46
Lowest Speed (km s^{-1})	450	400	370	100
Highest Speed (km s^{-1})	>1200	1500	4900	1300
Mean Speed (km s^{-1})	795	825	1380	515
RMS Dispersion (km s^{-1})	255	293	720	286

From a comparison of these two figures, one sees that the velocity distribution of Type II associated CMEs is similar at the declining and maximum phases of the solar cycle. Note that the distribution of all CMEs (Gosling *et al.*, 1976; Howard *et al.*, 1985) is also similar for these two phases. The average speed of the Type II bursts exceeds the average speed of the CMEs by about 70%, whereas the rms dispersion of Type II speeds is considerably higher than the rms dispersion of CME speeds. These results should be qualified with the following caveats. Firstly, most Type II speeds have been derived from drift rates and, therefore, depend on the density model (most often the 2x Newkirk streamer model) adopted for the corona. Secondly, the speeds of Type IIs were determined in the 1.5-2.5 R_0 height range, whereas the speeds of CMEs were determined at greater heights. Thirdly, the Type II speed determinations are very inhomogeneous in terms of method, instrument used, phase of the solar cycle, etc., as contrasted with the CME speed determinations which were very homogeneous.

Stewart (1984) compared the positions of Type II bursts observed with the Culgoora radioheliograph at 160 MHz with the positions of filaments and optical flares for the years 1980-1982. Figures 6.2.26 and 6.2.27 show Carrington plots of the Type II radio positions and the filament channels for 1980 and 1981. The circles give the approximate positional error of the Type II burst (5 °). Stewart finds that 93% of the Type II bursts occurring above the limb lie within 5 ° of a filament channel and that 51% lie within 1 °. For disk events, 86% of the Type II positions lie within 5 °. In a similar comparison with optical flare positions, he finds that 83% of the Type II burst positions occurred further than 10 ° from the flare site. Since the local Alfven speed is expected to be lower in a streamer than outside it, it is likely that an MHD wave will steepen into a shock at the streamer. Thus, Stewart's results are consistent with the concept of the Type II emission being generated by the interaction of an MHD wave with a helmet streamer overlying the magnetic neutral line (Stewart, 1984).

Kahler *et al.* (1985) question whether the Type II bursts associated with H-alpha flares but not with CMEs could be pure blast waves. For pure blast waves, the Type II bursts should correlate with the impulsive release of energy as measured by the size of the 3-cm peak flux. However, for a thick target model, Kahler *et al.* estimate that small Type II bursts have only one-tenth to one-hundredth the threshold energies necessary for shock formation in large flares. Also, only 20% of the large 3-cm bursts were associated with reported Type II bursts. Thus, Kahler *et al.* conclude that the relationship between impulsive phase energy releases and shocks identified by Type II bursts is poor.

At least two Type IV bursts have been identified with dense plasmoids observed within, or near the leading edge of loops or bubble-shaped CMEs (Gergely *et al.*, 1984; Stewart *et al.*, 1982). Gergely (1984) examined the statistical distribution of Type IV burst velocities for the period 1968-1982, as shown in Figure 6.2.28. Some parameters of the distribution are given in Table 6.2.3. Comparison of the Type IV speed distribution with the distribution of speeds for all CMEs implies that (a) the mean speed of the Type

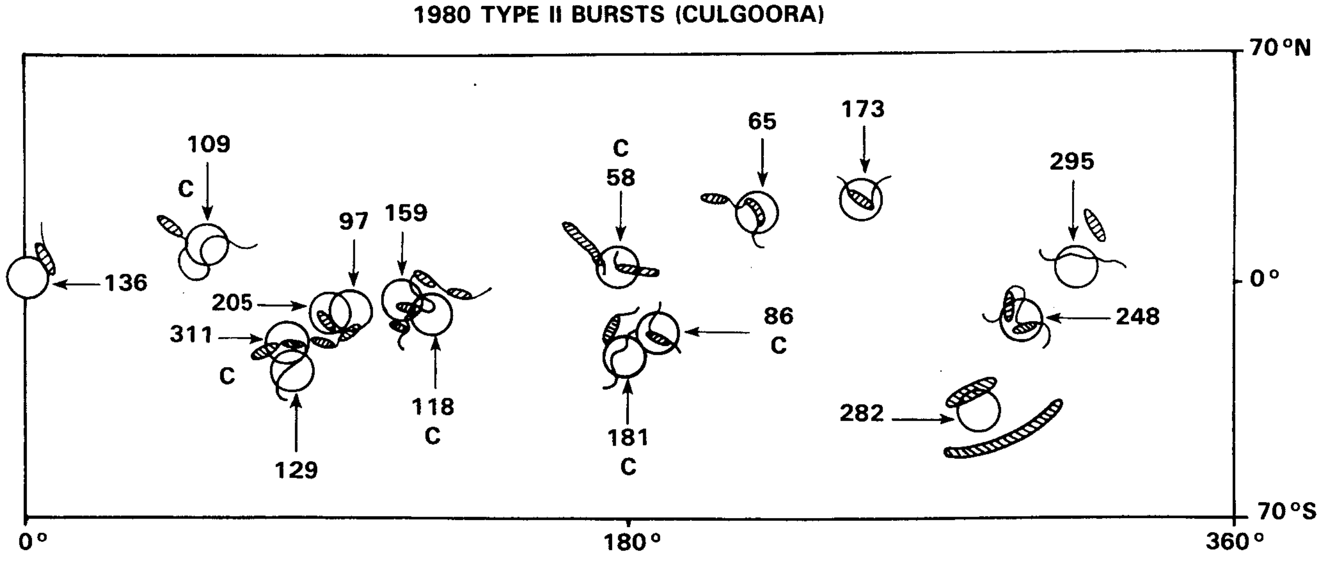

Figure 6.2.26 Carrington plots of the positions of Type II bursts and H-alpha filament channels for 1980. The position of the Type II bursts were derived from the Culgoora 160 MHz radioheliograph and are indicated with circles, the size of which indicates the estimated positional error. The positions of the H-alpha filament channels are indicated by the hatched regions and thin lines. The numbers are the day of year on which the Type II burst occurred. The letter "C" indicates those events associated with a CME observed either with the SMM C/P or the P78-1 SOLWIND coronagraph. Note the close association of the positions of Type IIs and the filament channels.

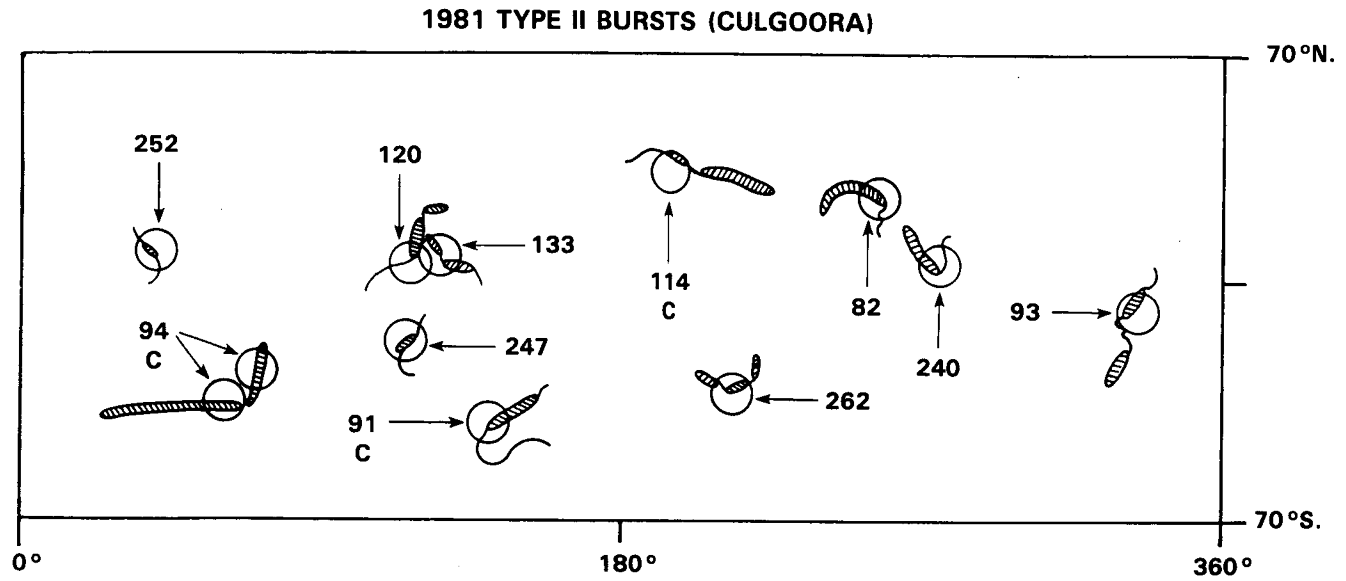

Figure 6.2.27 Carrington plot of the position of Type II bursts and H-alpha filament channels for 1981. The format is exactly the same as for Figure 6.2.26. Again, note the close association of the positions of Type IIs and the filament channels.

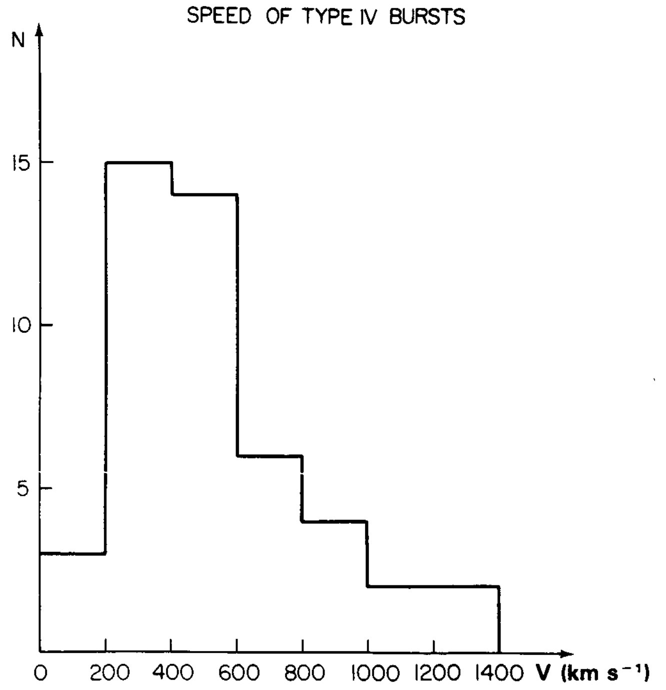

Figure 6.2.28 Speeds of Type IV bursts during 1968-1982. Note the broad maximum of speeds from 200-600 km/s.

IVs is less than the mean speed for all CMEs, and (b) the rms dispersions of the speed distributions of CMEs and Type IVs are identical. Thus, the moving Type IV bursts appear to be moving outward (sometimes to as high as 5 or 6 R_0 before fading) either slightly behind, or with the leading edge of the CME. In contrast with those inferred for Type II bursts, the speeds of Type IVs are not dependent on coronal density models; consequently they are more reliable than the Type II speeds. Since only a small number of instruments have been used to determine their speeds, the Type IV observations are also more homogeneous.

6.2.2.4 Association With Soft X-Rays

The long-duration, soft, X-ray events during the Skylab mission were usually accompanied by coronal mass ejections (see the review by Rust, Hildner *et al.*, 1980). Sheeley *et al.* (1983a) examined the relationship of the SOLWIND CMEs to the 1-8 A flux from the SMS-GOES satellite for the period 1979-1981. They find that the probability for a CME to be associated with an X-ray long-duration event increases as the duration of the X-ray event increases — from about 25% for X-ray events less than 2 hours long to 100% for X-ray events lasting longer than 6 hours. The distribution of X-ray durations of those X-ray events with CMEs has a broad peak centered at about 3.5 hours, with a median value of about 4.5 hours. Thus, the longer an X-ray event lasts, the more likely that a CME accompanies it.

6.3 The INITIATION OF CORONAL MASS EJECTIONS

6.3.1 Introduction

Surprisingly little is known about the initiation of coronal mass ejections. Although the first flare observation took place over a century ago (Carrington, 1859), and we have studied the passage of material through the solar corona for several decades (e.g., Payne-Scott, Yabsley, and Bolton, 1947–Type II; Wild, Roberts, and Murray, 1954–Type III; Tousey, 1973–coronal transients), their relationship is poorly understood. In asking how a mass ejection is initiated, we are requiring to know (a) the original location of the mass which is to be ejected, (b) when the onset is triggered, (c) the time-height profiles for the various components of the ejection, and (d) their relationship to other solar activity. With these observational questions answered we may then confidently postulate the basic mechanism behind these events.

A coronal transient is characterized by changes in brightness of regions of the corona with time-scales of tens of minutes. The majority of such events are thought to be indicative of CMEs, outward mass motions with velocities of < 1000 km s^{-1}. These events are most often associated with eruptive filaments whether or not they are flare associated.

In this section, we discuss the relative timing of the various components of ejecta and compare the sequence of events to surface activity. Of particular interest is the pre-flare role of ejecta and their association with pre-flare surface activity. We then describe some recent observations relating to below-coronagraph images of ejecta and, finally, due to the quality and quantity of data obtained for an event on 30 March 1980, we describe this event in some detail, emphasizing different aspects of the event than those treated in Section 6.2.1.5.

6.3.2 Relative Timing

The relationship between a solar active region, its flare activity, and related mass ejections cannot be sensibly modelled in the absence of detailed studies into the relative timing of the various active phenomena. There are problems, however, in obtaining suitable measurements. The use of externally occulted whitelight coronagraphs, which obscure the low corona, has tended to detach the study of the coronal response to mass motions from the study of solar surface phenomena. Furthermore, the usual plane-of-sky projection view introduces complications in matching a CME to its associated surface activity and produces a selection effect in favor of limb events which, due to their location, are not ideally suited to other types of investigations.

6.3.2.1 Eruptive Filaments

Filaments often exhibit pre-flare disturbances (Martin and Ramsey, 1972; Webb, Krieger, and Rust, 1976), typically showing some upward motion and internal material motion tens of minutes prior to flare onset. Heyvaerts, Priest, and Rust (1977) noted that at the time of a flare's impulsive phase, "...twisting motions in the filament are often observed. Occasionally the filament remains, though disturbed somewhat, but usually it rises (with a much greater acceleration than before), untwists or flies apart, and disappears completely."

An ongoing study begun at the SMM Workshop by Kahler, Moore, Kane, and Zirin is an investigation into the relationship between the flare impulsive phase and filament eruption. A close temporal relationship has long been known (Svestka and Fritzova-Svestkova, 1974) between the onset of Type II bursts, indicative of shocks, and the impulsive phase as measured in microwaves or hard X-rays. This has led to suggestions that an impulsive phase "explosion", perhaps generated by a rapid chromospheric deposition of energy carried by electrons of $E > 10$ keV, may initiate the shock. In the model of Lin and Hudson (1976) for large flares, this explosion also produces the mass ejection. This concept has also been incorporated in numerical hydrodynamical models (see Dryer, 1982). However, filament eruptions have often been thought to be magnetically controlled, and, as mentioned, filament activity tens of minutes before the impulsive phase is well known. Kahler *et al.* seek to resolve the question of just what is the activity in the filament (taken to be indicative of non-potential magnetic fields) at the time of the impulsive phase.

From a four-event subset of flares well-observed both with the University of California at Berkeley's ISEE-3 hard X-ray detector and in H-alpha at the Big Bear Solar Observatory (26 April 1979, 28 May 1980, 25 June 1980 and 27 July 1981), preliminary results show that the filaments rapidly accelerate during the impulsive phase. This acceleration does not seem to be a result or effect of the impulsive phase, nor does it seem to drive the impulsive phase. It appears that a catastrophic magnetic action (presumably reconnection) results in the impulsive phase, and both the particle acceleration and rapid filament eruption are manifestations of this causal action. Kahler *et al.* hope to show the temporal and spacial relationships of the filaments and impulsive phase energetic electrons as clearly as possible in the near future.

If the eruptive filament displays pre-flare activity and then exhibits a violent reaction to events during the impulsive phase, how does this relate to the main body of the CME? The fact that pre-flare filament activity is observed, combined with the fact that coronal material commonly leads the ascending filamentary material (Schmahl and Hildner, 1977; Maxwell and Dryer, 1982), begs the question: what is the relative timing between the main mass ejection onset and the flare onset?

6.3.2.2 Coronal Mass Ejections

One feature of the CME which exhibits pre-flare motion is the so-called forerunner (Jackson and Hildner, 1978; Jackson, 1981), a tenuous, broad envelope of material which leads the main component of the mass ejection. According to Jackson, the entire mass ejection process begins with acceleration of a high altitude, pre-existing structure which becomes the forerunner and ends with the onset of surface eruptions and flare activity. Using Skylab coronagraph data from 15 ejection events, he was able to show that 7 events showed outward motion of tenuous material prior to any surface H-alpha eruption and another 5 exhibited excess mass in the corona prior to an ejection. The other 3 events were rejected for various reasons. No event showed an H-alpha eruption prior to the motion of coronal mass.

In recent years it has been suggested that the main body of the transient also has a pre-flare activation (e.g., Gary, 1982; Wagner, 1983, 1984 and references therein). A thorough investigation into the onset times of several CMEs has been made during the SMM Workshop by Harrison *et al.* (1985). They have been able to confirm, for seven flares observed by the SMM observatory, that the mass ejection onset was prior to the associated flare. Perhaps the most significant fact is that in all of these events the ejection onset appears to be closely associated with a soft X-ray flare precursor. This is illustrated in Figure 6.3.1. Figure 6.3.1a shows the coronal mass ejection altitude history as recorded by the Coronagraph/Polarimeter for an event early on 29 June 1980 (Gary, 1982; Harrison *et al.*, 1985). A projection from a best fit to the data points, assuming no acceleration, indicates that the ejection left the vicinity of the low corona at about 0228 UT, some 5 minutes prior to the soft X-ray burst. The 3.5-5.5 keV intensity, as recorded with HXIS (van Beek *et al.*, 1980) for the flare event (post-0233 UT), and its precursor (pre-0233 UT) associated with this mass ejection, is superimposed onto the figure. The correlation between the mass ejection onset and the precursor is even closer if we assume continuing acceleration in the early stages of the ejection.

The same scenario is found for the 1823 UT flare on 29 June 1980, illustrated in Figure 6.3.1b. The solid line labelled T is the best fit to the mass ejection's altitude as observed with a K-coronameter (Wu *et al.*, 1983; Harrison *et al.*, 1984); projection to the limb region, assuming no acceleration, suggests an onset time of 1811 UT. Harrison *et al.* have attempted to describe the acceleration phase of this ejection by linking the K-coronameter data to ejection heights estimated from soft X-ray images (described later). Again, the HXIS 3.5-5.5 keV record (a, b, c, d) for this flare is superimposed onto the figure. As with the previous flare, the mass ejection is associated with a small event preceding a larger one. In this case the precursory event is a relatively large burst.

These analyses depend upon height vs time plots derived from coronagraph images, and such plots are susceptible to a number of uncertainties. Although the time at which each image is obtained is precisely known, the low contrast of CME features ensures uncertainty of 0.1 R_0 in most height measurements. Furthermore, the variation of a CME's brightness contrast as it moves through the field of view has the potential to introduce a systematic error in measurements of the heights of the CME's leading edge on successive images. Finally, a small error in the inferred speed of a slow CME produces a large change in where the trajectory line intercepts the time axis; that is, a change of five or so minutes in the inferred time of CME start, in the absence of acceleration or deceleration, could result from measurement uncertainties. However, as there is no accepted way to reduce these uncertainties, the data are taken to be as measured.

In addition to showing that for the seven events studied the mass ejections appeared to originate at the time of the flare precursor, Harrison *et al.* have attempted to show that all coronal mass ejections are accompanied by a soft X-ray burst and that a flare *may* follow, usually, some tens of minutes later. They describe an event on 27 June 1980, when a mass ejection, not associated with a flare, left the low corona at the time of a "lone precursor".

Harrison *et al.* point out that the coronal mass ejection/soft X-ray precursor association would be vitiated by the existence of either deceleration of the ejection or high altitude onset. They reject both, the latter on the grounds that the average onset altitude for the seven events analyzed would be 0.66 solar radii above the photosphere, and the former on the grounds that acceleration is frequently detected in coronagraph images — deceleration is rare to non-existent.

6.3.2.3 Summary

To summarize the work of Kahler *et al.*, Jackson, Harrison *et al.*, and others (Webb, Krieger, and Rust, 1976; Dryer, 1982; Schmahl and Hildner, 1977), we make use of a schematic time-plot as in Figure 6.3.2. The lower half of this figure is devoted to the intensity-time curves of the HXIS 3.5-5.5 keV and 22-30 keV energy bands, for a "typical" flare event. A soft X-ray precursor is seen from time A; the hard X-ray burst is seen from time B, just after the onset of the soft X-ray component of the main flare which maximizes at C. Of course, the separation in time between A and B may range from a few to tens of minutes. The top half of the figure shows three height-time plots. The lowest curve represents the location of the eruptive filament, which begins to rise at the time of the precursor but displays more rapid acceleration during the impulsive phase. The middle curve represents the height of the CME's leading edge. We assume that the mass to become part of the ejection is stored in low coronal loops (see, e.g., the model due to Simnett and Harrison, 1985) prior to onset. The structure entraining this mass starts rising at the time of the X-ray precursor, reaching an altitude of about 1 R_0 soon after flare onset. It travels, at any moment, at least as fast as the following filamentary material. The highest curve represents the forerunner's trajectory. The forerunner may well start several solar radii above the photosphere and is accelerated well before B, although the actual timing of the acceleration stage is uncertain.

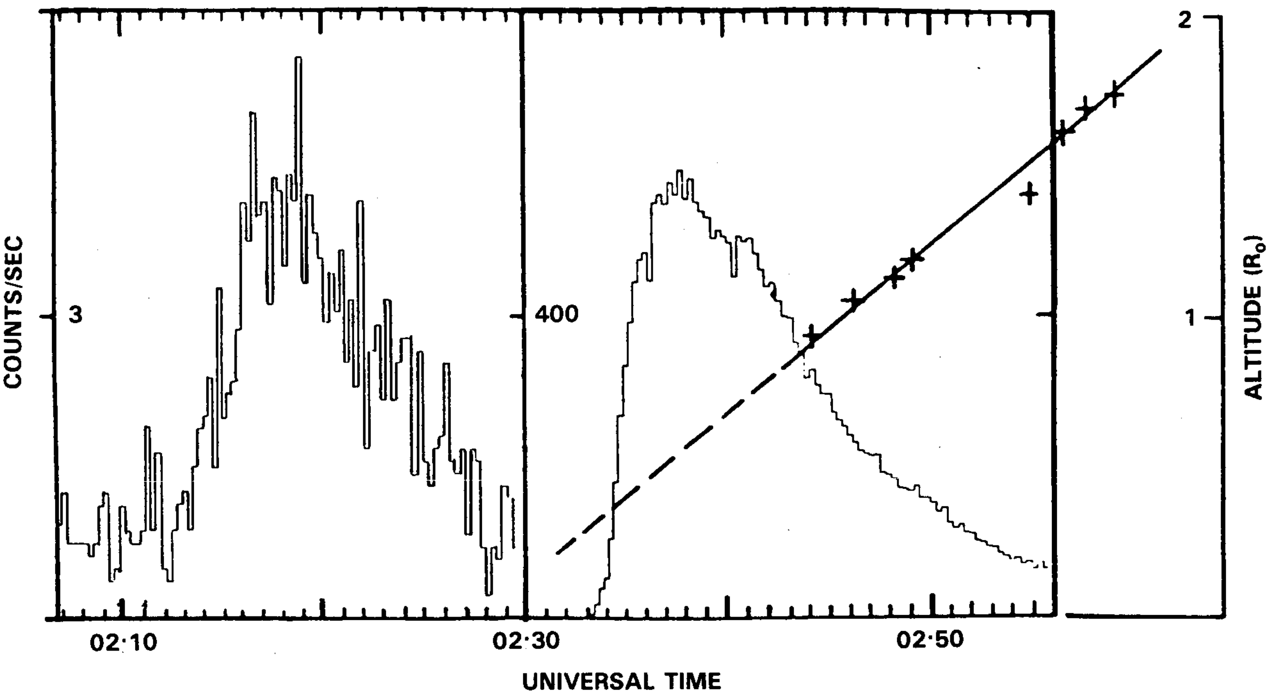

Figure 6.3.1a The relationship between the 0233 UT 29 June 1980 flare and an associated whitelight CME. The 3.5-5.5 keV intensity-time profile is shown for the flare (post-0233 UT) and its precursor (pre-0233 UT), along with the trajectory of the ejection. The solid line is a best fit to the observed leading edge, and the dashed path is a projection assuming no acceleration. The 3.5-5.5 keV background level is 0.05 count s^{-1}.

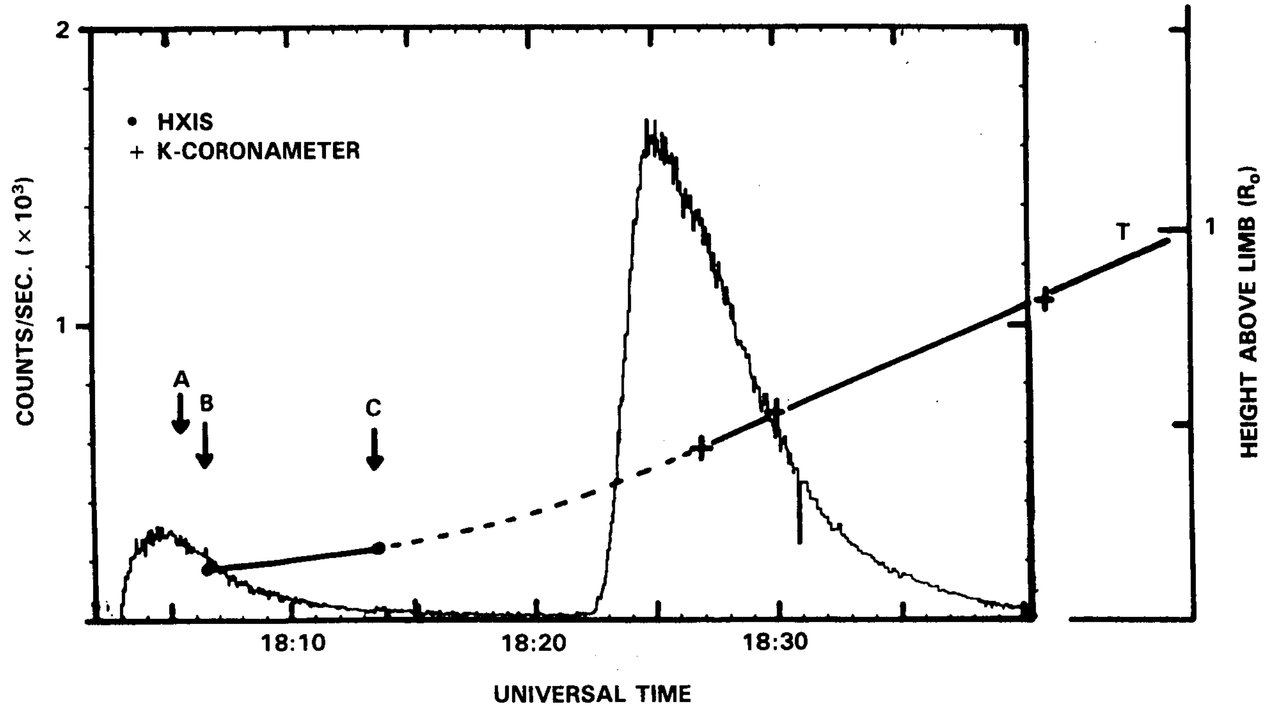

Figure 6.3.1b The relationship between the 1800 to 1900 UT 29 June 1980 flares and associated coronal activity. The 3.5 to 5.5 keV intensity-time profile is shown for the 1823 UT flare and the smaller 1803 UT event. Superimposed onto this are the altitude histories of a whitelight coronal mass ejection (T) and an X-ray transient as shown in Figure 6.3.3.

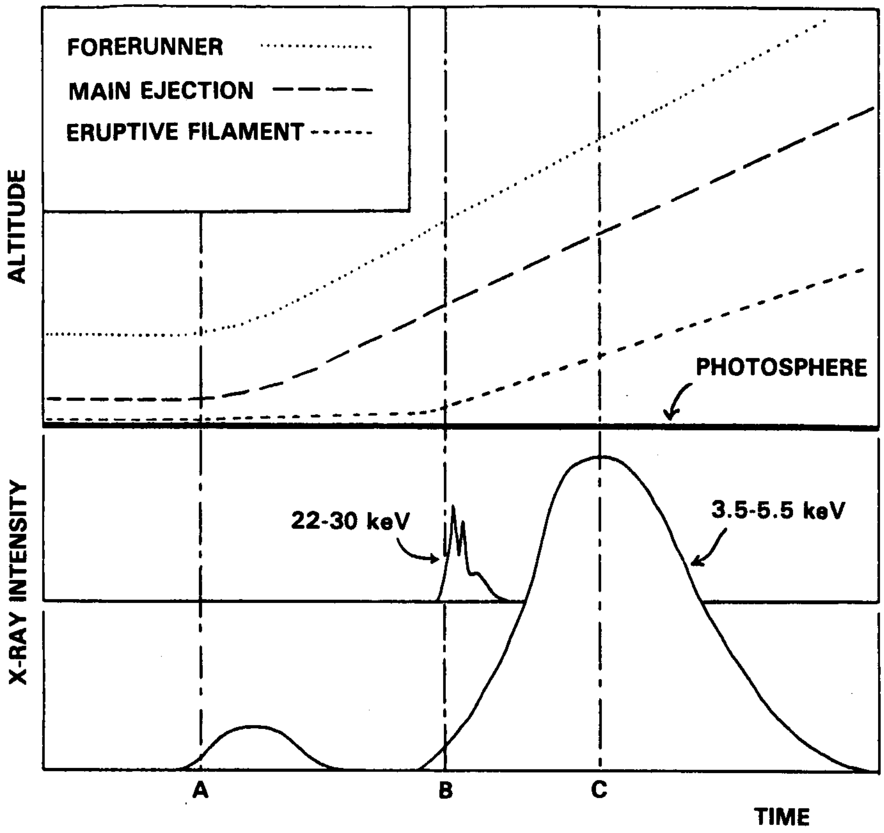

Figure 6.3.2 The relative timing between the X-ray signatures of a solar flare and the mass ejection onsets, shown schematically. The curves in the lower half of the figure represent "typical" soft and hard X-ray intensity profiles for a flare event. The energy bands shown are the highest and lowest bands of HXIS. A soft X-ray precursor is evident from A, the hard X-ray burst onset is at B, and the maximum intensity of the soft X-ray flare is at C. The upper plots show the heights of the eruptive filament, the main mass ejection, and the forerunner on the same time axis.

6.3.3 Low-Height Observations Relevant to Mass Ejections

We define low-height observations as those which view the atmosphere at altitudes below the occulting discs of whitelight coronagraphs, i.e., below about 150,000 km. In this category we include observations of sprays, surges and filamentary eruptions (Rust, Hildner, *et al.*, 1980). Whereas many surges are neither flare related nor result in the escape of material into the high corona, sprays and filamentary eruptions are commonly associated with coronal mass ejections (Munro *et al.*, 1979), sprays originate in flares, and it has been suggested that sprays and filamentary eruptions are not fundamentally different (Rust, Hildner, *et al.*, 1980). These phenomena are associated with the lowest altitude profile of Figure 6.3.2. What observations may be made to observe the low-height behavior of the main coronal mass ejection?

6.3.3.1 X-ray Coronal Transients

Using images from the HXIS in the 3.5-5.5 keV energy range, Harrison, Bentley, Phillips, and their colleagues (Harrison *et al.*, 1984) believe they have identified X-ray-emitting counterparts of whitelight CMEs (cf., Rust and Hildner, 1976). For three limb flares which were well observed by the SMM instruments on 29 June 1980, they examined temporal changes in the X-ray intensity of the low corona. Evidence was found for two classes of X-ray coronal transients.

Figure 6.3.3 shows an X-ray transient observed from about 1806 UT on 29 June. Panel a is a 7.7s exposure from 1806 UT, during the precursor event illustrated in Figure 6.3.1b. The subsequent panels show exposures from 1806, 1813, and 1818 UT, respectively. These images clearly show an X-ray coronal transient ascending at <40 km s^{-1}. The altitudes of the X-ray disturbance (the crosses in Figure 6.3.3)

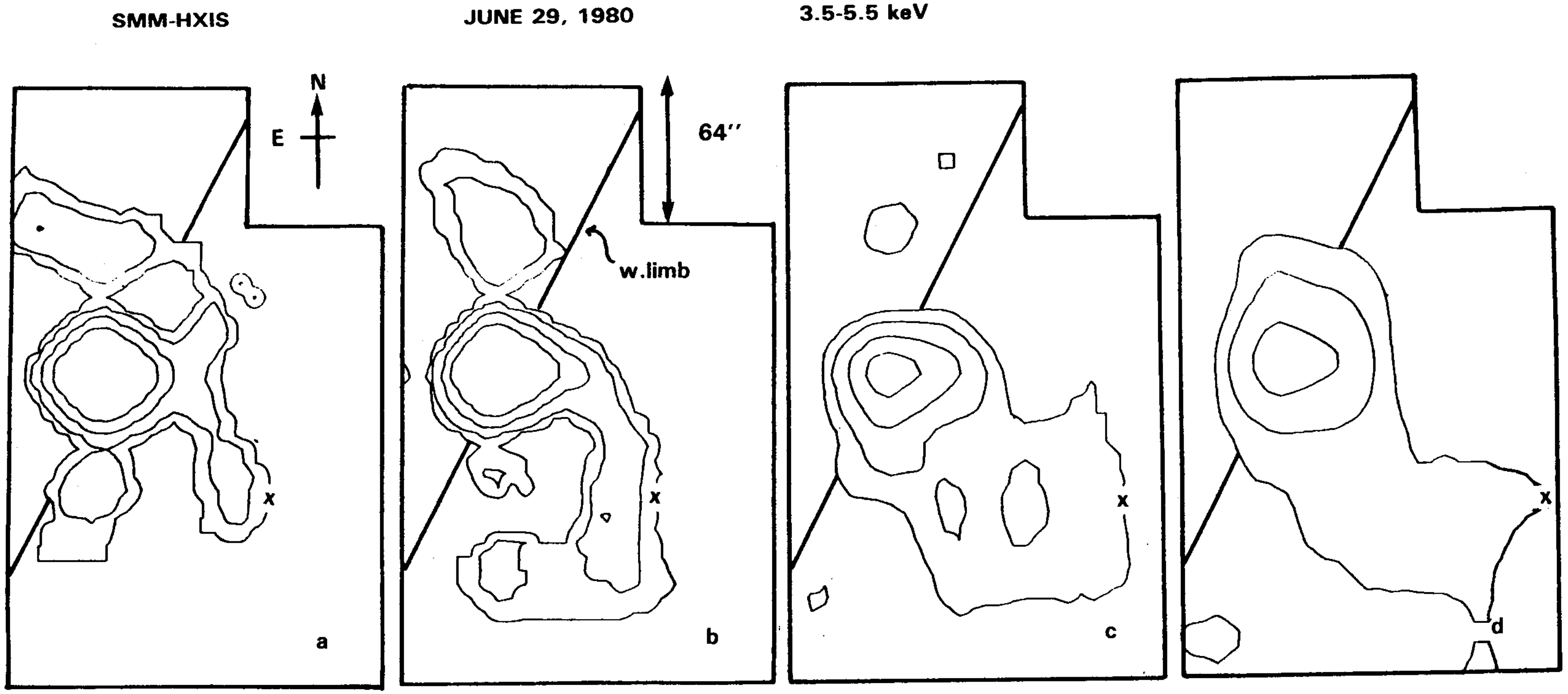

Figure 6.3.3 An X-ray transient seen in the precursor phase of the last 29 June 1980 flare. A series of HXIS 3.5 to 5.5 keV images are shown: (a) 18:05:48 UT, exposure duration 7.7s; (b) 18:06:16 UT, exposure 77s; (c) 18:13:10 UT, exposure 3.33s; and (d) 18:18:07 UT, exposure 32.3s. Intensity contours are plotted at 20, 5, 1 and 0.2 counts/sec. The background level is 0.005 counts/sec per pixel. The altitudes of the crosses are plotted in Figure 6.3.1b.

are plotted in Figure 6.3.1b. Under the assumption that the material producing the X-ray enhancement is part of the subsequent whitelight CME, the altitudes estimated from HXIS and C/P data are suggestive of acceleration in the early stages of the ejection.

A second X-ray transient is illustrated in Figure 6.3.4 for the flare of 1041 UT on 29 June; it is seen to be much more intense than the first example. The first image is accumulated during 9.2s after 1043 UT. The subsequent images are from 1046 and 1053 UT, respectively. They reveal a transient which is travelling into the corona at 60 km s^{-1}, during the main phase of the flare (see Figure 6.3.1a).

Harrison *et al.* believe these X-ray transients are due to material motion. In support of this, they demonstrate that as the intensity enhancements move outward, the variation in the intensity levels of the two lowest energy bands of HXIS suggests that the emission is coming from regions of significant density enhancement.

The X-ray transients analyzed by Harrison *et al.* fall into two classes. Events in the first class, like the 1806 UT 29 June event are observed during the precursor stage and are associated with the onsets of the main coronal transients. Events in the second class, like the 1041 UT 29 June event, occur during the main phases of flares and are not associated with whitelight transients or fresh energy releases. It is thought that this second class is due to hot material rising with the reconnecting magnetic fields above a flare site.

6.3.3.2 High-Velocity X-ray Ejecta in Flares

A study, principally made by Bentley and Phillips, has recently focused on the identification of high-velocity, low-altitude, X-ray emitting ejections which occur at flare onset times. Observations with the Bent Crystal Spectrometer (BCS) on SMM have revealed spectrally discrete, short-lived emission line features near intense parent lines in solar flare X-ray spectra for three large flares: 29 June 1980 at 1041 and 1823 UT and 21 May 1980 at 2100 UT. A preliminary account of them has already been given by Bentley *et al.* (1984). The line displacements, assumed to be Doppler shifts from the parent lines, indicate line-of-sight velocities of 300-400 km s^{-1}. The observed shifts imply surprisingly large speeds, especially for the two limb flares of 29 June, when one might think that most material would be ejected radially rather than along the line of sight. For the events mentioned, no high-speed feature can be positively identified in images. Bentley *et al.* speculate that the X-ray line features are due to fast-moving material connected in some way with the fast-moving material seen as a visible ejection.

For two west-limb flares of 29 June the discrete line features appear to the short wavelength side of the Fe XXV resonance line at 1.85 A (BCS Channel 7) for only $\sim$20s. In each case, the time is coincident with a spike-like burst in hard X-rays as seen with the Hard X-ray Burst Spectrometer (HXRBS on SMM). Figure 6.3.5 shows a sequence of BCS channel 7 spectra around the time of the line feature during the 1041 UT event, together with a light-curve of the parent Fe XXV line and all channels (25-500 keV) of the HXRBS. For each event, the line features have at least a 3σ level of significance. The displacement of the features from the centroid of the Fe XXV line is a Doppler effect rather than a spacial displacement within the BCS field of view, since the latter would require flare activity $>$ 5 arcmin from the main flare site, which is not observed. Approach velocities of 290 km s^{-1} for the 1041 UT event and 370 km s^{-1} for the 1823 UT event are indicated. The features are not clearly resolved in the BCS Ca XIX detector which has only half the spectral resolution of channel 7.

The large X-ray velocities and the existence of visible-light ejecta in all three events suggest that hot material is driven out with the whitelight ejection. The line features are narrow, so their spacial extent is small (at least in the direction of dispersion, normally E-W), suggesting that the emitting volumes are small and blob-like rather than, e.g., sheet-like. Though Rust and Webb (1977) reported a fast-moving, soft-X-ray-emitting blob coincident with an H-alpha spray, in the case of an eruptive filament Rust and Hildner (1976) report a large volume of soft X-ray emitting material rising to become, perhaps, the CME itself. It is very suggestive that all three events discussed are spray associated.

The possibility that spray-associated flares give rise to Doppler-shifted discrete, X-ray line features has led Phillips to investigate spray-associated flares listed in *Solar Geophysical Data* (SGD, U.S. Dept. Commerce) for the SMM operational period. Excluding the events already discussed (SGD lists the 29 June events as surges rather than sprays), of the 93 sprays listed in SGD only 3 were compatible with the SMM pointing and showed Ca XIX brightening (the BCS's most sensitive indicator of flare activity). BCS Ca and Fe spectra were examined for each of the three flares. For the event of 1904 UT 9 September, a discrete line feature appears only in Ca XIX just 2 standard deviations above background. The other two flares show nothing. For periods when sprays were not reported, the SGD was consulted for metric Type II radio bursts occurrence. BCS spectra taken at the times of Type II-associated events were examined, but no clear examples of discrete line features were found.

The absence of identifiable discrete line features in the examined flares seems to arise from poor count statistics at the flare start. Typically, the surveyed events had maximum channel 1 counting rates below 500 s^{-1}, whereas the counting-rate for the three large flares with discrete line events was at least 2000 s^{-1}. The appearance of discrete lines seems to be a phenomenon distinct from the broadening and mild blue-shifting of the parent line, which occurs at the time of the impulsive hard X-ray burst; thus the short-lived discrete features should be most easily visible when the parent line broadening is least. The least broadening of

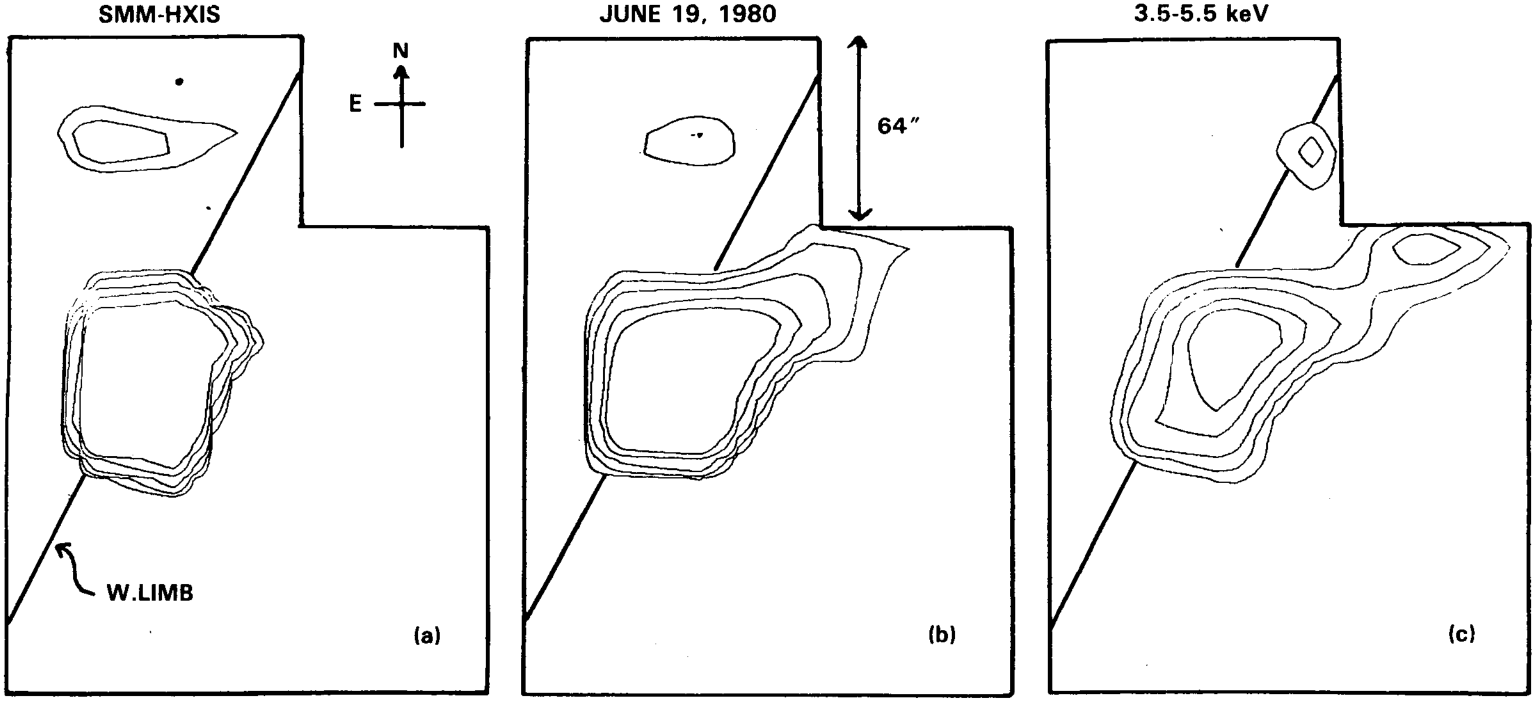

Figure 6.3.4 The X-ray transient seen during the second 29 June 1980 flare. Three HXIS 3.5 to 5.5 keV images are shown; (a) 10:42:50 UT, exposure 9.2s; (b) 10:46:00 UT, exposure 13.9s; and (c) 10:53:34 UT, exposure 20.5s. Intensity contours are plotted at 100, 50, 20, 10 and 5 counts/sec.

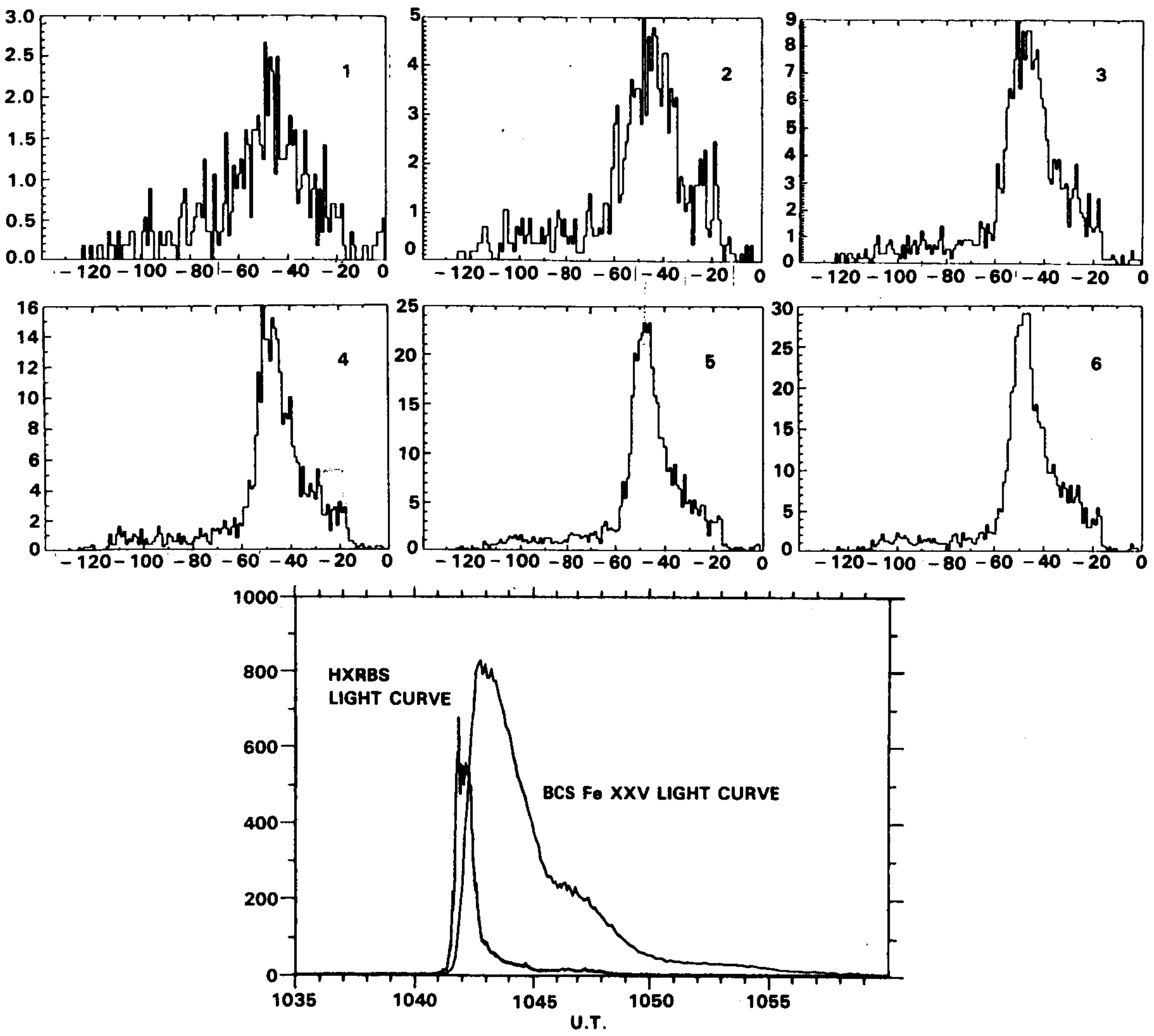

Figure 6.3.5 A. Six sequential BCS spectra of the Fe XXV resonance line ($1^1 - 2^1P$) during the rise of the soft X-ray event on 29 June 1980, at 1040 UT. Each spectrum covers the range 1.842 to 1.855A, and were obtained over an integration time of 5.63 at the following mean times: (1) 1041:45; (2) 1041:41; (3) 1041:57; (4) 1042:02; (5) 1042:08; (6) 1042:14. The vertical scale is in photon counts per wavelength interval per second. The line feature at bin 60 is reproducible in successive spectra starting at spectrum (2). (The structure at bins 20-30 is probably due to the blue-shifted Fe XXV line $1^1S_0 - 23^3P_2$.) B. Hard X-ray flux (HXRBS, all channels summed, energy range 25-200 keV) leading the Fe XXV line flux (BCS channel 7, bins 35-60) for the 1040 UT flare. (Vertical scales not absolute.) HXRBS light-curve from Dr. Allen Kiplinger, GSFC.

the parent lines occurs for flares on or near the limb, so a search for Doppler-shifted discrete line features of the type discussed here might be profitably directed at strong limb flares. It is hoped that the search will be renewed with the repaired SMM.

6.3.4 The 30 March 1980 Event

The event of 30 March 1980 has been selected for detailed description since an unusually complete set of observations exists. The active region (AR 2363) was at N25E25, well onto the disk, yet C/P observed a coronal transient resulting from activity within this region at about 1245 UT (assuming constant speed of the ejection from the surface to the heights observed later). Thus, the region is ideally suited for studying the initiation of the mass ejection. The activity of AR 2363 has been previously described (Lantos *et al.*, 1981; Lantos, 1984; Lantos and Kerdraon, 1984; and in Section 6.2.1.5). The complementary analysis done by Lantos and Waggett during the Workshop is summarized here.

The low coronal activity associated with the 30 March CME was varied and included a filament eruption, an intense metric noise storm, and an X-ray long duration event (LDE). At metric wavelengths, noise storms with durations of a few hours have been associated with filament eruptions (e.g., Webb and Kundu, 1978). Large amplitude X-ray LDEs are often associated with solar flares distinguished by their large physical sizes, low energy densities, and their association with whitelight coronal transients and centimetric gradual rise and fall bursts (e.g., Sheeley *et al.*, 1975; Pallavicini, Serio, and Vaiana, 1977). Like most others, the 30 March LDE appeared in soft X-rays as a system of large diffuse loops, brighter at the top and crossing a filament channel.

The structure of the low coronal region was imaged by the FCS; it is shown schematically in Figure 6.2.16. Two regions had been steady soft X-ray emitters, one associated with the magnetic inversion line to the northwest of the area labelled A and the other associated with the inversion line to the north of A, as well as various loop arcades. The footpoints of these arcades are denoted by H-alpha ribbons, also shown in the figure. Lantos *et al.* (1981) concluded that the two main loops are as in Figure 6.2.16., straddling a long filament which is due to erupt.

6.3.4.1 The Precursor Phase

The HXIS and BCS light curves indicate the presence of a small, soft X-ray burst between 1247 and 1250 UT of peak temperature and emission measure 6.4×10^6 K and 1.3×10^{54} m^{-3}. In Figure 6.2.16., two patches of emission are seen associated with the two areas previously mentioned. HXIS images reveal structure in both, and this — combined with their locations — implies that they are separate loop systems. However, the light curves for the two patches are so similar that there must be a connection between them, probably a large loop. This loop must be complex, since a simple link between the two regions would pass directly over the main sunspot group of the active region. This loop could either be passing to the north or south of the sunspots; as there is no evidence in the H-alpha photographs for any loops passing to the north, we will assume that the southern route is the more likely. Lying south of the sunspots implies that the loop will be close to those involved in the main X-ray LDE. This precursory activity could be an indicator of the actual initiation, the X-ray signature being due to loop-top merging to the south of the spot group.

6.3.4.2 The Main Event

The metric noise storm began after 1305 UT, about the time of the southern filament's disappearance. As discussed in Section 6.2.1.5, from about 1305 to 1330 UT, the motion of the noise storm is consistent with the motion of the poleward legs of the loops as they expand and carry the CME into the corona. Lantos and Kerdraon (1984) propose that as this scenario unfolded, the footpoints of some of the loops making up the transient were still attached to the chromosphere at least as late as 1330 UT. The motion discussed in Section 6.2.1.5 suggests a mass ejection onset at ~ 12:50 UT, assuming no acceleration. This implies a precursor/CME association of the type discussed by Harrison *et al.* (1985).

C/P observations of the CME were made at 1406 and 1426 UT, from which a relationship between the whitelight transient location and the rising loop structure is inferred and indicated in Figure 6.2.16.

Occurring contemporaneously with the preceding phases is the reconnection phase. During this phase, the main activity in the low corona is the reconnection of ruptured field lines; this powers the main X-ray event as well as the radio noise storm as soon as it is detached from the rising structure. The X-ray and radio intensity profiles are similar, peaking at about 1345 UT, although the noise storm (at B Figure 6.2.16) is several arcmin to the north of the X-ray emitting region, and they are associated with different legs of the ascending loop.

6.3.4.3 Summary

Summarizing the features of this event and the analysis:

1. Apparently a loop feature, between 1305 to 1426 UT, rose from a height of 100,000 km out to several solar radii.
2. This loop, which crossed over a filament involved in the ejection, became a CME.
3. The onset of the ejection was prior to the main X-ray event, perhaps associated with a precursor. The ejection appears to be the result of the merging of loop-tops.
4. The near-surface X-ray and radio signatures were due to reconnection.

6.4 MODELLING OF CORONAL MASS EJECTIONS AND POST-FLARE ARCHES

6.4.1 Introduction

For a comprehensive physical understanding of the CME phenomenon, theorists and modellers must address the following three broad questions and their ramifications: Under what circumstance and by what mechanism can a mass ejection be initiated, or triggered, in the low corona? How is the mass ejection accelerated and propelled dynamically through the corona? What are the manifestations of the mass ejection in interplanetary space? Though this chapter shows that observational data exist, sometimes in abundance, we are quite far from being able to provide answers to these questions in any complete form. Many interesting ideas have been pursued and debated. We refer the readers to recent review articles for surveys of these ideas (Anzer, 1980; Dryer, 1982; Rosner, Low and Holzer, 1984; Hundhausen *et al.*, 1984b). In this section, we report on some specific developments in the theory and modelling of mass ejections and other related coronal eruptions which were presented and discussed at the Workshop.

Existing spaceborne coronagraphs have fields of view covering 1.6 to 10 R_0. A mass ejection observed in these fields of view is already in a fully developed state of motion. Thus, mass ejections in this already-evolved dynamical state tended to dominate the interests of modellers and theorists in the early part of the Skylab era. Gradually, emphasis broadened to include the question of initiation. Data from the present generation of spaceborne coronagraphs cannot be expected to give direct information on the manner and circumstance of the initiation of mass ejections in the low corona. We emphasize two collections of indirect evidence relevant to the question of initiation. Some Skylab-era mass ejections were found to have been preceded, for an hour or more, by broad, faint outflows in the corona called transient forerunners (Jackson and Hildner, 1978; Jackson, 1981). These authors took this result to suggest that, for some mass ejections, the initiation involves a non-impulsive precursory phase. A contrasting view for the initiation of some SMM-era CMEs is presented in Section 6.3.2.2. In at least one case, a forerunner has been identified accompanying an SMM-era mass ejection (Gary *et al.*, 1984). The second group of indirect evidence comes from the statistical association of CMEs with the occurrence of other forms of eruptions in their space-time vicinity. The Skylab CMEs had a significant association with flares and an even more significant association with prominence eruptions (Munro *et al.*, 1979). This pattern of association has been found to be basically unchanged at the current solar maximum (Sawyer *et al.*, 1985; but see also Webb and Hundhausen, 1985). Unlike the SMM era, the prominences that erupted in association with the Skylab CMEs were found to tend to have north-south orientations before their eruptions (Trottet and MacQueen, 1980).

Recently, direct observation of the low corona in whitelight became possible with the operation of HAO's K-coronameter at Mauna Loa, which has an annular field of view of 1.2 to 2.2 R_0 (Fisher *et al.*, 1981). Observations of mass ejections in their early dynamical development show distinctly different kinematics for flare- and prominence-associated mass ejections in the low corona (MacQueen and Fisher, 1983). The former tend to be already at high speeds (>300 km s^{-1}), when first observed, and have little discernible acceleration thereafter, whereas the latter tend to be at low speeds (<300 km s^{-1}) when first observed and often show detectable accelerations. Above 2 R_0 in the fields of view of spaceborne coronagraphs, mass ejections tend to move at approximately constant speeds, making their acceleration profiles nearly indistinguishable. These observations suggest that different mass ejections may be subject to different types of acceleration process in the low corona.

The good association between some mass ejections and flares suggests that the initiation processes of mass ejections and of flares may be coupled. Numerical MHD models developed thus far have taken as a starting point that the flare energy initiates and drives the mass ejection by way of impulsively generated nonlinear MHD waves (e.g., Dryer, 1982). It has also been suggested that mass ejections may be magnetically driven as a consequence of the magnetic reconnection postulated for the liberation of the flare energy (Pneuman, 1980). On the other hand, there are CMEs not associated with flares which appear without any impulsive signature in the chromosphere. For these ejections, it has been suggested that they result from the transition of a highly stressed, slowly evolving structure into a state of non-equilibrium (Low, 1981).

Over the length and time scales of concern, ideal magnetohydrodynamics (MHD) provides an appropriate, lowest order description for CMEs. The contention between different theoretical ideas suggested for the initiation and propulsion of mass ejections has led, among other things, to the recognition that we need to develop our basic intuition and understanding of the magnetohydrodynamic medium in the presence of gravity (e.g., Rosner, Low, and Holzer, 1984). We seem to be at a stage where the questions posed by observation on mass-ejection initiation and dynamics are sufficiently focused to warrant intensifying theoretical efforts to resolve basic theoretical issues and to develop the next generation of models. The question concerning the interplanetary manifestations of CMEs is relatively new. The observational picture is, at the present, incomplete, and the theoretical ideas on this question are much less developed.

With the above overview, we present the following five projects developed at the Workshop. In Sections 6.4.2 and 6.4.3, we report on two projects aimed at understanding basic MHD. In Section 6.4.2, Hildner and Wu present a parametric study of an ideal MHD numerical model to investigate the range of physical characteristics exhibited by the impulsively perturbed atmosphere. In Section 6.4.3, Low reports his recent discovery of analytic, self-similar solutions to the time-dependent equations of MHD, which opens up the possibility of building analytic models and testing numerical MHD codes. The projects in Sections 6.4.4, 6.4.5, and 6.4.6 are concerned with various aspects of mass-ejection initiation. In Section 6.4.4, Svestka interprets the formation of post-flare coronal arches observed with the HXIS instrument on the SMM satellite. In Svestka's study, the flares are studied not only for their own sakes, but also for their possible relationships with the initiation of associated mass ejections observed with NRL's SOLWIND coronagraph. In Section 6.4.5, Poletto and Kopp treat a magnetic reconnection model to refine the method of estimating the energy extractable from the magnetic fields in a two-ribbon flare. Finally, in Section 6.4.6, Low demonstrates, theoretically, the linear MHD-stability of coronal structures.

6.4.2 Parametric Study with a Numerical MHD Model

Numerical models have the technical advantage that within the numerical code developed for a particular model, one can freely prescribe the details of the initial and boundary conditions. Numerical modelling has so far concentrated on pulse-initiated disturbances in an ambient atmosphere (Dryer, 1982). Despite the existence of numerical modelling studies with a rich diversity of initial conditions and initial perturbing pulse characteristics, till now there has not been a systematic attempt to learn how the simulated coronal response is affected by varying the initial conditions (e.g., the initial magnetic field strength). In this section, we present the results of a systematic study of this type. We used a single numerical model (Wu *et al.*, 1983) incorporating ideal MHD equations to calculate the response of the solar atmosphere to a standard pressure-pulse perturbation, introducing the pulse into a different member of a family of magnetic configurations for each calculation. The members of the family of magnetic configurations differ in their multipole number and in their base strength. The standard pressure pulse was introduced at one or the other of two places in each initial configuration and strength, as explained below. The results of the 12 calculations allow us to gauge how initial field strength at the coronal base, overall field configuration — and the fall-off of field strength with height, and the location of the pulse affect the response of the corona.

An isothermal ($T = 2 \times 10^6$ K) hydrostatic corona of base density $n_e = 10^{8.5}$ cm^{-3} is permeated by a potential field. Because the calculation is two-dimensional and axisymmetric, there is no variation of any parameter in heliocentric longitude.

Three initial field configurations are considered: a dipole (180 deg symmetry), a quadrupole (90 deg symmetry), and a hexapole (60 deg symmetry), as shown in Figure 6.4.1. Of course, the magnetic field strength decreases more rapidly with height for the higher multipole fields. Coronal mass ejections often arise in active regions, only rarely subtending as much as 60 deg of heliographic angle; even the hexapole configuration may span too large an angle to be realistic, but we are interested in discerning trends in coronal response as we examine magnetic structures of various scales. Since the gas pressure in the initial, hydrostatic corona varies only with height, the initial plasma beta, the ratio of gas to magnetic pressure, varies with latitude and height. In our calculations, we use two magnetic field strengths for each configuration; the pre-perturbation beta at the site of the perturbing pulse is either 0.1 or 1.0 for a perturbation placed on the open-field symmetry axis. These field strengths imply beta is 0.45 for 4.5 for a perturbation on the closed-field symmetry axis.

The side boundaries of the computational domain are defined by radial rays along symmetry axes of the initial magnetic configuration; no fluid flows through these boundaries, but the pressure and density evolve in response to the perturbation. Though the computational domain covers only one half of one lobe in each magnetic configuration, we take the boundary conditions as periodic, with a perturbing pulse identical to the one in the calculational domain being placed simi-

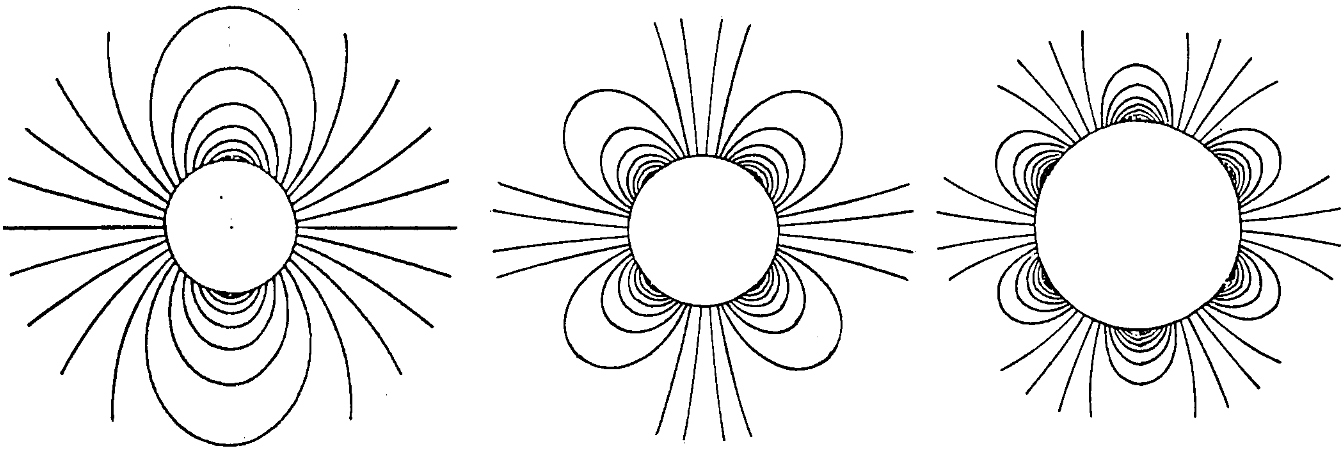

Figure 6.4.1 Meridional cut through the magnetic field configurations for parametric study. Each configuration employed in the study has rotational symmetry about an axis in the plane of the paper; the orientation of the symmetry axis is chosen to make the equatorial magnetic field either open or closed. (a) Dipole configuration. (b) Quadrupole. (c) Hexapole.

larly in each lobe of the magnetic field around the sun. The top and bottom boundaries are transparent to fluid flow. After the perturbation is established, the temperature and density are maintained constant on the lower boundary, and the compatibility relations determine the flow; temperature and density are allowed to evolve on the upper boundary. The lower boundary is at 1.0 R_0, and the upper boundary is at 5 R_0 for the dipole, 3.5 R_0 for the quadrupole, and 3.0 R_0 for the hexapole, respectively. Once the calculation begins, the magnetic field lines are not "tied" to a particular location nor required to have a specified orientation on any boundary.

To start each calculation, the gas pressure on three mesh points at the base of the mesh is raised, in a fast linear-ramp fashion, to a value five times the initial value. To achieve the pressure increase, the temperature is increased by 3 and the density by 1.67. At the perturbation site, the temperature and density values are maintained at their elevated values for the duration of each calculation. The perturbing pulse is placed at the base of the corona on a symmetry axis, either the open or the closed axis.

For this ideal MHD calculation, the governing equations are given by Wu *et al.* (1985) and Wang *et al.* (1982).

Comparisons among the 12 calculations are facilitated by Table 6.4.1, which emphasizes the outward flow of plasma engendered by the perturbing pulse. A stronger pressure pulse would be expected to increase the flow speed somewhat, especially in the open field configuration and for the

Table 6.4.1 Coronal Response for Various Magnetic Fields

Speed[b] (km s^{-1})
Density Enhancement[c]

STRENGTH

	β = 1.0[a]		β = 0.1[a]	
CONFIGURATION	**OPEN**	**CLOSED**	**OPEN**	**CLOSED**
DIPOLE				
t = 1200 s	340[b]	390	380	560
	6.5[c]	5.2	8.4	4.6
t = 2400 s	275[d]	360[d]	350	530
	12.0[d]	7.8[d]	17	9.8
QUADRUPOLE				
t = 1200 s	410	380	360	480
	5.6	4.9	7.1	2.5
t = 2400 s	265	310	300	250
	8.7	8.9	13	4.4
HEXAPOLE				
t = 1200 s	220[e]	240[e]	310	230
	4.4[e]	3.5[e]	5.8	2.1
t = 2400 s	240[f]	280[f]	240	180
	6.8[f]	8.0[f]	9.5	3.3

Notes:
a. The ratio of gas to magnetic pressure at the base of the open field. Pre-perturbation beta is ~4.5 times greater at the base of the closed-field symmetry axis.
b. The estimated, on-axis height of the $n_e(r,t)=2n_e(r,o)$ contour, divided by the elapsed time; see text.
c. The maximum density enhancement attained anywhere in the computational domain at the noted time.
d. At t = 2800 s
e. At t = 1050 s
f. At t = 2250 s

weak magnetic field case (β = 1.0). Other tables could be drawn to contrast other aspects of the way the corona responds to the standard pulse, of course. In Table 6.4.1, at two times for each configuration, we have listed an estimate of the on-axis speed of the contour which represents a 100 percent local density enhancement and the maximum relative density enhancement.

Perusal of the table allows us to state a number of comparative results which are verified by close examination of the more detailed plots of the coronal evolution simulated by the calculations.

1. In the weak-field cases, those in which beta = 1.0 on the open-field symmetry axis at the lower boundary, the outward speed of strong density enhancement is nearly the same for the open- and closed-field trials of a particular configuration. Similarly, the magnitude of the maximum density enhancement differs little between trials when the disturbance is placed in the open or closed portion of a configuration. Even between configurations the variation is fairly small.
2. In sharp contrast to result 1, in the strong-field case, those in which beta = 0.1 (0.45) at the base of the open (closed) field, there is a considerable difference between the open- and closed-field trials of each configuration, especially in the magnitude of the maximum density enhancement which occurs.
3. The chosen excess density contour rises at speeds within the range of observed coronal mass ejections speeds.
4. The ascent of the contour appears to be slowing with time, generally. This contrasts sharply with the observed behavior of coronal mass ejections in the lower corona; MacQueen and Fisher (1983) report that CMEs typically exhibit steady or increasing speeds in this height range.

From these results we may draw the following interpretations and conclusions:

1. The effect of the magnetic field is small when beta = 1.0 at the base of the open-field corona. This is understandable in light of the fact that for our assumed initial field (and for any non-pathological, realistic solar magnetic field) beta increases rapidly with height; for beta = 1.0 (4.5) at the base of the open (closed) corona, therefore, the gas pressure dominates the magnetic pressure everywhere in the initial configuration.
2. When the magnetic field is sufficiently strong, the character of the flow is significantly different for the perturbation introduced on the open-field axis of the configuration than it is for the perturbation introduced on the closed-field axis. The introduction of the perturbation sets up a pressure gradient in its vicinity. In response, the plasma can flow outward (along the field lines) if the site of the high-pressure perturbation is on the open axis of the magnetic field configuration. In these cases, the outflow from the perturbation site adds mass to the computational domain, and dense material rising from below into the more tenuous, ambient upper corona causes ever-increasing, strong, local density enhancements. By contrast, outward fluid flow — which must produce deformation of the overlying magnetic field — is strongly retarded in the closed-field cases. Because fluid flows away from the perturbation less readily, less mass is added to the computational domain per unit of time, and there is a much smaller maximum density enhancement than in the open-field cases.

Although in the calculation waves propagate away from the site of the perturbation, their density contrast ($\Delta n_e/n_e <$ one percent) is insufficient for them to be identified with observed CMEs, whose much higher brightness contrast with the background ($(B-B_0)/B_0 > 0.6$ according to Sime, MacQueen and Hundhausen (1984)) implies a higher density contrast. The shape of the wave front is affected by the choice of the site of the perturbation, since MHD fast waves propagate more rapidly across than along field lines.

In summary, it is difficult to see how a reasonable pressure pulse at the bottom of a potential magnetic field configuration can give rise to rapid outflow of large amounts of mass, as seen in CMEs. In the calculations reported here, for the more realistic low-beta cases, a significant fraction of the energy given to the fluid by the excess gradient of pressure in the vicinity of the perturbation site is absorbed in the deformation of the magnetic field, initially in its lowest-energy state. Thus, the field is retarding, rather than driving the mass flow. Nevertheless, wave motion propagates significant energy away from the perturbation site even though the bulk flow is small; this wave motion alters local plasma conditions as it goes.

It appears that an appropriate next step in attempts to simulate CMEs via numerical modelling is to start from an equilibrium configuration in which the magnetic field is stressed, i.e., contains stored energy, so that magnetic energy can be transferred to the fluid once the perturbed flow begins (Low, 1982). Whether this initial state is best simulated as a magnetohydrodynamic steady state (more realistic) or as a magnetohydrostatic one (easier to calculate) is not yet clear.

6.4.3 Self-Similar MHD Modelling of Mass Ejections

In reality, mass ejections are three-dimensional objects. Since time-dependent MHD flows with variations in three-dimensional space pose exceedingly difficult mathematical problems, modellers have so far concentrated on two-dimensional systems, in particular, the axisymmetric atmosphere. It is generally accepted that a spacially one-dimensional system is of little use in the study of mass ejections, because many of the interesting, anisotropic magnetic effects in the MHD medium take trivial forms in such a system. Fortunately, a two-dimensional system is adequate to capture the essence of these effects; two-dimensional, time-dependent MHD flows are very complicated, and numerical methods provide the only practical means of building models. Still, a strictly numerical approach is not often useful. There is a need to build up our intuition and knowledge of the behavior of the highly nonlinear MHD system to enable ourselves to question and to interpret numerical results. Analytic solutions, whenever they can be found, serve this need well. We are fortunate that analytic, time-dependent solutions to the MHD equations exist (Low, 1982; 1984a). In the following, we describe briefly what these solutions are and point out some of their physical implications for the mass ejection phenomenon.

As demonstrated in Low (1984a), the ideal MHD equations admit time-dependent solutions describing a radial global velocity field of the form

$$\underline{v} = \frac{r}{\Phi}\frac{d\Phi}{dt}\,\hat{r} \qquad (6.4.1)$$

where Φ is a strict function of time satisfying

$$\left(\frac{d\Phi}{dt}\right)^2 = \eta - \frac{2\alpha}{\Phi} \qquad (6.4.2)$$

with η and α being arbitrary constants. In such a velocity field, the plasma and magnetic field evolve in a self-similar manner as described by

$$p(\underline{r},t) = \Phi^{-4}\, P(\zeta,\theta,\phi), \qquad (6.4.3)$$

$$\varrho(\underline{r},t) = \Phi^{-3}\, D(\zeta,\theta,\phi), \qquad (6.4.4)$$

$$\underline{B}(\underline{r},t) = \Phi^{-2}\, \underline{H}(\zeta,\theta,\phi), \qquad (6.4.5)$$

where the similarity variable

$$\zeta = \frac{r}{\Phi} \qquad (6.4.6)$$

has been introduced. In fact, if Equations (6.4.3)-(6.4.6) are substituted into the MHD equations, the conservation laws for mass, magnetic flux, and entropy are trivially satisfied for all functional forms of P, D, and H, provided we set $\gamma = 4/3$. Explicit time-dependence can then be transformed away from the momentum equation to give rise to

$$\alpha\,\zeta\,D\hat{r} = \frac{1}{4\pi}(\underline{\nabla^*} \times \underline{H}) \times \underline{H} - \underline{\nabla P} - \frac{DGM_\odot}{\zeta^2}\, r, \qquad (6.4.7)$$

where ∇^* is the usual operator ∇, but with r replaced by ζ. In this final procedure, we have transformed the time-dependent MHD problem to a "static" problem cast in the (ζ,θ,ϕ) space. To construct a solution, we solve the pseudo-magnetostatic problem posed by Equation (6.4.7), seeking equilibrium states in which the Lorentz force balances a pressure gradient and a body force made up of Newtonian gravity and an inertial force arising from the non-Galilean similarity transformation. To every solution so constructed and a solution Φ of Equation (6.4.2), we can generate a time-dependent MHD solution by transforming from the (ζ,θ,ϕ) space back to real space-time. It is important to note that this formulation does not require the physical system to be two-dimensional. Both axisymmetric and fully three-dimensional solutions are admissible. Axisymmetric solutions are the ones that received immediate attention for reasons of tractability. However, we should bear in mind that this formulation has opened up the feasibility of building three-dimensional solutions (Low, Hundhausen, and Hu, 1985).

Figure 6.4.2 displays the time-development of an axisymmetic solution which simulates a mass ejection in the form of an expanding loop structure. This type of mass ejection is commonly observed (Munro *et al.*, 1979). The mathematical construction of the solution displayed in Figure 6.4.2 is given in Low (1984a). In the figure, we are looking at a global outflow carrying an axisymmetric magnetic field. This outflow plows into an ambient atmosphere having no magnetic field. A spherical contact surface, marked $r = R_c$, forms between the two fluids and drives a strong gasdynamic shock propagating into the ambient atmosphere. The top panel shows the magnetic field lines projected onto the meridional plane at three successive instants of time. In this particular example, there is a ϕ-component of the magnetic field. Thus, the set of nested, closed loops of field-line projection correspond to a twisted toroidal magnetic flux rope in three-dimensional space.

The free parameters of the solution and the density profile of the ambient atmosphere have been chosen to produce the following dynamical behaviors. At some initial moment, say $t = t_0$, the outflow has been established with $R_c = 2 \times 10^{11}$ cm and the shock created right on $r = R_c$. The ambient atmosphere is such that the shock immediately separates and propagates with a speed which increases as the 1/7th power of the shock radius. At the same time, the contact surface moves outward at a constant speed of 540 km s^{-1}. All this is achieved with an ambient atmosphere whose density falls with radius approximately like $r^{-26/7}$, a profile which is steeper than r^{-2} drop for a solar wind with a constant speed. Thus, this ambient density profile would correspond to a region of accelerating solar wind in the corona. The three instants of time indicated in Figure 6.4.2 are reckoned from the initial moment $t = t_0$.

Consider the second panel of Figure 6.4.2 showing the time development of density in the outflow. We find low den-

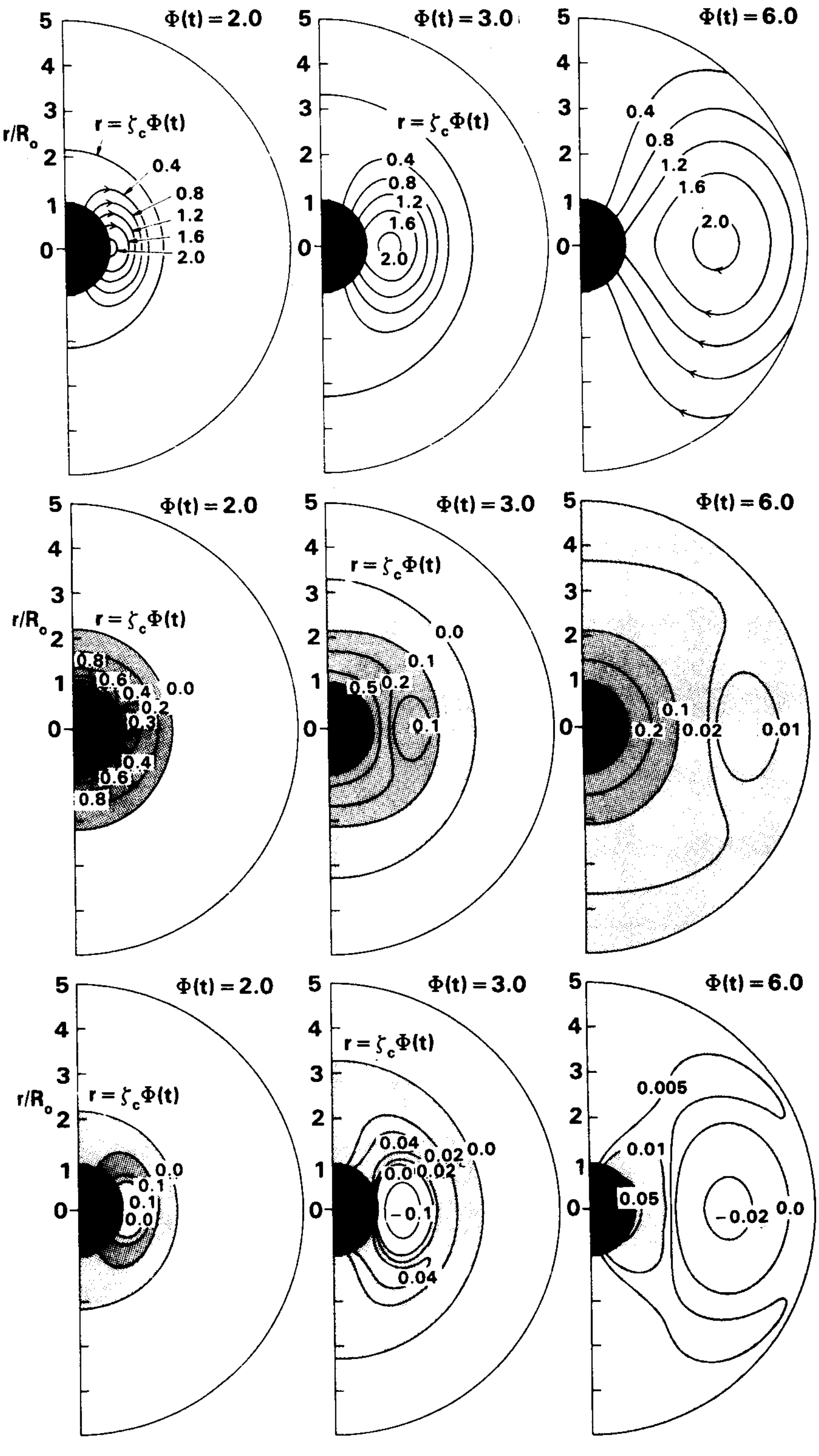

Figure 6.4.2 A particular axisymmetric MHD solution simulating a loop-like mass ejection. The top panel shows magnetic field lines projected on the meridional plane at three instants of time. The boundary $r = \zeta_c \Phi$ is a contact surface. The lower two panels show the distributions, at the same respective instants of time, of the density ρ and density excess $\Delta\rho$, as described in the text.

sity in the equatorial region, flanked by higher densities at higher latitudes. Let us define $\Delta\varrho$ to be the excess density above the spherically-symmetric reference density given by the run of the initial density along the polar axis. The departure from spherical symmetry, $\Delta\varrho$, is analogous to the result of subtracting a standard pre-event photograph from a coronagraph photograph of a mass ejection, a procedure commonly used in data analysis. The time-development of $\Delta\varrho$ is shown in the third panel in Figure 6.4.2. We identify a density enhancement ($\Delta\varrho > 0$) in the form of a loop structure in the r, θ plane, enclosing a cavity of density depletion ($\Delta\varrho > 0$). In the time development, the top of the "loop" fades away, leaving the appearance of a pair of radial "legs". The legs tend towards a fixed angular displacement between them, a phenomenon commonly observed for loop-like mass ejections. Eventually, the density depletion cavity rises. and a density enhancement takes its place. This and other illustrative MHD solutions are constructed and analyzed in Low (1984a).

Self-similar MHD solutions are being generated both for comparison with specific mass ejection observations and for studying their basic physics. Since these solutions can be constructed analytically, they also provide an opportunity to test the accuracy of existing numerical codes. In the following, we point out two interesting physical implications which have emerged from the study of self-similar MHD. The form of radial velocity given by Equation 6.4.1 is specialized. Realistic mass ejections exhibit small motions in the θ-direction (e.g., Hildner, 1977). The radial velocity field of Equation (6.4.1) must be regarded as a lowest-order description. In fact, self-similar solutions often are lowest-order descriptions of general, non-self-similar solutions in regions of space-time which are not sensitive to the influence of boundary and initial conditions (Barenblatt and Zel'dovich, 1972). It seems worthwhile to look quantitatively for self-similar behaviors in observed mass ejections; see the study by Illing (1984).

The time development of self-similar flows is dictated by the function fixed through Equation (6.4.2) by prescribing the constants η and α. Only positive values of η are admissible for unbounded expansion flows. For these flows the sign of α dictates an accelerating ($\alpha > 0$) or decelerating ($\alpha < 0$) flow. In *all* cases, the flow rapidly becomes inertial so that each plasma parcel sees no net force and cruises at constant speed. There is a spacially and temporally varying (Eulerian) velocity field, since different plasma parcels may move with different inertial speeds. The value of α then controls the magnitude of the terminal speeds of the cruising plasma parcels. The value of α is not bounded below so that, in principle, the expansion flow can have extremely low inertial speeds. These properties allow us to understand for the first time why most mass ejections are observed to have constant speeds above 2 R_0 and why their constant speeds can cover a broad range, from below 100 km s^{-1} to about 1000 km s^{-1} (Gosling *et al.*, 1976; Rust, Hildner, *et al.*, 1980; MacQueen, 1980). It appears that such inertial states are preferred asymptotic states, irrespective of initial conditions. In the inertial states, Lorentz forces and pressure gradients act to balance gravity so that ballistic deceleration of mass ejections is seldom observed. Notice that the construction of a self-similar MHD solution involves solving Equation (6.4.7) the pseudo-magnetostatic problem and Equation (6.4.5) the time-evolution problem, as two independent steps. Thus, an infinite variety of plasma and magnetic structures, generated by Equation (6.4.7), can evolve from the same velocity field given by Equation (6.4.5). This suggests that the dominant effect in a mass ejection may be a global outflow due to gravitational instability (Low, 1984a). In such an outflow, an entire coronal structure expands and is carried outward. That the corona is gravitationally unstable is not new. We know from the study of solar wind that efficient heating and thermal conduction, in the absence of adequate interstellar pressure to confine the corona, are natural causes for an expanding corona (Parker, 1963). Magnetic fields provide the only means to halt this expansion for localized low coronal regions through the tension force of field lines anchored in the dense photosphere. Various effects, for example the occurrence of a flare, can cause the magnetic tension force to be inadequate to hold down a coronal structure. The coronal structure then expands outward. In such a picture of the mass ejection, density-enhanced and density-depleted features are different parts of a single expanding structure and can have a different dynamical relationship than might be postulated for a compressional wave and its trailing rarefaction wave.

6.4.4 Post-Flare Coronal Arches Imaged in >3.5 keV X-rays

The Hard X-ray Imaging Spectrometer aboard the SMM (van Beek *et al.*, 1980) detected gigantic post-flare arches in the solar corona that are seen in X-rays above 3.5 keV and extend along the $B_{\|} = 0$ line to altitudes between 10^5 km and 2×10^5 km. So far we have detected a number of arches of this kind, of which four have been studied in detail: on 22 May 1980, following the flare of 2055 UT on 21 May; on 6 November 1980, following flares at 0329 and 1444 UT; and on 7 November 1980, following the flare at 0444 UT. The relationship between these arches and the similarly-sized loops which brighten just prior to flares discussed in Sections 6.3.3.1 and 6.3.4 for two events, is not clear. In this section, the post-flare behavior of large arches is considered.

The basic characteristics of the arches can be summarized as follows:

(a) All flares that produced or revived a coronal arch were flares associated with a Type IV radio burst (mostly accompanied by Type II). Flares of this kind have the form of two bright ribbons in H-alpha at footpoints of a growing system of loops (e.g., Svestka, 1976). The existence of bright ribbons and/or growing loops has been confirmed for all flares that produced the arches and for which H-alpha pictures were available. Other flares in the same active regions, even of H-alpha importance 2B in one case (6 November, 1726 UT), did not produce or revive the arch.

As the radio Type IV burst decays, the continuum becomes noisy, and the burst changes into a long-lasting type I noise storm. Thus, the arch can be considered to be an X-ray image of the lowest part of the (stationary) Type IV burst in its early phase, and of a Type I noise storm in the later phase of its development (examples in Svestka, 1983).

(b) The arch observed after the flare of 21 May 1980 (Svestka *et al.*, 1982a) was stationary, its brightness maximum staying at a constant projected distance of 10^5 km from the $B_{\|} = 0$ line (corresponding to an altitude of $\sim 1.5 \times 10^5$ km). There was no other two-ribbon flare in that region: the arch was an isolated feature formed during the flare, and it ceased to be visible 11 hours later.

(c) In contrast to that, in the three consecutive arches on 6 and 7 November 1980, shown in Figure 6.4.3 (Svestka, 1984), brightness maxima moved upwards, eventually disappearing from HXIS field of view (Figure 6.4.4). Arches 2 and 3 were clearly revivals of the preceding arch following new two-ribbon flares in the active region (cf., the shaded triangles in Figure 6.4.3). However, there was another major two-ribbon flare at 1341 UT on November 5. We surmise that this flare produced the first arch of the series (while HXIS looked at another region) so that even arch 1 in Figure 6.4.3 was probably a revival. This supposition is supported by the striking homology of arches 1 and 2 in Figure 6.4.4 (arch 3 was significantly weaker).

(d) A detailed analysis of HXIS images reveals that there were two velocity components in the arches (Figure 6.4.5): a slow one, with 8-12 km s^{-1} in projection on the plane of sky, and a fast one, with 35 km s^{-1} in projection. The slower speed is related to the rise of the brightness maxima, whereas the source of the fast component remains unknown.

Two other kinds of motion are also present: the 1-10 km s^{-1} growth of post-flare loops below the arch, and a possible coronal transient (no observations available) with a speed of several hundred km s^{-1}. Thus, the post-flare velocity pattern in the corona is extremely complex.

(e) In arch 2, which HXIS observed from its beginning, temperature ($\sim 14 \times 10^6$ K) peaked $\sim$65 minutes, X-ray counts peaked about 2 hours, and emission measure maximized $\sim$3.5 hours after the onset of the arch revival. Thus, the coronal arch looks like a magnified flare, with scales both in time and size increased by an order of magnitude.

(f) At the altitude of 10^5 km (mean of six integrated HXIS pixels) the maximum electron density was $n_e \sim 2.5 \times 10^9$ cm^{-3} and energy density $E \simeq 11.2$ erg cm^{-3}. This leads to a total energy content of the arch of 1.2×10^{31} erg at the time of observed maximum energy density and to a total mass of 4.4×10^{15} g.

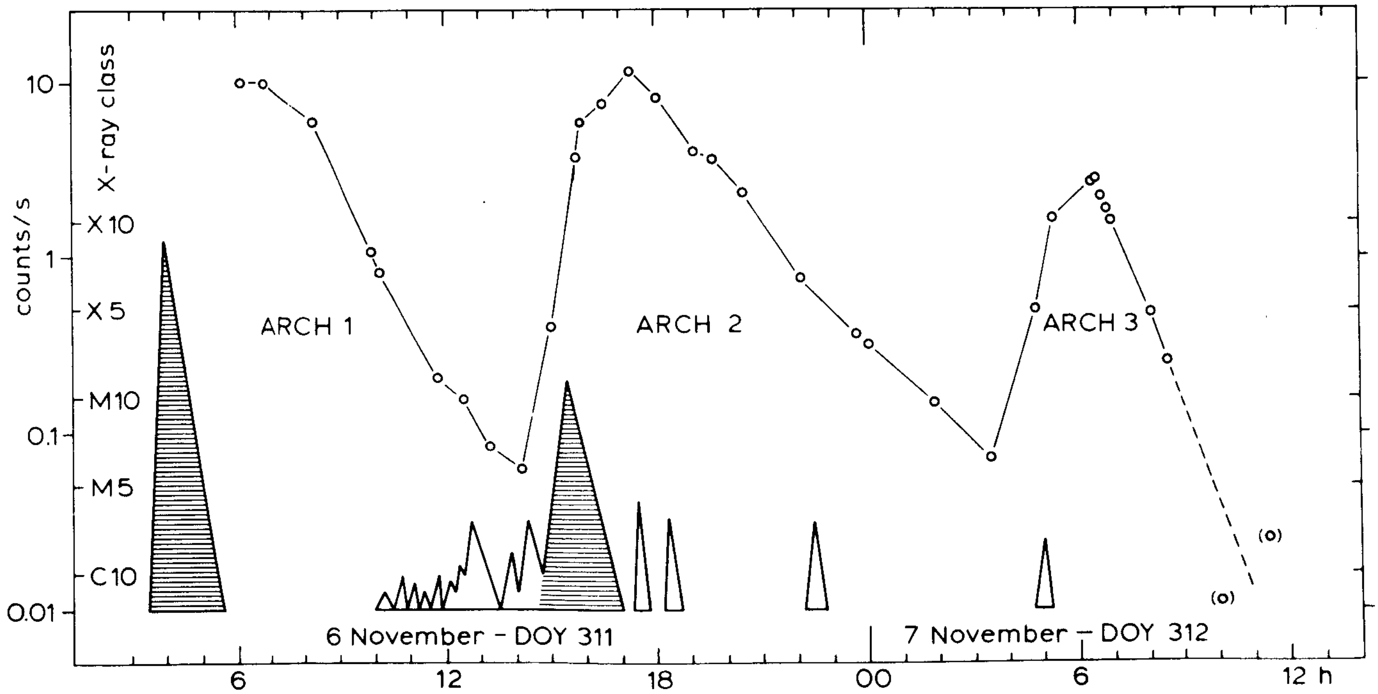

Figure 6.4.3 Time variations of the brightness of the coronal arches on 6 and 7 November 1980: maximum counts per second in one pixel of HXIS coarse field of view (32″ × 32″) in the energy range from 3.5 to 5.5 keV. The triangles below indicate 1-8 A X-ray variations in the active regions below the arch (GOES-2 data, scale C6-X10). The parent flares of the arches are hatched.

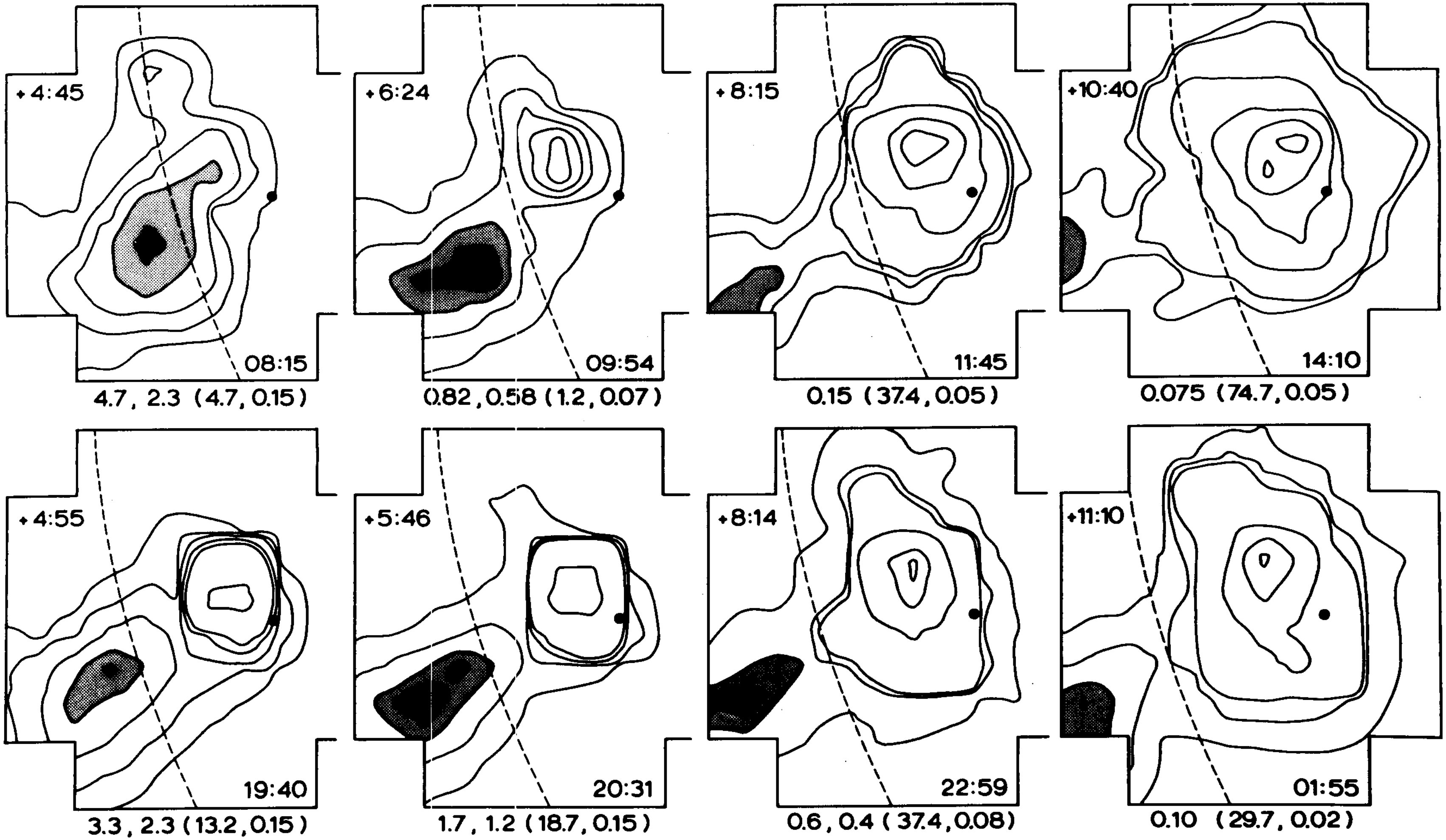

Figure 6.4.4 3.5-5.5 keV images of the arches 1 and 2 of Figure 6.4.3. The dashed line is the solar limb; a black dot marks the big spot in the parent active region. In each image the lower-right number is the time of imaging, while the upper-left number is the time elapsed from the onset of the parent flare. The numbers below each image are counts/second per pixel of HXIS coarse field of view corresponding to the brightest (shaded) contour(s) in the arch and (in brackets) the maximum and minimum contours in the image.

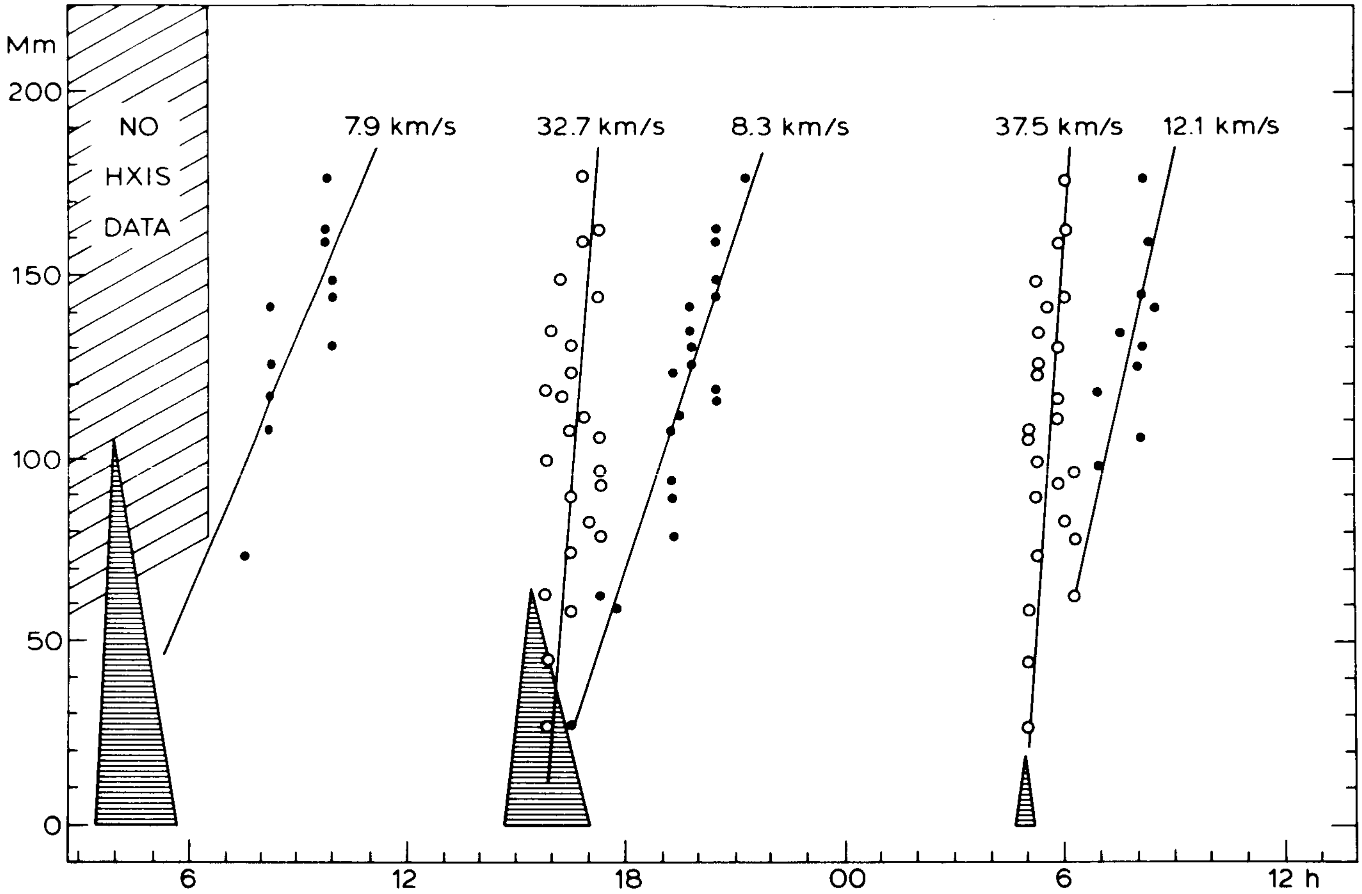

Figure 6.4.5 Velocities on 6 and 7 November 1980, deduced from a set of 25 pixels of HXIS coarse field of view. Each point (or circle) shows the time at which the arch brightness reached maximum in a HXIS pixel located at a given distance (in Mm) from the active region. The triangles (parent flares in X-rays) have been taken from Figure 6.4.3.

The arch must cool through radiation, with conduction cooling inhibited. If uninhibited conduction cooling occurred for the duration of the arch, then the arch's total energy content would exceed that of the parent flare below it.

(g) Even at the altitude of 10^5 km, the temperature began to rise at the very onset of the flare that revived the arch. This is evidence that the whole extent of the pre-existing arch was fed with energy from the beginning of its revival. Thus, the revival apparently implies a refilling of the pre-existing arch with heated plasma.

In addition to the revived arch, the images in Figure 6.4.4 and the velocity patterns in Figure 6.4.5 reveal that a new feature was formed in the low corona and propagated upwards. An analysis of the emission measure and temperature reveals that the travelling disturbance was predominantly a temperature enhancement.

(h) Maximum temperature in the arch is always observed slightly above the site of the maximum brightness and rises with a similar speed. This indicates a decrease in density with increasing altitude.

In temperature maps, the rising temperature wave can be studied even in the early phase of the arch development, when the image of the arch cannot be easily separated from the image of the nearby flare. For arch 2 on 6 November we get $v \simeq 7.4$ km s^{-1} as the speed of the thermal wave during the period 40 to 80 min after the flare's impulsive peak (compared to ~ 8.3 km s^{-1} for the later period shown in Figure 6.4.5). In a similar way, for the same period of time after the flare, we find a thermal wave with $v \simeq 6.3$ km s^{-1} for the flare of 4 June 1980. HXIS looked at this flare for one orbit only; still, the existence of a temperature wave moving upwards with a speed similar to the 6 November event indicates strongly that this flare was also the source of a post-flare arch. This offers an attractive possibility to infer the existence of more arches from HXIS data, even when the arch itself was not imaged as HXIS looked elsewhere on the Sun after the flare was over.

Characteristic a. shows clearly that the arch must be a natural component of a two-ribbon flare, formed or revived during the flare formation; at the same time as flare loops are formed below (sometimes for hours after the flare onset), the arch originates in the corona above them. This can be explained well by the Kopp and Pneuman (1976) model of the post-flare loop formation in Sturrock and Smith's (1968) configuration, through sequential reconnection of distended field lines. Each field-line reconnection produces a flare loop below and an elliptical closed field formation above. If the reconnecting field is sheared, the upper formations become interconnected and form a coiled structure over the $B_{\parallel} = 0$ line (Anzer and Pneuman, 1982; Svestka *et al.*, 1982a; Pneuman, 1983). There is a long sequence of such reconnecting coils that merge, mix, partly reconnect, and eventually give rise to a very complex magnetic field above the flare site; this field confines plasma, excited in the reconnection process, which is seen in X-rays as the post-flare arch. The magnetic field complexity also explains why the conductive cooling is inhibited (characteristic (f) noted above).

If the arch still exists when a new flare of the same type occurs below it, the arch field structure becomes an obstacle for the newly distending field lines. The loop distention at the onset of the flare is stopped, and at least some loops reconnect with the coils in the arch (Svestka, 1984). Thus, particles accelerated in the reconnection process and heated plasma begin to have free access into the pre-existing arch, raising its temperature: the arch revival begins. However, the field lines that reconnect first with the old arch are the outer field lines (the highest ones), most distant from the $B_{\parallel} = 0$ line. Only later does reconnection of the lower loops occur; and only then can the Kopp and Pneuman mechanism begin to work, since the lowest lines reconnect back first. This really seems to be confirmed in arch 2 on 6 November, where no loop system was seen in the flare during the first 33 - 40 minutes of its development, though temperature in the arch was increasing (Svestka, 1984). A new arch begins to be formed, perhaps, as the upper product of the loop-reconnection process, *after* the first post-flare loop appeared and the velocity fields found in Figure 6.4.5 may reflect this formation.

A difficult problem to be solved is the relation of these stationary or semi-stationary coronal arches to whitelight coronal transients and coronal mass ejections (CMEs). On 21 May 1980, the preflare filament was greatly activated, but it did not rise and never fully disappeared. Instead, a powerful outburst of dark material was seen to leak southwards from its eastern end. The whitelight coronagraph of NRL observed a CME in the extension of this dark outburst, but it was regarded as an atypical event that could not be included in any well-known category of CMEs (McCabe, Howard, and Svestka, 1985). On the other dates when HXIS recorded the arches, outer coronal images were not available. However, the SOLWIND coronagraph imaged a typical post-CME coronal structure above the eastern limb a few hours after the flare that had produced arch 1 on 6 November (Howard, 1984). This flare produced one of the most extensive Type IV bursts ever seen at Culgoora, as well as a strong Type II burst (Stewart, 1983). Thus, it looks very likely that a CME was associated with this flare. Apart from it, Type II bursts accompanying four out of the six parent flares producing arches signify shocks moving through the corona and are generally associated with CMEs. Thus, though the evidence is only circumstantial, both a post-flare arch and a CME can apparently originate in one and the same flare. There also seems to be radio evidence for associated CMEs: in many flares one can see both moving and stationary Type IV bursts. The moving burst may be related to a mass ejection, whereas the stationary burst is imaged as an arch in X-rays while gradually changing into a Type I noise storm lasting (like the X-ray arch) for hours.

The possible co-existence of mass ejections and semi-stationary post-flare arches is intriguing, particularly in light of the pre-flare brightening of large coronal loops in association with CMEs, as discussed in Section 6.3. We first thought that a transient may be ejected first and only then may an arch begin to form. However, if the revived arches are associated with transients, which seems to be indicated, this explanation cannot be true; the transient and the arch must involve different parts of the magnetic field above the active region.

6.4.5 Extension of the Reconnection Theory of Two-ribbon Solar Flares

The magnetic reconnection theory for the "decay phase" of two-ribbon flares, as developed originally by Kopp and Pneuman (1976) and subsequently by Pneuman (1980, 1982), Cargill and Priest (1982), and others, is generally regarded (Svestka *et al.*, 1980; Pallavicini and Vaiana, 1980) as providing a comprehensive and self-consistent description of the relationships between a wide variety of flare-associated phenomena — filament eruptions, H-alpha-ribbon brightenings and separations, hot (X-ray) and cool (H-alpha) flare-loop growth, and nonthermal particle generation and storage. Briefly, the theory hypothesizes that a two-ribbon flare is the visible manifestation of magnetic reconnection in the corona above the flare site, the stressed open-field structure within which this reconnection occurs having been created immediately beforehand by a filament activation/disruption and coronal transient. The excess magnetic energy of the distended field is released (rapidly at first and more gradually as the flare progresses) as reconnection allows a lower energy configuration containing closed magnetic loops to form. The field-annihilation process supplies the diverse energy requirements of the flare itself — enhanced optical emissions, dynamical mass motions, energetic particle releases, etc.

In the following, we extend the analytical basis for the reconnection model by developing a more general representation of the time-dependent magnetic configuration in the flare region than has heretofore been attempted. We will take explicit account of the fact, largely neglected in previous analyses, that the physical size of the hot flare loops generally increases as the flare progresses. The modified theory yields an analytic expression for the temporal variation of the average thermal energy density of the plasma on these closed loops. To compare with earlier studies, we apply the formalism developed here to the large two-ribbon flare of 29 July 1973, for which Skylab-era observations are available.

In previous studies the reconnecting field geometry was assumed to be dipolar near the Sun, but to undergo a smooth transition to a radial field at some radius $r_{1(t)}$ identified as the height of the neutral point. The dipole was located either at the solar center (Kopp and Pneuman, 1976) or at some specified distance beneath the solar surface (Pneuman, 1980, 1982). In neither case is the detailed analysis adequate: in the first case the global scale of the field is simply too large, whereas in the second an application of the axisymmetric dipole equations to a displaced (from sun center) dipole yields erroneous analytical results.

Large two-ribbon flares generally occur in mature or decaying active regions containing a magnetic neutral line oriented roughly in the east-west direction; but see Trottet and MacQueen (1980). For this reason, we choose a field representation which retains axial symmetry about the solar rotation axis ($\partial/\partial\phi = 0$), but which possesses a high degree of spacial structure in the latitudinal direction. Specifically, we seek a field which at any time t:

(a) is potential between the solar surface ($r = r_0$) and the neutral point level ($r = r_1$);
(b) extends radially outward beyond $r = r_1$; and
(c) has always the same magnetic flux distribution at the solar surface (i.e., an invariant $B_r(\theta)$ at $r = r_0$), since observations indicate that major field rearrangements do not occur at the photospheric level during large flares.

The field that satisfies conditions (a)-(c) is found by solving Laplace's equation $\nabla^2\Phi = 0$, where $B = \nabla\Phi$ in the region $(r_0,\ r_1)$, subject to the condition that $B = \frac{1}{r}\frac{d\Phi}{d\theta} = 0$ $r_1 = r_1$ ($B_\phi = 0$ automatically by the assumed symmetry). For $r > r_1$, $B_\theta = 0$, and B_r declines outward as r^{-2} from its value at $r = r_1$. It suffices to consider fields proportional to a single Legendre polynomial $P_n(\theta)$, giving rise to n "lobes" of field lines between $\theta = 0°$ and $\theta = 180°$, each lobe being bounded latitudinally by radial lines along which $(^{dP}n/d\,\theta)$ $(\sim B_\theta) = 0$. For appropriate n, one lobe will span the latitudes covered by a given active region. For example, Figure 6.4.6 shows selected field lines for the sixth lobe (from the north pole) of a P_{17} field, for several values of the neutral point height $y = r_1/r$. This particular lobe is centered at colatitude 59.1° and has a latitudinal width of 10.3°.

The total magnetostatic energy $\int(B^2/8\pi)\,dV$ of a single lobe, per radian of longitude, as a function of the neutral point height is:

$$E^{(n)}(y) = \frac{\beta^2 r_o^{\,3}\ y^{2n+1}}{8\pi}\ \{(n(n+1) + (n+1)y^{2n+1} - n/y^{2n+1}\}\ \ I_{12}{}^{(n)} \tag{6.4.8}$$

$$I_{12}^{(n)} = \int_{x_1}^{x_2} P_n^2\,(x)dx \tag{6.4.9}$$

$$\beta = B_o/\{n+(n+1)(r_1/r_0)^{2n+1}\} \tag{6.4.10}$$

where the limits of integration x_1 and x_2 correspond to the latitudinal boundaries of the lobe (i.e., the points at which $dP_n/d\theta = 0$) and B_o is the field strength at the poles ($\theta =$ 0°, 180°). This stored energy decreases as the neutral point rises higher in the corona:

$$\frac{dE}{dy} = -2n(n+1)(2n+1)^2 b^2 y^{2n}(y^{2n+1}-1)\,\{n + (n+1)y^{2n+1}\}^{-3}, \tag{6.4.11}$$

where $b^2 = r_o^{\,3}\ B_o^{\,2}\ I_{12}{}^{(n)}/8\pi$. We identify $-dE/dt = -(v_n/r_o)dE/dy$, where $v_n = dr_1/dt$ is the upward velocity of the neutral point, as the rate at which energy "reappears" in the flare plasma in an observable form. If we assume that some fraction, f, of this liberated energy is used to supply the thermal energy density, e, of newly formed flare loops, then we can write

$$e = 3N_e kT = -f\frac{dE}{dr_1}\left(\frac{dV}{dr_1}\right)^{-1}, \tag{6.4.12}$$

where dV/dr_1 is the rate at which the volume of the loop system, V (per radian of longitude), grows as the neutral point rises. Let L denote a characteristic arc length over which the enhanced thermal energy of a newly formed loop is significant. Then we can write $dV \simeq L\,dr_1\,r_1 \sin\langle\theta\rangle$, where $\langle\theta\rangle$ is the mean latitude of the loop system. For the reasonable assumption that L is twice the loop height, i.e., $L = 2r_0(y-1)$, Equations (6.4.11) and (6.4.12) yield

$$e = \frac{n(n+1)(2n+1)^2 B_0^2 I_{12}{}^{(n)}\ f}{8\pi\ \sin\langle\theta\rangle}\left(\frac{y^{2n-1}}{y-1}\right)\left(\frac{y^{2n+1}-1}{\{n+(n+1)y^{2n+1}\}^3}.\right) \tag{6.4.13}$$

To apply Equation (6.4.13) to a particular flare, we have to know the variation of neutral point height with time. For flares near the solar limb, this information may be derived directly by measuring the height of the highest (i.e., most

FIELD LINE TOPOLOGIES
FOR A SECTION OF A P_{17} FIELD

SIXTH LOBE: $\theta_1 = 25\overset{\circ}{.}75$, $\theta_2 = 36\overset{\circ}{.}05$

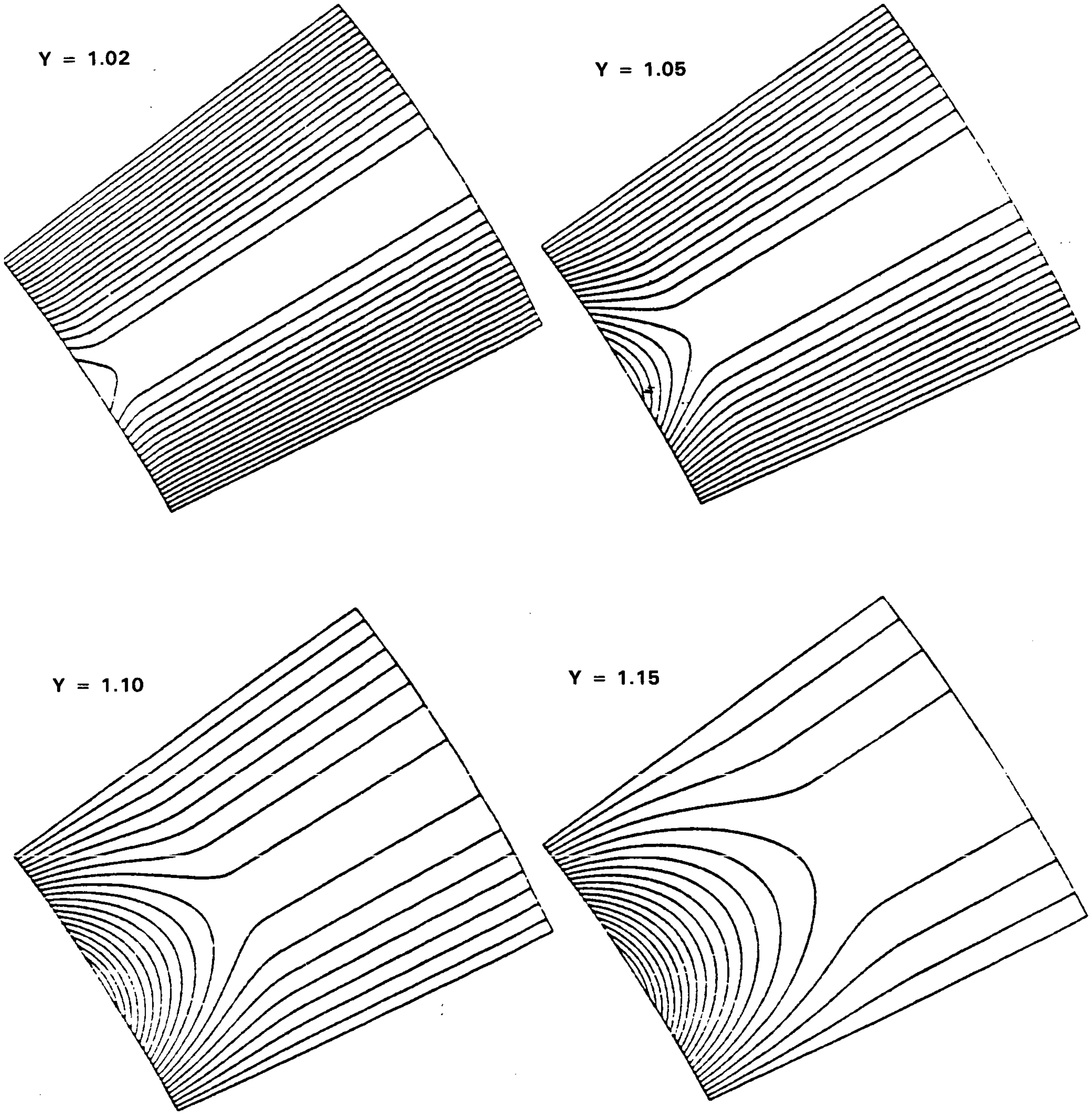

Figure 6.4.6 Selected field lines for the sixth lobe of a P_{17} field as a function of the height of the neutral point (source surface).

recently formed) X-ray loops, since the neutral point supposedly lies immediately above. However, for flares near disk center we recall that the highest X-ray loops visible at any time appear to have their footpoints anchored in the *leading edges* of the expanding H-alpha ribbons. Using the field representation developed above, we can calculate numerically the neutral point height, y, which gives a magnetic separatrix which intersects the solar surface with a footpoint separation corresponding to that of the ribbon's leading edges at any time. As a test of this procedure, we present the results of such a calculation for the well-observed disk flare of 29 July 1973; this classical two-ribbon flare occurred sufficiently far away from disk center that both ribbon separations and loop heights were simultaneously measurable during the later stages of the event and are available in the published literature (Moore *et al.*, 1980).

The latitude and size of this flare suggest that the eighth lobe of a P_{18} field is appropriate. We adopt the values of Moore *et al.* (1980) for the average separation of the leading edges of the H-alpha ribbons (cf., their Figure 8.4) and for the height of the brightest X-ray emission (their Figure 8.5). From these data we derive the empirical relationship between hot-loop height and ribbon separation shown by the filled circles in Figure 6.4.7 (error bars from Nolte *et al.*, 1979). During the time interval 16:43-21:41 UT, the loop-height observations are fit well by the theoretical run of neutral point height versus separatrix-footpoint separation.

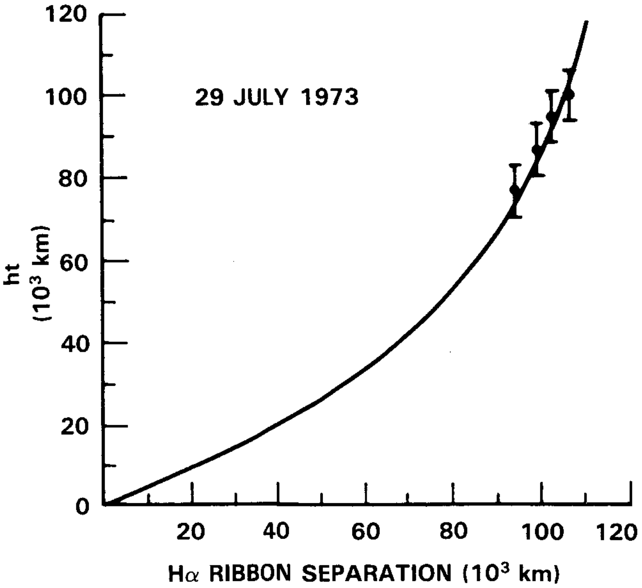

Figure 6.4.7 The heights of the hottest loops seen in X-rays appear to incresae as the H-alpha ribbons separate; the filled circles correspond (left to right) to the observed loop heights at 1643, 1821, 1958, and 2141 UT, respectively. The solid curve depicts the height of the neutral point as a function of the separatrix-footpoint separation for the magnetic field configuration described in the text.

The goodness of fit thus obtained suggests using the theoretical curve to extrapolate the empirical relationship to earlier times in the flare, when soft X-ray images are not available. Combining this extrapolation with the ribbon-separation observations of Moore *et al.* (1980) yields the neutral point history shown by the filled circles in Figure 6.4.8; the smooth curve represents an analytical fit to these results, namely

$$y(t) = 1.06704 + 2.927 \times 10^{-2} \log (t-t_0) , \quad (6.4.14)$$

where t is in hours (UT) and $t_0 = 13.078$.

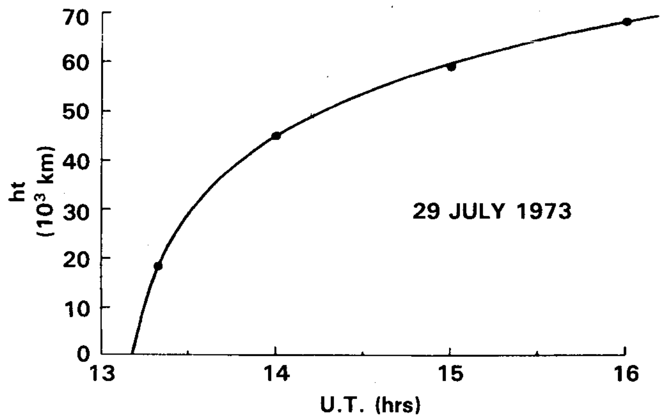

Figure 6.4.8 Temporal variation of the height of the neutral point for the 29 July 1973 flare, as calculated from Equation (6.4.22).

The solid curve in Figure 6.4.9 shows the temporal variation of plasma energy density as calculated from this fit and Equation (6.4.13). The parameter values assumed were $B_0 = 1600$ G (which gives a peak field strength in the magnetic lobe representing the flare region of about 300 G; cf. Michalitsianos and Kupferman (1974)) and f = 0.003. This value of f was chosen to fit the energy density profile (vertical bars in Figure 6.4.9) calculated from the flare-plasma temperature and density values as determined from SOLRAD full-disk data as revised by Svestka *et al.* (1982). The small value thus derived implies that only a tiny fraction of the total magnetic energy stored in the active region corona apparently need be used to account for the presence of hot plasma on flare loops.

In this project we emphasize two major points pertaining to the reconnection theory for two-ribbon flares. The first is that the theoretical magnetic field model should have a spacial scale and orientation corresponding to that of the active region within which the flare occurs. Most large two-ribbon flares occur in active regions characterized by a bipolar field configuration oriented more-or-less in the north-south direction. To meet this requirement, we have chosen to represent the observed photospheric field distribution in

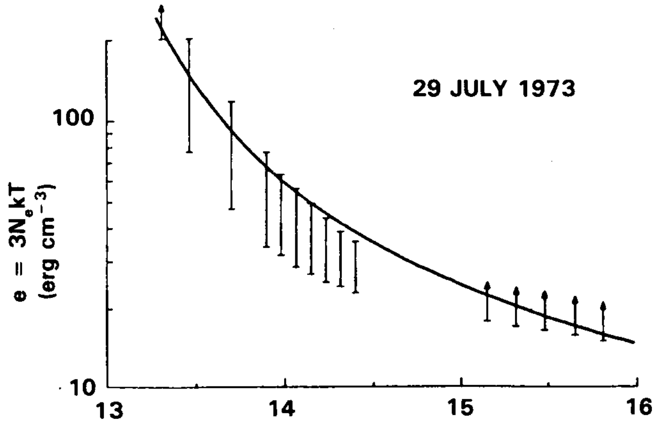

Figure 6.4.9 Thermal energy density of plasma on closed loops for the 29 July 1973 flare. The data (vertical bars) were taken from Svestka *et al.* (1982), whereas the smooth curve was calculated from Equations (6.4.13) for the parameter values given in the text.

and around the flare site by a single high-degree term of the Legendre-polynomial series expansion that comprises the general solution of Laplace's equation. Also, we have imposed the additional boundary condition that the field lines become radial at the level of the neutral point (more correctly, neutral "line") which rises into the corona as reconnection proceeds, and that they remain radial beyond this level (source-surface model). The resulting field contains volume currents everywhere above the source surface and a current sheet extending radially outward from the neutral point itself. There is no necessity to align the axis of symmetry with the rotational axis since we confine ourselves to a finite sector in longitude. For H-alpha ribbons not in an east-west orientation, we can relocate the axis of symmetry so that the field lobe of interest runs parallel to the observed H-alpha ribbons.

The second point is that, as the flare progresses, the new closed loops which are being formed continually via reconnection represent an increase of total volume of the loop system with time. A proper accounting of this growth is necessary if one is to relate the net rate of reconnection-liberated *energy* to the *energy density* of the plasma trapped on these closed field lines. Our approximate treatment of the increasing loop dimensions leads to an expression for the hot-plasma energy density which *declines monotonically with time*, once the reconnection phase has commenced. This is in good agreement with observations for the 29 July 1973 flare, thereby representing a major improvement over the results of earlier analyses (e.g., Pneuman, 1980) which indicated that the energy density should increase rapidly from zero at flare onset to a maximum value a short time after the onset of reconnection.

Finally, only a very small fraction (0.003) of reconnection-liberated magnetic energy was needed to account for the thermal energy density on the hot loops of the 29 July 1973 flare. This shows that the postulated field configuration contains much more energy than is actually needed to supply these losses. From Equation (6.4.8), when the neutral point rises from the solar surface ($y = 1$) to infinity, the total energy released per radian of longitude is found to be

$$\Delta E_{12}^{(n)} = \frac{r_o^3 \, I_{12}^{(n)} \, B_o^2}{8\pi}\left(\frac{n}{n+1}\right), \qquad (6.4.15)$$

and for the parameters $n = 18$, $B_o = 1600$ G, and $I_{12}^{(n)} = 2.93 \times 10^{-3}$ representing the 29 July 1973 flare, it follows that $\Delta E_{21}^{(n)} \cong 10^{35}$ erg/radian. The longitudinal extent of the active region was about 2×10^5 km, so that the net available magnetostatic energy is about 3×10^{34} erg. In actuality, the field at flare onset may not be opened up all the way down to the solar surface, and the neutral point will not rise to infinity. Both of these effects tend to reduce the energy actually accessible by reconnection. Even if the range of neutral point heights is limited to that shown in Figure 6.4.8. (i.e., 18,000-70,000 km), it can be shown from Equation (6.4.8) that about two-thirds of the above energy, or 2×10^{34} erg, will be liberated. This rather large energy — two orders of magnitude higher than the observed flare losses — is consistent with the small fraction found necessary to account for the hot-loop plasma.

We deem it unlikely that future refinements in the potential-field/source-surface model presented in this paper will be of a sufficient magnitude to remove the energy disparity noted above. A more promising possibility is that the rate of reconnection is physically limited to values lower than those otherwise desired by external inflow conditions; i.e., the reconnection is "forced". A restricted merging rate could produce a post-reconnection, three-dimensional, field configuration (e.g., force-free) after only a small fraction of the energy of the original open field has been shed.

6.4.6 Linear Stability of Magnetostatic Coronal Structures

In the low corona, where the solar wind may be neglected, long-lived structures are in approximate magnetostatic equilibrium. These structures may evolve quasi-steadily. Calculations have been presented to suggest that a quasi-steady evolution may terminate in an unstable equilibrium state, whereupon the coronal structure appears to break spontaneously into a dynamical state (Low, 1981; Wolfson, 1982). Such a process may be the origin of some coronal mass ejections, particularly those associated with eruptive prominences without flares (e.g., Low, Munro, and Fisher, 1982). It is worthwhile, therefore, to study what kind of magnetostatic states are stable, and what others are not, in the low corona. Problems in MHD stability are formidable, and our theoreti-

C-5

cal knowledge is limited because the stability analyses can be carried out only for equilibrium states of the simplest geometries. There are two main technical difficulties. Equilibrium states of complex, but realistic, geometries usually cannot be written down in analytic forms to allow the usual expansion for the linearized perturbation equations. Even if the linearized perturbational equations were available, the equilibrium state description usually introduces such spacially-varying coefficients into the equations as to make the mathematical problem intractable. Low (1984b) presented a theoretical study in which these two difficulties are overcome and several analytic magnetostatic equilibrium states with known stability properties are made available. Magnetostatic equilibrium is described by the equation:

$$\frac{1}{4\pi}(\underline{\nabla} \times \underline{B}) \times \underline{B} - \underline{\nabla} p - \varrho \frac{GM_0}{r^2}\hat{r} = 0 \,. \quad (6.4.16)$$

Assuming axisymmetry, this equation can be reduced to a non-linear, elliptic, partial differential equation in the r-θ plane (Hundhausen, Hundhausen, and Zweibel, 1981; Uchida and Low, 1981). The following solution describing $\gamma = 6/5$ polytropic, axisymmetric atmosphere can be constructed by solving this elliptic equation:

$$\underline{B} = B_0 \left(\left(\frac{\cos\theta}{r^4}\right)\hat{r} + \left(\frac{\sin\theta}{r^4}\right)\hat{\theta} \right), \quad (6.4.17)$$

$$p = \frac{1}{6}\left(W_0 - W_1 \frac{B_0}{2}\frac{\sin^2\theta}{r^2}\right)\left(\frac{GM_0}{r}\right)^6, \quad (6.4.18)$$

$$\varrho = \left(W_0 - W_1 \frac{B_0}{2}\frac{\sin^2\theta}{r^2}\right)\left(\frac{GM_0}{r}\right)^5, \quad (6.4.19)$$

where W_0 and W_1 are free constants and $B_0 = \pi W_1 (GM_0)^6/3$. This analytic solution is displayed in Figure 6.4.10; the geometry is shown by the solid lines in panel (a). Superposed is a set of broken lines representing the potential magnetic field having the same normal flux distribution at the reference level $r = R_0$. Panel (b) shows contours of constant density. The axisymmetric density distribution is characterized by a density depletion low in the equatorial region. This equilibrium state may be visualized to have been formed in the following manner. Consider the initial equilibrium state in which an atmosphere is in spherically-symmetric hydrostatic equilibrium with the potential magnetic field shown in panel (a) of Figure 6.4.10. If we slowly remove plasma from the low equatorial region, the reduced pressure in this locality will not be able to support the weight of the upper atmosphere. Adjustment to new equilibrium states results, and the atmosphere weighs upon the magnetic field, deforming it into the geometry of the non-potential field shown.

The global force balance of the equilibrium state in Figure 6.4.10 may be described in the following terms. The density depletion in the low equatorial region is buoyant in the stratified atmosphere. The lower pressure of the depletion region does not result in its collapse because of its locally large magnetic pressure. The buoyant depletion region is prevented from rising by the downward-acting magnetic tension force. In this equilibrium, gravity has its role to play through the buoyancy force.

The equilibrium state just described can be subjected to a vigorous stability analysis, using the energy principle of Bernstein *et al.* (1958), assuming rigid boundary conditions at $r = R_0$ and linear perturbations. The mathematical analysis in Low (1984b) establishes the following results. The equilibrium state contains two free parameters, W_0 and W_1 in Equations (6.4.17)-(6.4.19). For all values of W_0 and W_1 the equilibrium is unstable. However, instability appears only for perturbations with variations in three-dimensional space. The equilibrium state is stable to all axisymmetric perturbations. The detailed analysis shows that to excite an instability, the perturbation must involve a displacement perpendicular to the magnetic field in the r-θ plane combined with a ϕ-dependent displacement out of the r-θ plane. An obvious example of this type of perturbation is one due to a particular magnetic flux tube rising outward in its r-θ plane. In so doing, the flux tube expands and pushes aside the neighboring magnetic flux tubes. In the three-dimensional development, we find strands of magnetic flux pushing their way out, destroying the axisymmetry of the initial equilibrium state. Finally, this instability is confined to magnetic field lines which subtend angles at $r = R_0$, between their pairs of footpoints, exceeding about 45. Hence, if the equilibrium is perturbed, instability sets in for the larger magnetic arches that extend high up in the atmosphere. Other magnetostatic equilibria and their stability, as well as a discussion of their relation to mass ejections, can be found in Low (1984b).

Stability analyses establish properties on a firm basis whenever they can be carried out completely. Obviously, many more studies are needed before we can synthesize a broad understanding of stability properties of relevance to coronal structures. From this synthesis, we can hope that a theory will emerge as to why certain coronal structures may become unstable and develop into large scale outflows to be identified with the mass ejection phenomenon.

6.5 INTERPLANETARY EFFECTS OF CORONAL MASS EJECTIONS

6.5.1 Introduction

The mass, energy, and volume observed in the Skylab coronal mass ejections implied that the consequent interplanetary effects of CMEs should be similarly dramatic and readily observed at 1 AU. The association of interplanetary (Gosling *et al.*, 1975) and coronal (Gosling *et al.*, 1976) shocks with fast CMEs seemed to confirm this point of view.

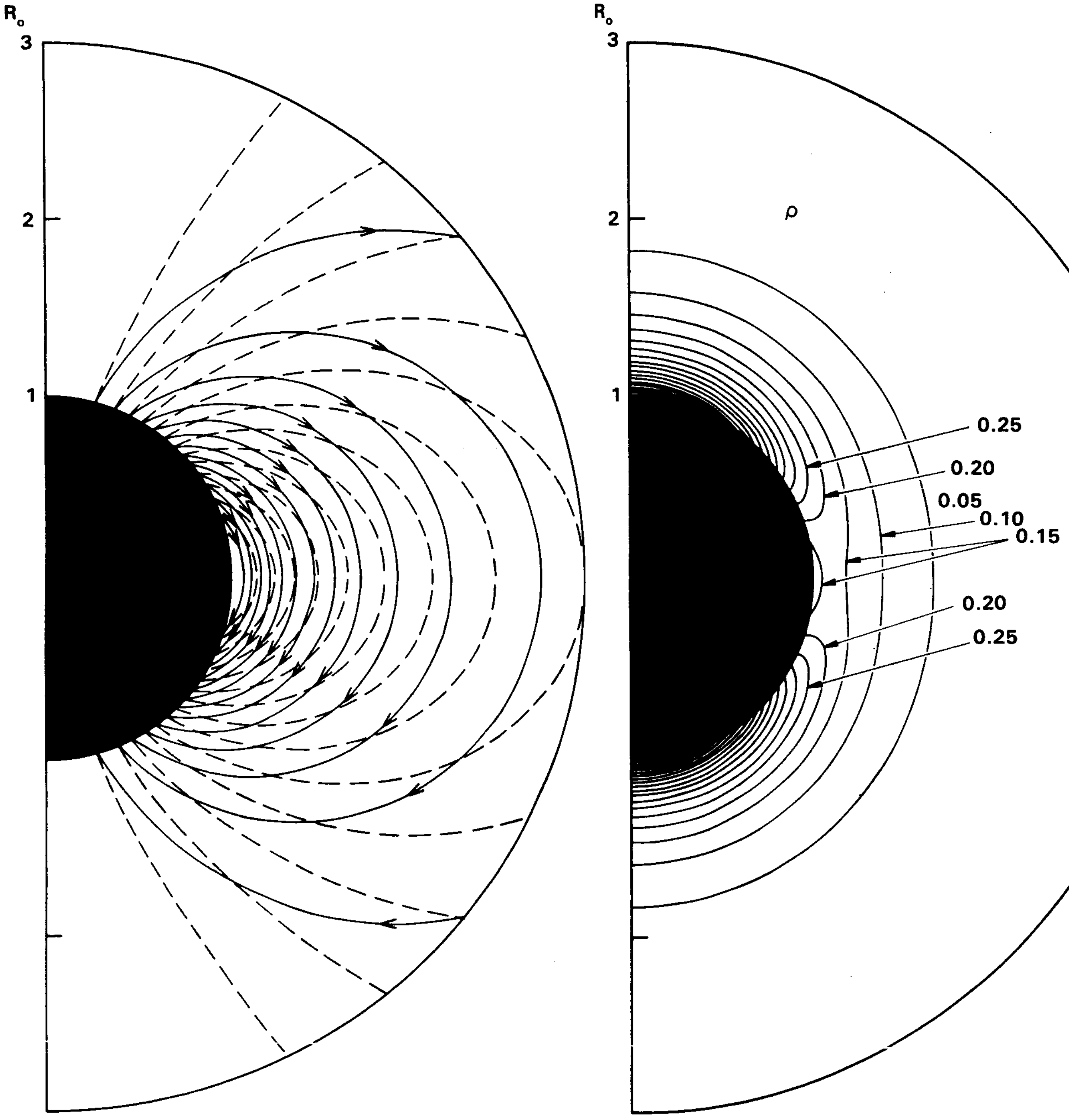

Figure 6.4.10 A particular axisymmetric magnetostatic solution. The left figure shows the magnetostatic field in solid curves and the associated potential magnetic field in broken curves. The right figure shows the distribution of the density ρ.

The realization that the mechanical energy released in mass motions dominates the easily observed radiative output of associated large flares (Webb *et al.*, 1980) further enhanced this expectation.

The results to date have been rather surprising. The principal effects of CMEs — interplanetary shocks and energetic particle events — appear well associated with major CMEs, but the detection of CMEs themselves at 1 AU has remained elusive. Gosling *et al.* (1977) suggested that non-compressive density enhancements (NCDEs) observed in the solar wind were the interplanetary signatures of CMEs. Another attempt to detect CMEs at 1 AU has been carried out by Klein and Burlaga (1982), who observed "magnetic clouds", regions in which the magnetic field has rotated nearly in a plane, perhaps indicating a loop-like structure. A third approach has been to associate solar wind helium abundance enhancements (HAEs) with CMEs (Borrini *et al.*, 1982). The lack of correlation among NCDEs, magnetic clouds, and HAEs, however, suggests that the interplanetary signatures of CMEs may show considerable variations (Borrini *et al.*, 1982).

In the remainder of this section, we discuss the results of team members engaged in efforts to clarify the interplanetary signatures of CMEs and follow that with a review of work on associating CMEs, interplanetary shocks, and energetic particles.

6.5.2 Direct Detection of CMEs in Interplanetary Space

Klein and Burlaga (1982) surveyed hourly averages of interplanetary magnetic field and plasma data from 1967 to 1978 to search for "magnetic clouds." The clouds are defined as regions with radial dimensions of ~0.25 AU in which the magnetic field strength is high and varies so that the measured field direction rotates substantially, nearly parallel to a plane as the cloud passes over a spacecraft. These criteria sieved out 45 identified clouds, which Klein and Burlaga listed in three classes, depending whether each cloud followed a shock, preceded a stream interface, or was a cold magnetic enhancement. Each class had about the same number of clouds, and it was suggested that all clouds arose from the same basic physical cause but found themselves in different environments in the solar wind. The sums of the magnetic and ion pressures in the clouds were higher than the ion pressure outside, implying that the clouds were expanding. Klein and Burlaga suggested that these magnetic clouds might be the 1 AU manifestations of CMEs.

The Klein and Burlaga analysis did not include a search for the solar origin for each of these magnetic clouds. Wilson and Hildner (1984) undertook to search for the solar origins of the 35 clouds observed from 1971-1978. For each cloud they determined a temporal window, based on the maximum and minimum wind speeds observed within each cloud, during which the cloud must have departed the Sun. They then looked for solar activity which might serve as proxy indicators of the occurrence of a CME within each window. As proxy solar events for CMEs they examined H-alpha flares, Type II and IV radio events, radio GRF events and soft X-ray events listed in *Solar Geophysical Data*. The same proxy phenomena were also examined for temporal windows when no clouds were observed, i.e., for control periods. No significant proxy events were found, relative to the control periods, for the clouds associated with stream interfaces and cold magnetic enhancements. However, for six of the nine clouds associated with shocks, Wilson and Hildner found a Type II burst originating within 49° of central meridian during the event window. Of nine control windows, only three contained a Type II burst and each of those was at least 63° from central meridian. On the assumption that Type II bursts are well correlated with fast CMEs, which are likely to result in interplanetary shocks, Wilson and Hildner (1984) find support for the idea that fast CMEs are expelled nearly radially from the Sun to become shock associated magnetic clouds at 1 AU. Caution about the hypothesis is urged because of the very sparse statistics involved (six of nine cases) and because for three of the six good cloud associations the Type II bursts were associated with H-alpha subflares. The recent study of Kahler *et al.* (1984a), shows that about 2/3 of all Type II bursts associated with subflares are *not* associated with CMEs. It is discouraging that the solar signature of the large group of magnetic clouds not associated with shocks is still undetermined.

The attempts to observe CMEs at 1 AU through their particle or magnetic field signatures, as discussed above, lack the global perspective with which CMEs are first observed in coronagraphs. However, as mentioned in Section 6.2.1.8, Jackson has shown that there is a way to observe CMEs globally beyond 10 R_0. As first discussed by Richter, Leinert, and Planck (1982) the zodiacal light photometers on the two solar-orbiting Helios spacecrafts can be used to observe interplanetary plasma clouds and to determine their velocities. Each Helios experiment consists of three photometers pointed at ecliptic latitudes of 16°, 31°, and 90°, with Helios 1 viewing the southern hemisphere and Helios 2 the northern. The spin axes point to the ecliptic poles, and the 16° and 31° photometers sample 32 positions of azimuth through various color filters and polarizers (Leinert *et al.*, 1975; 1981).

Jackson has shown that several CMEs observed with the SOLWIND and SMM coronagraphs can be tracked well into the interplanetary medium using the Helios data (Jackson *et al.*, 1985a,b), and he has used a program to plot brightness contours (and excess density contours deduced from them) in a "fisheye" lens view that shows the shape and position of the CME as seen from Helios, relative to the Sun and Earth. For some CMEs seen in projection with coronagraphs in near-Earth orbit, this offers the possibility of a "stereoscopic" view of their shape and evolution. Figure pairs 6.2.21-6.2.22 and 6.5.1-6.5.2 show coronagraph and Helios views of the 24 May 1979 and 29 June 1980 mass ejections, respectively.

The Helios photometer data do have several important limitations which must be considered. CMEs cannot be observed until they are at least 15 R_0 away from the Sun, even under the most favorable circumstances. The best observations are obtained when the CMEs are several tenths of an AU distant from the Sun. This makes detailed comparisons with coronagraph observations difficult (Jackson *et al.*, 1985a). In addition, the brightness variation due to the Thomson scattering angle and the distance of the CME electrons from the Sun is substantial, which leads to a considerable uncertainty in deconvolving the CME shape from the Helios observations. It is also necessary to assume the distributions of material along the photometer line of sight to determine the total mass in the field of view. Nevertheless, the Helios data allow one to determine the general size and position of

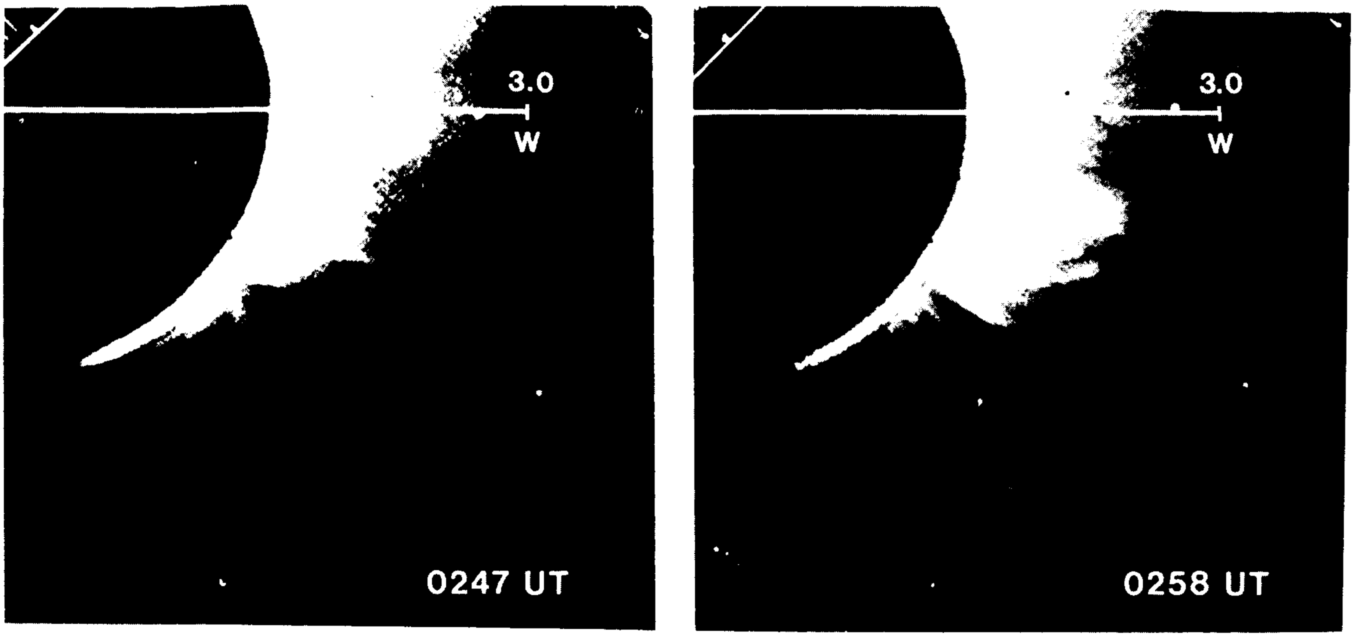

29 JUNE 1980

Figure 6.5.1a Coronagraph observations of the early 29 June 1980 mass ejection. (a) C/P observations. In these views of the low corona the ejection is clearly observed as a complex loop system. The coronagraph's occulting disk is at 1.6 R_0 and the field of view extends outward as indicated.

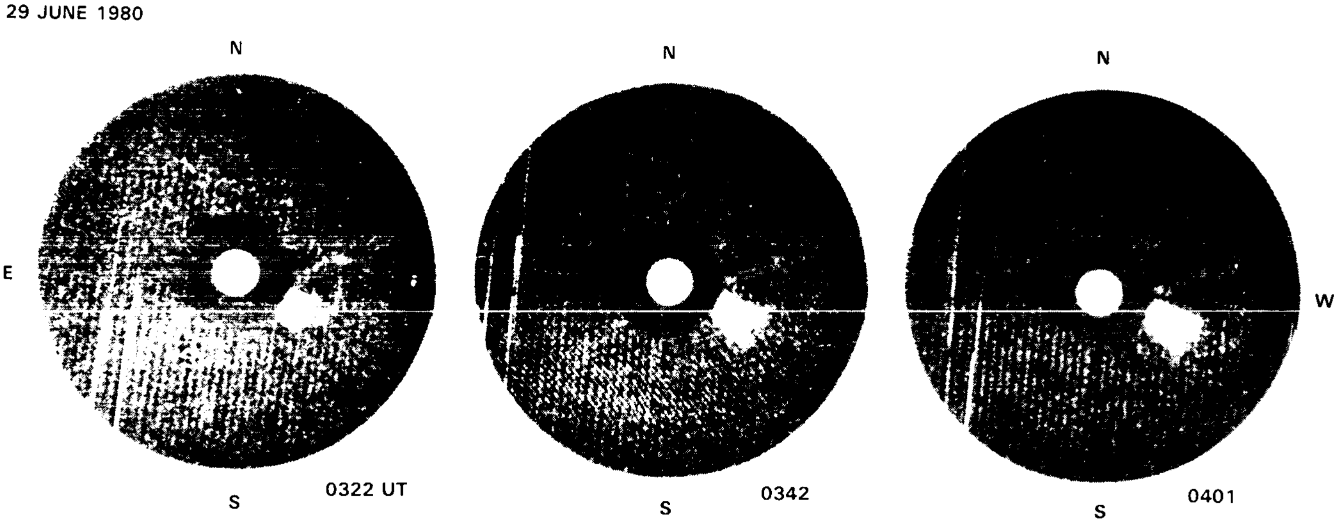

Figure 6.5.1b Coronagraph observations of the early 29 June 1980 mass ejection. (b) SOLWIND coronagraph difference images later in the event.

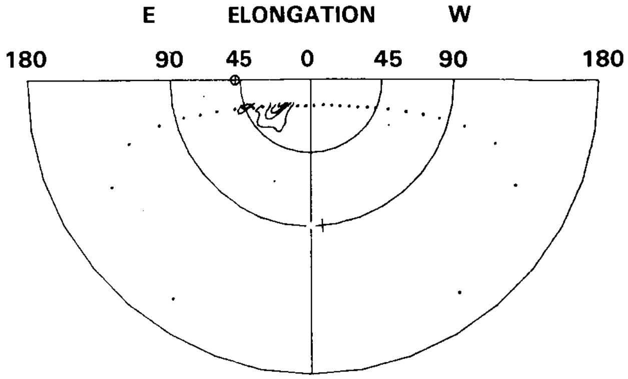

1800 UT 30 JUNE 1980

Figure 6.5.2 Helios 1 contour image of the 29 June 1980 mass ejection at 1800 UT 30 June 1980 in levels of 6 × 10^{12} g deg^{-2}. The Sun is centered, and the point behind the observer on the spacecraft, i.e., at 180° elongation is represented as the outer circle. The position of the Earth (⊕) and the solar pole are indicated relative to the ecliptic plane (horizontal line).

a CME as it moves through the interplanetary medium. Further work should help to elucidate the hitherto elusive nature of CMEs at 1 AU.

6.5.3 Interplanetary Shocks and Energetic Particles Associated with CMEs.

The large (≳1000 CMEs) SOLWIND data set has provided an excellent base for studying CME associations with interplanetary shocks and energetic particles. Using the Max Planck Institut's plasma detector on the Helios 1 spacecraft to detect interplanetary shocks, Sheeley *et al.* (1983b, 1985) carried out a direct comparison of CMEs and interplanetary shocks. For 80 shocks detected while Helios 1 was within 30° of the Sun's east or west limb and for which there were complementary SOLWIND observations, 40 appropriately-timed, well-associated, major CMEs were found. For the 40 remaining shocks, 19 "possible" associations were found, "possible" for a variety of reasons, and for 20 shocks associations with CMEs were "indeterminate". The associated CMEs generally encompassed the ecliptic plane and usually (but not always) had speeds exceeding 400 km s^{-1}. If one starts with CMEs and asks how many had Helios-observed shocks associated with them, the following answers emerge. There were: 27 major CMEs in Helios' hemisphere not initially associated with Helios shocks; 17 of these did not encompass the equator, i.e., no part of the CME went in the direction of Helios; the remaining 10 grazed or spanned the solar equator, and 7 of these failed to be associated with shocks, though 5 of these 7 were associated with disturbed flows, including NCDEs.

Although this initial association study suggested a strong CME/shock correlation, several questions remained. The first was the origin of the "possible" category of events, which consisted of one-quarter of the sample for which adequate data existed. Second, although the CME occurrence rate was 0.9 major events per day, (Howard *et al.*, 1985), the rate for large, low-latitude CMEs on Helios' limb was only 0.15 per day, making unlikely the occurrence of many random, chance associations. As Sheeley *et al.* (1983b) pointed out, the shock-associated CMEs were generally bright, fast, low-latitude events not typical of CMEs in general.

As a test of their CME associations Sheeley and his colleagues (Sheeley *et al.*, 1985) updated their original list of Helios shocks to 99 events and matched them and (for control) a comparable set of randomly generated "shock" times with their CME data (see Table 6.5.1).

Table 6.5.1 CME Associations with Helios Shocks and Random Times

	Helios Shocks	**Random "Shocks"**
Yes	49 (72%)	7 (16%)
Possible	18 (26%)	15 (34%)
No or Doubtful	1 (2%)	22 (50%)
Indeterminate	21	40
Helios More Than 30° Away From Limb	10	15
	99	99

As the percentages in Table 6.5.1 show, when the indeterminate and poor Helios geometry cases are eliminated, there was close temporal association with a CME for 72% of all observed shocks, but an apparent association for only 16% of the random periods or control "shocks". In addition, where half the random "shocks" had no CME association, only one (2%) Helios shock was similarly unassociated. This result establishes that about 70% of the Helios shocks are, in fact, associated with CMEs, although the origin of the remaining 30% of the Helios shocks is unclear. In addition, the relationship between coronal shocks, observed as metric Type II bursts, and interplanetary shocks is also unclear, despite the work of Cane (1984); considerable work is still required to obtain a comprehensive view of these shocks. Results obtained by Kahler and his colleagues (Kahler *et al.*, 1984b) suggest that the earlier picture that all prompt, i.e., flare associated, proton events are associated with CMEs (Kahler, Hildner, and van Hollebeke,

1978) needs some revision. They found that 26 of the 27 prompt proton events with identified H-alpha flares also had associated CMEs. The one exception, on 7 June 1980, is one of what may be a rare class of events which are associated with short duration, well-connected (W50-W90) flares with no CMEs. These unusual events tend to have γ-ray emission and strong Type III bursts, suggesting a prominent role for the impulsive phase in the production of interplanetary energetic protons despite their lack of CMEs.

A further complication has been found in the sources of the ^{3}He-rich energetic particle events. In these events the ratio ^{3}He/^{4}He exceeds 0.2 at 1.5 MeV/nucleon (Reames and von Rosenvinge, 1983). Sixty-six events have been found in the GSFC ISEE-3 experiment data from 1979 to 1982. Comparing these events with metric Type II bursts and with CMEs, Kahler *et al.* (1985b) found that there was no statistically significant association of these particle events with the radio bursts nor with CMEs. The accepted view that a preheating phase selectively energizes ^{3}He ions, which are then accelerated in a second, conventional particle acceleration process, implies that ^{3}He-rich events should be significantly associated with CMEs and Type II bursts through the second acceleration process. The scenario for ^{3}He ion acceleration now appears distinctly different than for the conventional proton events and perhaps different than the proton events from the short-duration well-connected flares. These results suggest that particle acceleration processes in the solar corona may be more diverse than previously supposed.

6.6 THE SLOWLY VARYING CORONA NEAR SOLAR ACTIVITY MAXIMUM

6.6.1 Introduction

The background against which we see the continual activity of the solar maximum corona is a large scale structure, coherent over times of the order of weeks. Whether this global pattern of activity has true "time scales" and "spacial scales" in the sense of peaks in a power spectrum is as yet unknown. In this section, we present a brief view of the slowly varying component of the SMM corona, and we emphasize its interaction with the complex phenomena below it.

Since we are concerned with the aspects of long-term stability of coronal structures, we avoid any detailed investigation of the phenomena known collectively as coronal mass ejections. Thus, we explicitly restrict our discussion to time scales of about a day and longer, and spacial scales (in the upper corona) of a solar radius and greater. A short discussion of the inner corona (i.e., below the Coronagraph/Polarimeter occulting disk at 1.6 R_0) as seen by the HXIS instrument and meter-wavelength radio telescopes is given first. Then we present preliminary results of analysis of a synoptic map of the upper corona derived from SMM coronagraph observations during Carrington rotation 1693. We conclude with a glimpse of the global stability of the SMM-era corona on the time scale of multiple solar rotations, presenting pictures of the corona taken at intervals of one Carrington rotation.

6.6.2 Inner Corona

It seems obvious that the inner corona will react to the rapid evolution seen dramatically in observations of flares. However, some coronal loops at the limb, seen in X-rays, appear to have a large scale component which is almost impervious to the disruptive effects of flares, as the examples in Section 6.4.4 show. Observations of radio events also seem to provide evidence that in spite of bursts here and noise storm enchancements there, the underlying magnetic structures are fairly long-lived, evolving on time scales of a day. We discuss the joint radio and whitelight coronagraph observations of Duncan and of Pick and Trottet which bear on this interpretation.

Harrison *et al.* (1984) have studied a large coronal feature which extended above the west solar limb on 29 June 1980 (cf. Section 6.3.3.1). This feature was observed with HXIS throughout the day. The west limb was exceptionally active on this day, apparently because active regions 2522 and 2530 were near limb passage; three M-class flares occurred in these regions, and major coronal mass ejections were seen in conjunction with the first and last flares, as noted in Sections 6.2.1.6 and 6.3.3.

The coronal feature seen in 3.5-5.5 keV X-rays has been interpreted by Harrison *et al.* as a set of three loops (or loop systems) interconnecting active regions at the limb. The loop systems were seen on the first and all subsequent orbits of the day, except when the HXIS was in its flare mode, a mode in which sensitivity to low-surface-brightness features is much diminished. Figure 6.6.1 shows the appearance of the loops at 1337 UT. The loop system brightens significantly at various times during the day, often associated with the flares in the nearby active regions. The loops' brightness contours also expand upward, perhaps due to injection of material. However, despite the large energy releases during this period (one flare occurred at a footpoint of one of the loops), the same basic components are visible at the end of the day as at its beginning. This alone argues that the large-scale magnetic structure of the interconnected active regions has not been disrupted substantially by the flares, or, at least, that the large-scale configuration is re-established in a few hours or less after any disruption. The CMEs associated with the first and last X-ray flares (class M4.6 and M5, respectively) exhibited complex loop systems; see Figure 6.6.2 for representative coronagraph frames. It is unfortunate that the HXIS flare observing mode does not allow observation of the X-ray loops during the flare; we cannot know whether the X-ray-emitting loops seen before the flare are the same loops seen later, high in the corona. It may be that here we

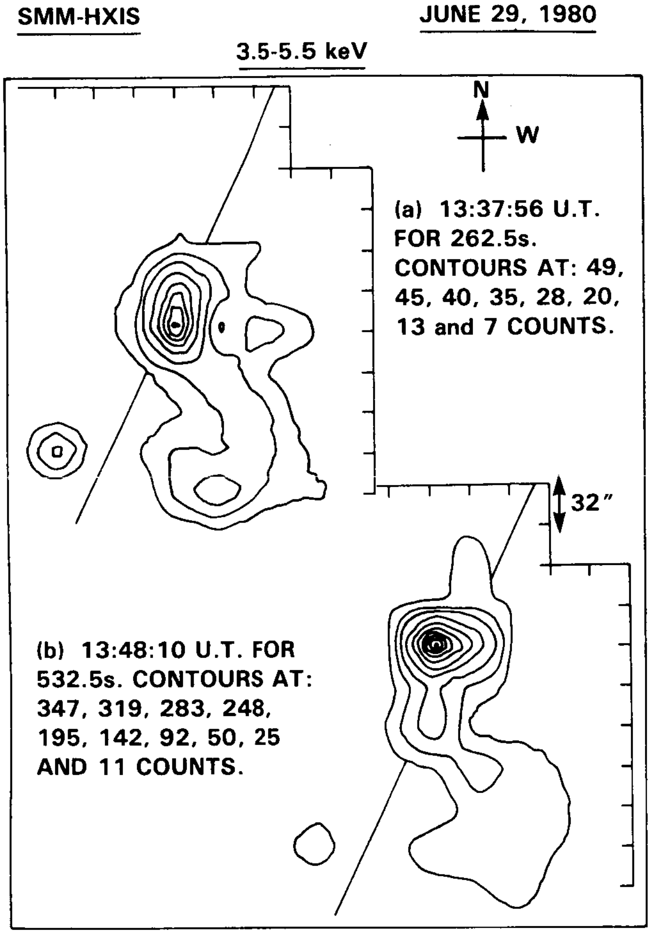

Figure 6.6.1 Contour plots showing the largest of the coronal loops seen by HXIS at the limb. The solar disk is to the left of the diagonal line, and the corona to the right (cf., Figures 6.3.3 and 6.3.4).

are seeing the "shedding" of loops by the active region as it readjusts its magnetic structure to nearly that existing before the flare. However we may speculate about the details, one striking fact remains: even in the presence of repeated large energy releases, there is a persistent skeleton of large-scale coronal features lasting at least a day.

The persistence is not absolute, however. The magnetic structure of an active region certainly changes on time scales of a day. Catastrophic changes sometimes are associated with CMEs; slower, more subtle changes also affect large-scale coronal structure. To investigate these slow changes, we turn to joint observations of the corona in whitelight and meter wavelength radio. Duncan (1983) analyzed the relation between the slow injection of mass into the corona and the appearance of radio activity (a Type I storm) under the coronal region. Duncan used a digital technique — closely akin to unsharp masking in photographic processing — to reduce the background streamer brightness levels in SMM coronagraph images. In the pictures thus processed, he followed the evolution of several coronal rays. Over several hours, the rays brightened, and a new ray was formed. The brightenings began at the ray's bases and moved upward, as if new material were being forced into the corona along thin, open flux tubes. Simultaneously with the appearance of the new ray, the Culgoora radio spectrograph recorded a Type III burst at an unknown position. Duncan suggested that the ray and Type III bursts were related. In keeping with this result, Pick *et al.* (1980) have shown that the coronal structure overlying Type III-producing regions is highly structured, with thin dense rays whose densities vary on time scales of a few hours. Similarly, Trottet *et al.* (1982) located more than 100 Type III bursts on SMM coronagraph images with positional uncertainties of 2° in latitude and 0.05 R_0 in radius. They found that Type III electron beams tend to occur where the corona is composed of small discrete rays, and that the Type III structure tends to follow that of the corona.

Even more remarkable than the appearance of the new ray in Duncan's study period was the behavior of the system of rays as a whole. Simultaneously with the appearance of the ray brightenings, the entire complex of rays began to expand latitudinally, and continued to do so for 24 hours. The centroid of the ray system remained at nearly the same position angle throughout. The Type I noise storm was motionless near this centroid. This situation was an example of the more general finding of Kerdraon *et al.* (1983), who found that noise storm onsets or enhancements are systematically associated with the appearance of additional material in the corona, often as thin rays or amorphous structures with time scales of brightness increase one hour or less. In all cases, the radio sources were cospacial with regions of coronal mass enhancements. Duncan reached the conclusion that the noise storm is likely caused by the emergence of new flux at the coronal base, precisely at the center of symmetry of the expanding ray system. This interpretation of the observations suggests that the slow evolution of the photospheric magnetic structure is indeed mirrored in the high corona. The effect in the corona is subtle, so that it may be occurring continuously but is usually overlooked because of the small amount of brightness slowly added to existing structures.

6.6.3 Outer Corona

In this section, we discuss the longest temporal and largest spacial scales accessible with the coronagraphic data from the SMM. We proceed in two steps from the scale of a day — discussed above — to the scale of several solar rotations. For the first step, we present a detailed synoptic map of the corona prepared by Illing and House for Carrington rotation 1693, and we consider what it shows regarding the large-scale characteristics of the corona. For this purpose we use the map's information about large scales, considering its high-resolution details only as they relate to global phenom-

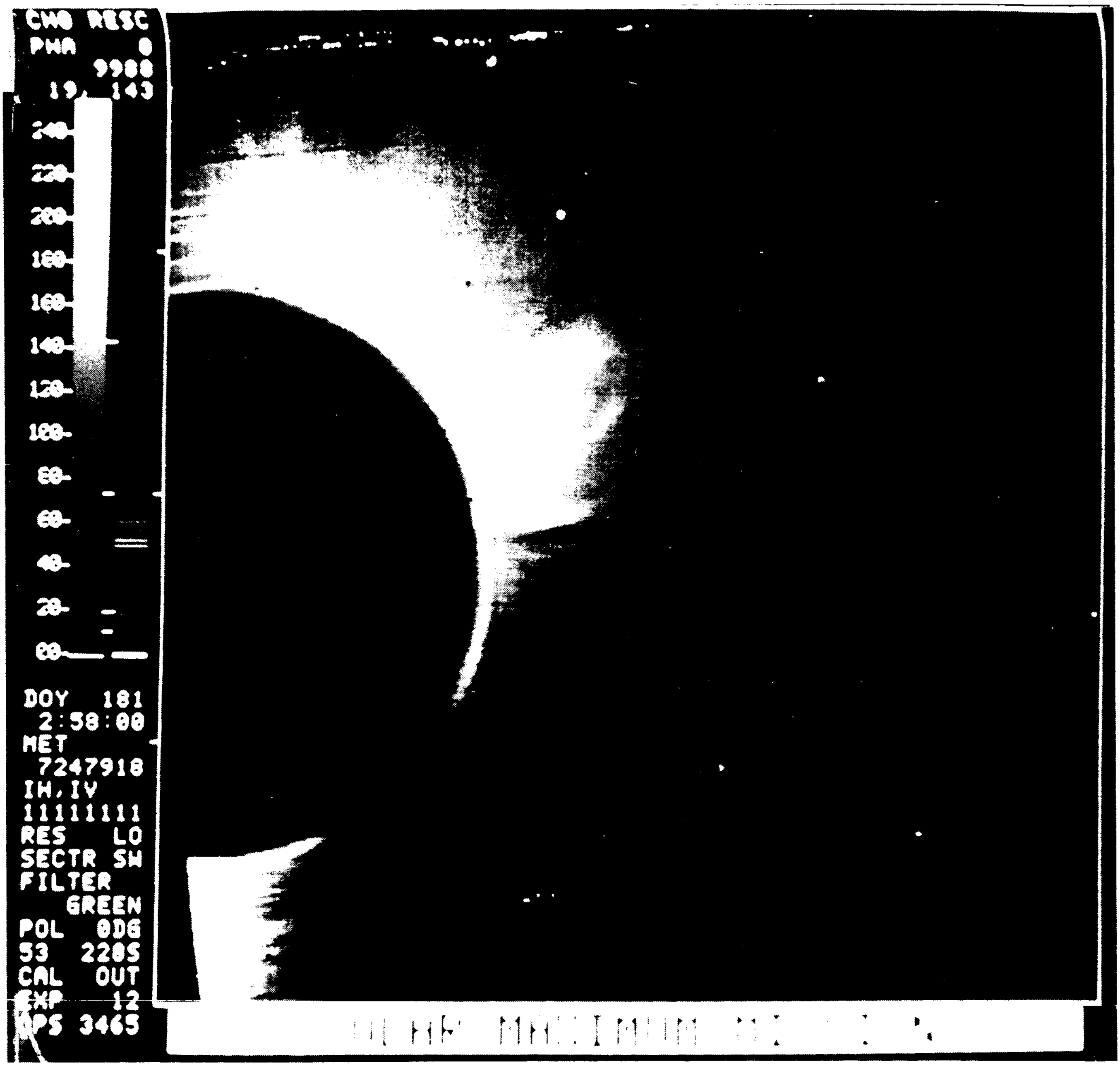

Figure 6.6.2a SMM coronagraph frames showing the 29 June 1980 CMEs associated with the flares seen with HXIS. North is to the upper left, and west to the upper right. The brightest diffraction ring around the occulting disk has a radius of 1.61 solar radii. (a) At 0258 UT.

ena. For the second step, we remark on the variability of the corona at solar maximum from one rotation to the next. The analyses of both the one-rotation synoptic map and the rotation-to-rotation variations are in an extremely preliminary state.

6.6.3.1 Coronal Variations During Rotation 1693

Figure 6.6.3 shows the intensity distribution of the corona during Carrington rotation 1693. This synoptic map was built up from vertical strips, each strip a constant-height scan of coronagraph images. The images were separated, on average, by 96 min (one spacecraft orbit), corresponding to a change of approximately 1 ° in Carrington longitude between images. However, integration along the line of sight through the optically thin corona sets the true longitude resolution of coronal features, more like 15 °. The latitude resolution was chosen to be 1 ° for convenience of presentation. Since we have not removed the tilt of the solar rotation axis, the latitude scale shown in the figure is slightly incorrect. The

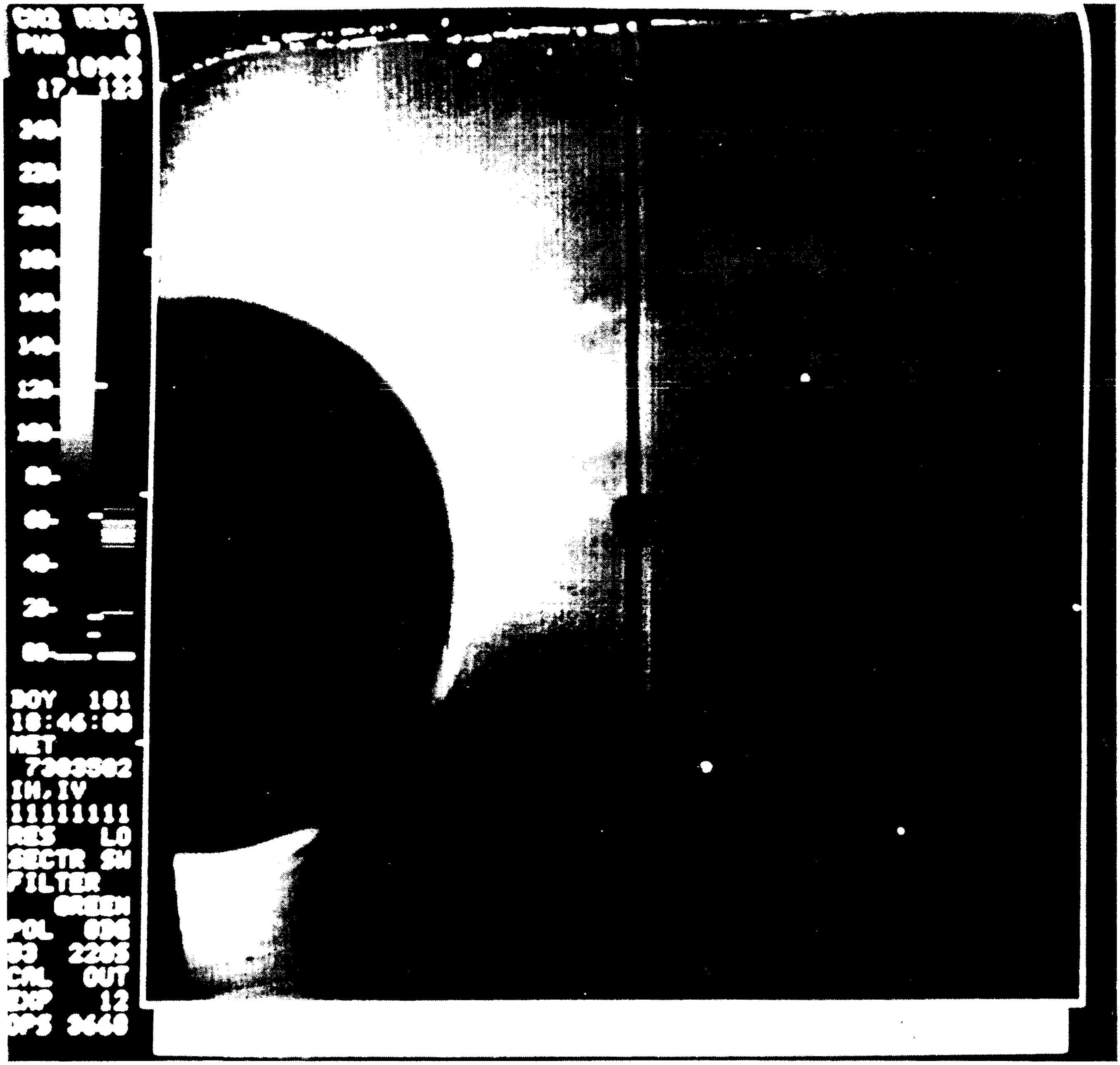

Figure 6.6.2b SMM coronagraph frames showing the 19 June 1980 CMEs associated with the flares seen with HXIS. North is to the upper left, and west to the upper right. The brightest diffraction ring around the occulting disk has a radius of 1.61 solar radii. (b) At 1846 UT.

Carrington longitude for each image (or scan) is the longitude of central meridian at the time of the image plus (for west limb images) or minus (for east limb images) 90°. We have thus assumed that the coronal features are in the plane of the sky in each image, and that the images represent the state of the corona at the Carrington longitude of the underlying photospheric and chromospheric structures. We have used only north, east, and west quadrants for the maps presented here, since a large portion of the south images is blocked by the support for the C/P's external occulting disk. The north images have been split at position angle zero into east and west sections. The Sun rotates once every 410 SMM orbits, making room for 410 constant-height latitude scans in the synoptic map; operational constraints and instrumental considerations (corrupted images, down time, special observing programs, etc.) reduced coverage by about 25%. In total, the map contains scans of over 900 quadrantal images. East limb observations of rotation 1693 are limited by the begin-

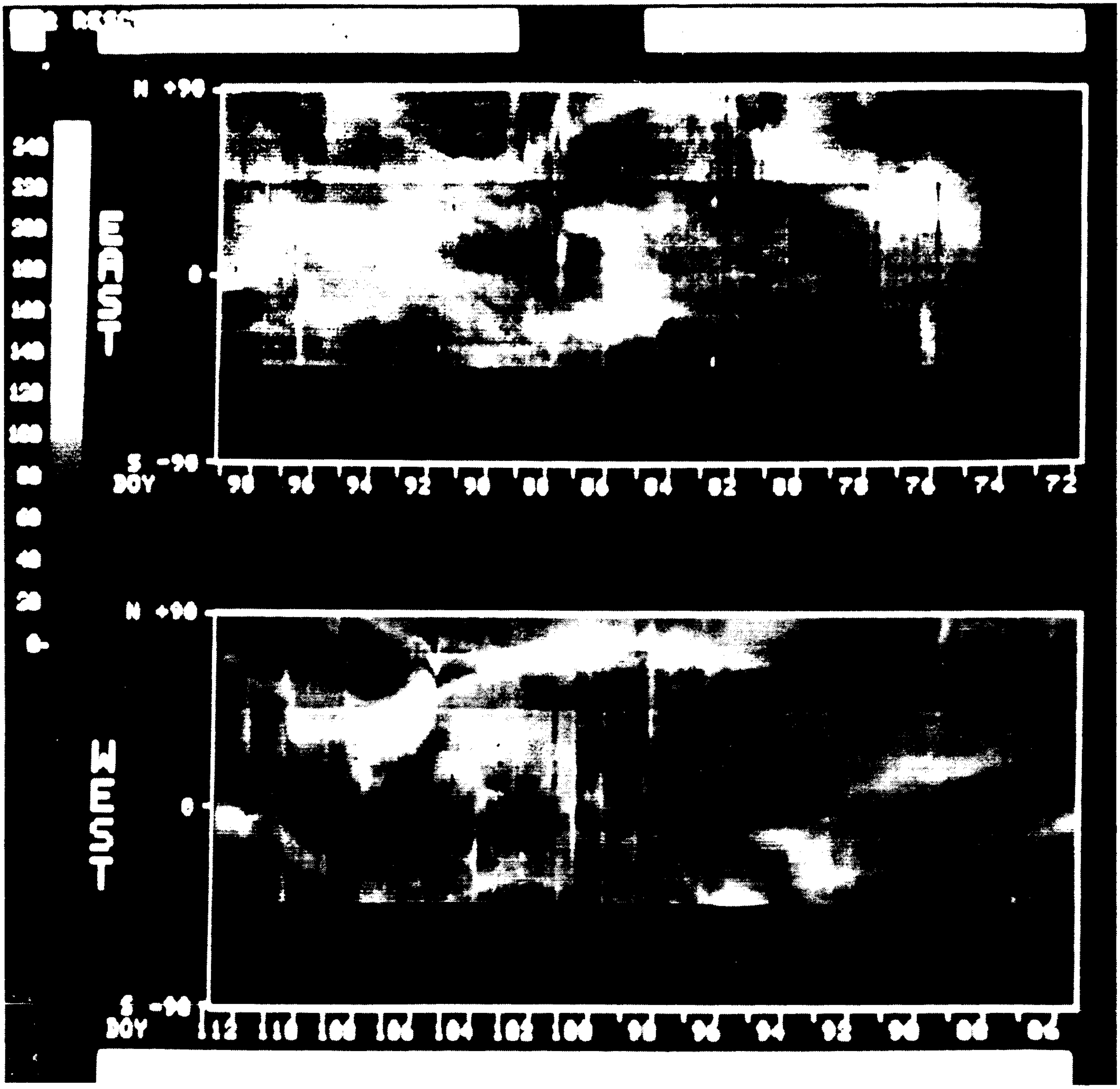

Figure 6.6.3 The detailed synoptic map of Carrington rotation 1693, at a height of 3 R_0. Time increases to the left, measured in day of year, 1980. See the text for an explanation of the construction of this map.

ning of satellite operations on 13 March 1980 (DOY73). In both east and west projections there are no data from 3-4 April 1980 (DOY 94-95) because of instrumental problems. Otherwise, missing data occur more or less at random throughout the observing interval. To minimize visual interference due to data gaps, we have interpolated the intensity distribution across the gaps in the longitudinal direction only.

Investigation of the vertical "streaks" in the synoptic map shows that about 75% are due to CMEs; the rest are due to coronal rearrangement, uncorrected photometry shifts, etc. Of the real, abrupt coronal brightenings on one limb or the other, 34 CMEs can be described as loop-like or as major disruptions of streamers. This "major event" group (for only one of five solar rotations observed in 1980) is half as numerous as the total used by Hundhausen *et al.* (1984a) in their determination of the CME occurrence rate (0.9 ± 0.15 per day, on average) for all of 1980. Hundhausen *et al.*, before Figure 6.6.3 was prepared, counted 21 CMEs in rotation 1693. The discrepancy between the formerly-identified events and the new count of 34 events arises from more-detailed examination of the data using image-difference and blink-comparison techniques on the images suggested by the streaks in Figure 6.6.3. This type of "second look" analysis was not used by Hundhausen *et al.*, intentionally; to retain consistency with the Skylab coronagraph analyses, they examined only the direct C/P images.

The tendency for transients to be clustered in time is not an artifact of the cadence of data acquisition; we used one coronagraph image (per sector) for each spacecraft orbit, even if more images are available. A notable example of temporal (ergo, spacial) clustering can be found on the west panel, near the equator, between days 102 and 106; Figure 6.6.4 shows a blowup of this area. The original pictures confirm the impression given by the map; there is a great concentration of coronal activity in this area, including at least five major mass ejections and much intermediary restructuring. This concentration of extreme coronal activity occurred above active regions which produced a large number of flares.

In Figure 6.6.3, coronal streamers are clearly visible as longitudinally extended brightness features. Comparison of the map with the heliospheric current sheet inferred by Hoeksema, Wilcox, and Scherrer (1983) suggests that the streamer-like features seen at 3 R_0 approximately outline the current sheet; further investigations of this correlation are in progress. The interaction of a CME with a streamer typically produces mostly a short-term change; the map shows that the large-scale structures basically return to their pre-event forms in about 6 hours or less. Even in such apparently violent events as that seen in the east frame at day 87, an event which extends over the entire east limb and strongly bends and displaces streamers, the long-term disruption is nil. It may be useful to distinguish two ways in which the brightness of observed coronal structures recovers to approximately its pre-event configuration. In the case of neighboring streamers which are obviously bent and displaced, recovery must be due to the relaxation of the CME-strained magnetic fields. The time scales involved are likely to be several hours, the approximate Alfven transit time across a coronal feature of length 1 R_0. Alternatively, in the case of longitudinally extended streamers, we are looking through long arcades; a part of the arcade may erupt, leaving the remainder of the overall structure nearly unaffected. In this case, the time scale for coronal recovery is more difficult to assess, since there can be a larger brightening due to rotation of the whole arcade blended with the smaller brightening due to "refilling" or recovery of the restricted region which erupted.

Of course, there are exceptions to enduring stability. The region of frequent restructuring (days 102-106) mentioned above suffers persistent brightening or the creation of several small streamers. On day 105, a large eruptive prominence-associated mass ejection occurred (in projection) over the north pole. The southwestern leg of the transient loop impinged on a pre-existing, fairly quiescent streamer; following this interaction, the streamer expanded in latitude and height and was the site of numerous additional coronal mass ejections over the next 5 days, as shown in Figure 6.6.4. Indeed, the original frames indicate that the streamer, in addition to the major coronal transients, underwent almost continous activity in the form of material outflows and frequent small changes of shape. This "activation" of the coronal (magnetic) structure persisted for about 3 days before the streamer "deflated" to nearly its pre-activation, day 105 size. Even after this relaxation, the area was the site of numerous mass ejections.

The map shows that the upper corona has a remarkable ability to "heal" itself and to recover in a few hours or a few days from the effects of strong disruptions. The day(s)-long recovery from disruption occurs in the context of slower evolution. Comparison between the east and west limb panels in Figure 6.6.3 shows that there is noticeable evolution of the corona during half a rotation, just as MacQueen and Poland (1977) found for the Skylab-era corona. Often, the streamer bands merely shift position somewhat, while keeping their major features intact. In contrast, the bright region on the east near the equator between days 84 and 88 has almost vanished by its west limb passage on days 98 to 102. Comparisons of this type between similar maps of successive rotations give the same conclusion; in 14 to 28 days, one-half to one solar rotation, there takes place considerable movement, appearance and disappearance of major features.

6.6.3.2 Coronal Variation From Rotation to Rotation

The detailed synoptic map of Figure 6.6.3 is not the most appropriate way to present coronal observations for study of the longest time scales of coronal evolution. The welter of detail tends to obscure those trends which are the object of investigation. In this section, we give only a glimpse of these trends.

Figure 6.6.5 shows a set of six SMM coronagraph frames taken at the central meridian passages of Carrington longitude 090° during the SMM mission in 1980. Each frame is a composite of three images of the north, east, and west quadrants. As usual, solar north is to the upper left, and east is to the lower left. The individual images were chosen to be free of CMEs. The dark stripes and spots are instrumental artifacts and should be ignored. There is no picture for rotation 1695.

Though coronal structure varies from rotation to rotation, there is also correlation from rotation to rotation. In each rotation, there is some bright streamer structure on the

ORIGINAL PAGE IS
OF POOR QUALITY

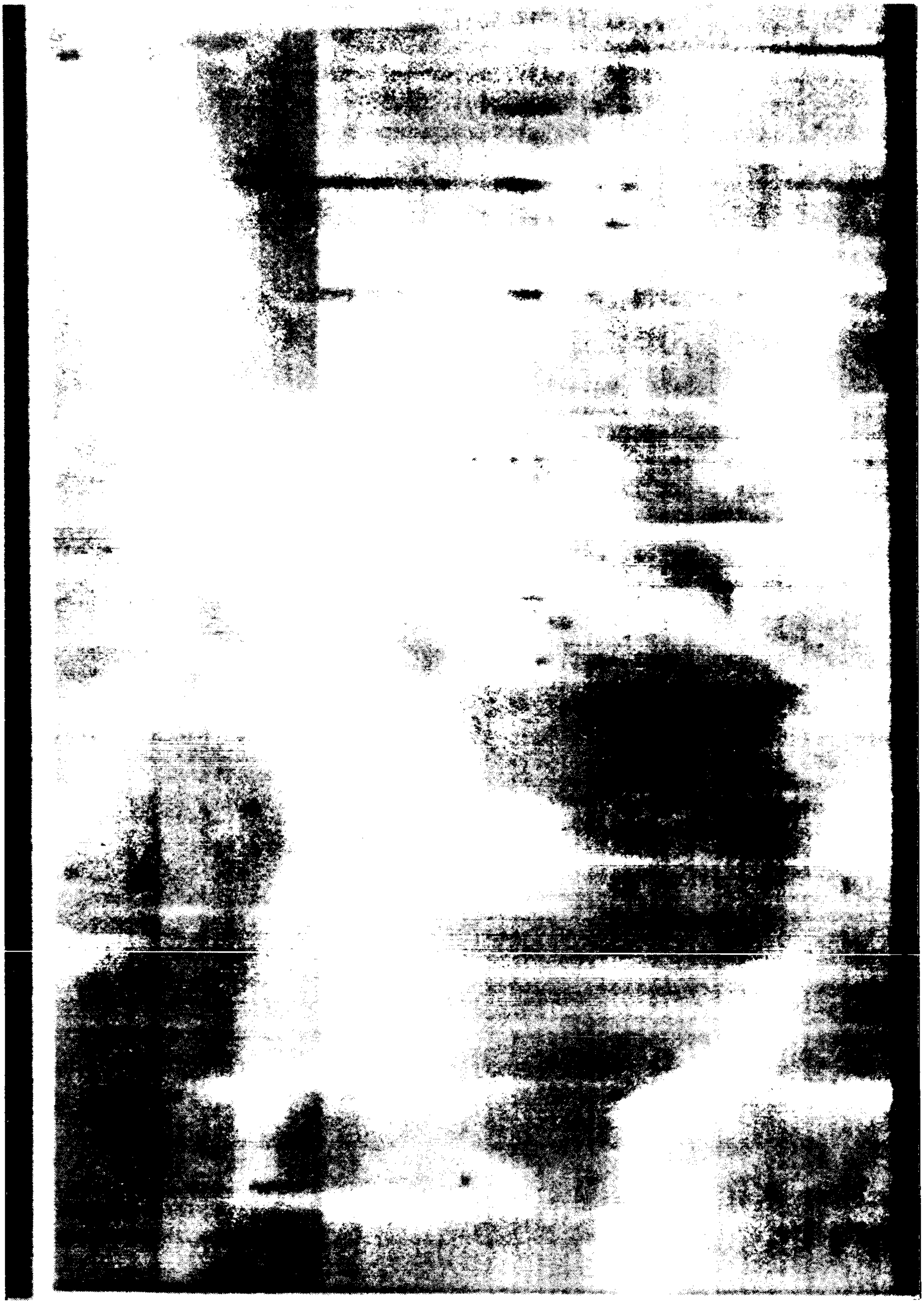

Figure 6.6.4 Expanded view of the coronal activity on days 102 to 106, from the detailed synoptic map of Figure 6.6.3.

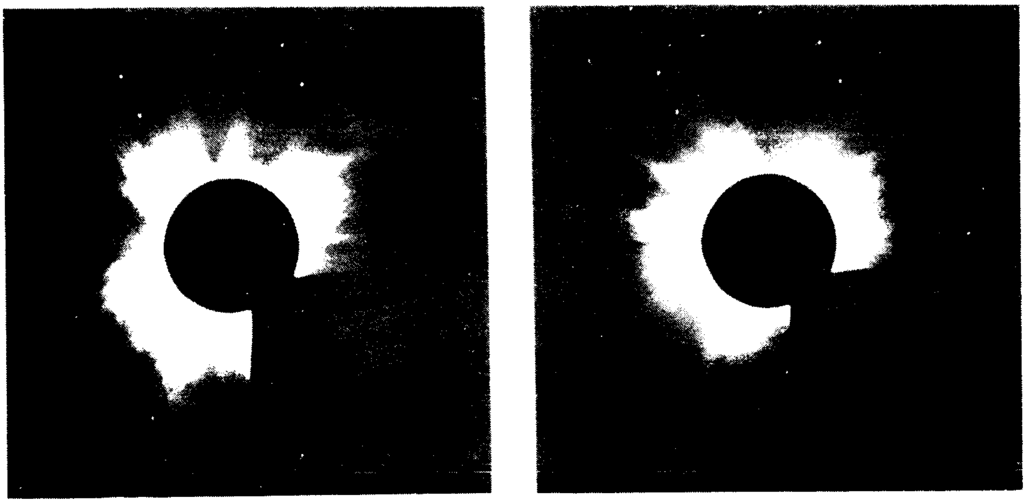

1693: 1545 UT, MARCH 25

1694: 0047 UT, APRIL 22

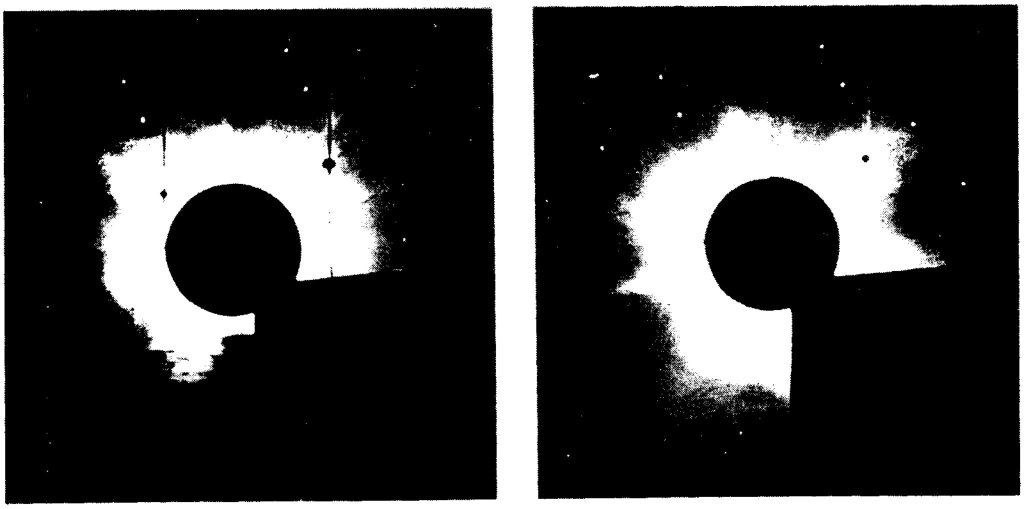

1696: 0803 UT, JUNE 15

1697: 1603 UT, JULY 12

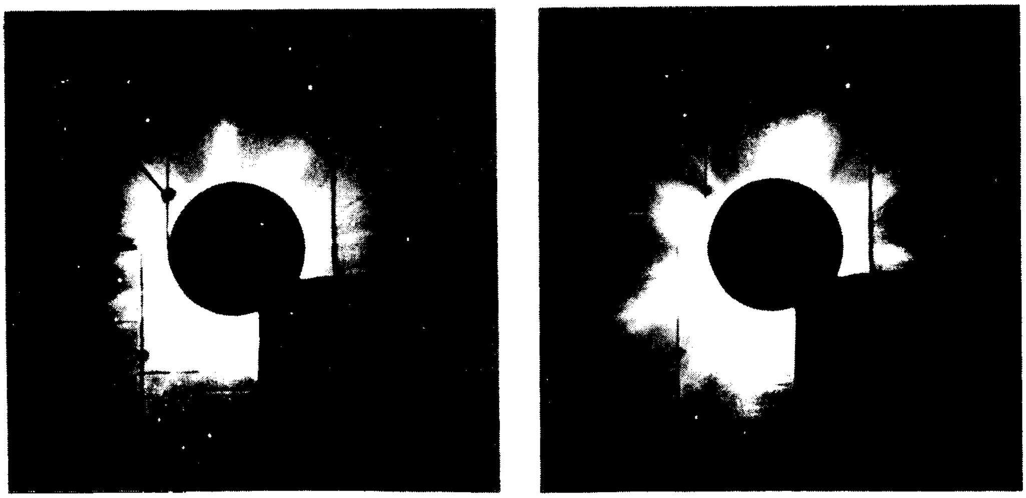

1698: 0225 UT AUGUST 9

1699: 0110 UT, SEPTEMBER 6

Figure 6.6.5 SMM coronagraph frames taken at 090° disk center Carrington longitude for five of the six rotations included in the 1980 SMM data.

east limb; though less evident on rotations 1694 and 1696, it becomes strong again in the following rotations. In each rotation, there is fairly bright structure near the north pole. The west is the most variable region, with prominent streamers disappearing and being replaced by other streamers at considerably different positions. Even though the detailed structure of the corona changes from one rotation to the next in Figure 6.6.5, the correlation of bright structure from rotation to rotation implies that the major, determining, magnetic features underlying the corona remain, at least on the north and east limbs.

The large-scale structure does not always correlate well in successive rotations. Figure 6.6.6 shows the corona as it appeared at central meridian passage of Carrington longitude 000° and as it appeared one rotation later. The north and east have almost no features in common between the two rotations and we interpret this as evidence for the occurrence of major change or disruption in the underlying magnetic structure. Comparative analysis of coronal changes with magnetic changes inferred from contemporaneous magnetograms is necessary to achieve complete understanding of these large scale phenomena.

From our still preliminary analyses we can draw the following conclusions about evolution of the SMM-era corona on temporal scales of a day or longer. The corona showed remarkable ability to recover to near pre-event configuration over times of a few days after violent disruption; this at the epoch of maximum solar activity. However, the coherence time for many of the largest features was short, approximately one solar rotation. Both these results are consistent with the results found by Hundhausen, Hansen, and Hansen (1981) in their analysis of K-coronameter observations of the lower corona over almost two full solar cycles.

6.7 SUMMARY

6.7.1 Introduction

The quantity and diversity of results presented in the preceding five sections of this chapter almost defy summarization. Yet, they are so voluminous as to demand an outline of some of the major achievements. Inevitably such a list is idiosyncratic and slights excellent work of extreme interest to some. In Section 6.7.2, we list — in very abbreviated form — some of the major conclusions and observations presented during the Workshop. Readers interested in more detail are referred to the appropriate subsection of this chapter. In the final portion of this section, we suggest future work to advance our understanding of the corona and its (slow and rapid) evolution.

6.7.2 Major Observations and Conclusions

The list which follows is a selection of the major observations and conclusions presented during the SMM Workshop. The reader is referred to the appropriate subsection of the chapter for more details and for references to published work regarding the listed items; the reader is referred to the entire chapter for many results which are not in this list of highlights. That the selected items preponderantly deal

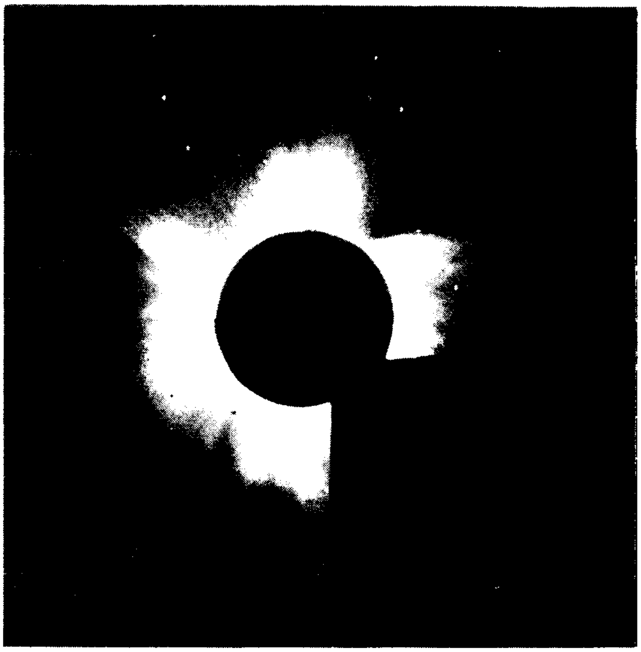

1696: 1743 UT, JUNE 7

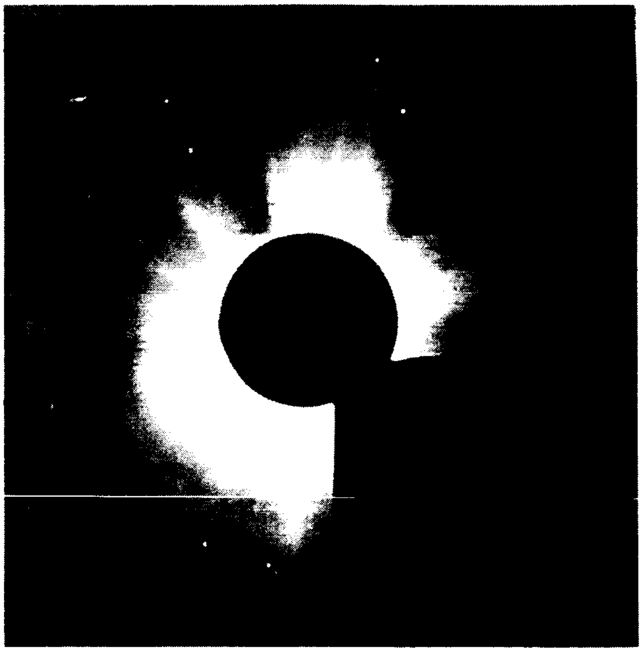

1697: 2243 UT, JULY 5

Figure 6.6.6 SMM coronagraph frames taken at 000° disk center Carrington longitude for rotations 1696 and 1697.

with coronal mass ejections reflects the interest of the majority of the team members in that phenomenon as observed in the corona. Not all of the members of the Team were exclusively interested in CMEs, so some results on other coronal topics are listed as well.

1. We have gathered together in one place comprehensive, multi-instrument descriptions of seven coronal mass ejection events. Detailed conclusions which follow from these collaboratively observed events are (Section 6.2.1.1-6.2.1.7):

(a) An example of the class of dark or depletion (at 1.2 R_0) transients was reported to acquire a bright rim as it rose through the corona. Thus, this depletion transient (perhaps the ascent of the cavity often seen around a prominence at the limb) became a bright coronal mass ejection in an orbiting coronagraph's field-of view. In this case, it is quite clear that the excess mass ejected from the orbiting coronagraph's field-of-view was not raised from the chromosphere but, rather, started in the corona (Section 6.2.1.1);

(b) In one event there is a strong suggestion of magnetic disconnection from the Sun; that is, there is a rising, outwardly concave, intensity-enhanced structure. Less obvious, but still suggestive, similar structures were seen in perhaps as many as 10 percent of all SMM events (Section 6.2.1.2);

(c) A CME which possibly resulted from the eruption of an *arcade* rather than a single loop was reported; a moving Type IV radio burst was associated with a denser blob of rising plasma; soft X-ray emission enhancement commenced 17 minutes before the earliest H-alpha activity; a forerunner similar to those reported for Skylab-era events surrounded the ejection (Section 6.2.1.7).

2. Observations with the Helios satellites' zodiacal light photometers enabled us to obtain "stereoscopic" views of three coronal mass ejections and to resolve some of the ambiguities which are inherent in observations from a single vantage point. The observations show that coronal mass ejections typically have a complicated 3-dimensional structure (Section 6.2.1.8; see also 6.5.2), a result supported by the SOLWIND coronagraph observations of "halo" CMEs which sometimes appear to surround the occulting disk completely (Section 6.2.2.2).

3. The long observing period of the SOLWIND coronagraph aboard the P78-1 satellite has enabled statistics to be gathered on more than a thousand CMEs occurring around the time of solar activity maximum (Figure 6.2.23). Aside from the broader range that might be expected when the sample size is increased by more than 100 times, the values of speed, mass, and energy are similar to those reported for Skylab-era CMEs, though the latitude of occurrences spread much higher (Section 6.2.2).

4. It was suggested that at least some coronal mass ejection events — with or without accompanying flares — start at a time coincident with weak, soft X-ray bursts. Such "precursory bursts" occur some minutes before the associated flare onset, if any (Section 6.3.2.2).

5. In some flares, both near disk center and at the limb, doppler shifts of Ca XIX or Fe XXV X-ray emission lines were seen briefly during the flares' impulsive phase. The observed magnitude of the doppler shift implies motion of 300-400 km s^{-1} toward the observer during the impulsive phases. The doppler shift and apparent velocity were too brief to be seen in low-cadence X-ray images, so the location of the phenomenon could not be related in detail to flare site morphologies (Section 6.3.3.2).

6. Rising, X-ray-emitting counterparts of whitelight coronal mass ejections were detected at low heights (e.g., 1.14 R_0). In one well-observed case, the X-ray emitting structure started to rise before the main X-ray flare occurred; it may have started at the time of an X-ray "precursory burst" as mentioned in item 3 (Sections 6.3.3.1 and 6.3.4).

7. Characteristically, coronal mass ejections associated with flares show rapid initial acceleration, usually followed by constant speed or deceleration. By contrast, coronal mass ejections associated with prominence eruptions tend to move more slowly and often are still accelerating at great heights in orbiting coronagraphs' fields-of-view (Section 6.4.1).

8. From a family of numerical model calculations, it was concluded that it is impossible to simulate a realistic coronal mass ejection by calculating the response of an atmosphere in hydrostatic equilibrium, permeated by an initially potential magnetic field, to a perturbing pressure pulse at its base (Section 6.4.2).

9. Self-similar solutions of the MHD equations were suggested as a good way to model the asymptotic behavior of coronal mass ejections far from their initiating sites (Section 6.4.3). Appropriate choice of the free parameters in the models appears to give good agreement with some observations (Section 6.2.1.2).

10. Gigantic post-flare coronal arches, emitting soft X-rays for several hours, were discovered after two-ribbon flares. Such flares typically have Type IV (and, often, Type II) radio bursts. In one case, the arch was stationary, but in another case of subsequent flares from the same active region, the post-flare coronal arches revived, brightening in place in X-ray emission, and rising at different speeds. The arches probably cooled radiatively, with inhibition of cooling by conduction. The relation of these arches to coronal mass ejection is unclear, due to a lack of data (Section 6.4.4).

11. The energy expected to be liberated by magnetic field reconnection and realignment to a potential configuration over a two-ribbon flare was examined analytically. Conservative assumptions about magnetic field strength and geometry yield an energy liberation some 300 times greater than what is needed to power an observed flare taken as an example. Therefore, it may be concluded that the magnetic field in the volume above and around a flare does not relax com-

pletely, that is, to a potential field; rather, it remains stressed after the flare is over (Section 6.4.5).

12. An axisymmetric, hydrostatic, equilibrium configuration (with two free configuration-changing parameters) was presented which allowed analytical examination of stability. Though stable against all axisymmetric perturbations, the equilibrium was — in every case — unstable against perturbations with variations along all three axes (Section 6.4.6).

13. Based on the observed association between meter-wave Type II bursts at the appropriate time and place and the later observations of interplanetary magnetic clouds, it was suggested that interplanetary magnetic clouds are the manifestations of coronal mass ejections at 1 AU (Section 6.5.2).

14. Observations (obtained with instruments aboard the Helios and other satellites) of the interplanetary consequences of coronal mass ejections were particularly rich (Section 6.5.3):

(a) Of 80 interplanetary shocks observed when Helios was within 30° of a solar limb and when the SOLWIND coronagraph was observing, 40 had good associations with coronal mass ejections, and another 19 of the shocks had possible coronal mass ejections. The mass ejections associated with the shocks at Helios were generally faster, brighter, and at lower latitude than the typical CME; they tended to fill an arc of heliocentric latitude in the corona which encompassed the Helios — Sun line;

(b) Of 27 prompt proton events with H-alpha flares which were observed, 26 had associated coronal mass ejections. The 27th event appears to be a member of a new class of events associated with short-lived flares having γ-ray and radio Type III bursts but no CME;

(c) By contrast, energetic particle events which were rich in ^{3}He (^{3}He/^{4}He >0.2 at ~ 1.5 MeV/nucleon) were *not* well associated with radio bursts or coronal mass ejections.

15. Though the topic was not intensively studied during the Workshop, it is possible to say a few words about coronal evolution during SMM (Section 6.6.2):

(a) On occasion, there were permanent changes in coronal structures due to coronal mass ejections;

(b) Sometimes, coronal structures endured for more than a day, even in the presence of repeated flaring below them;

(c) Often, there were changes which occurred over a period of hours. These are difficult to identify as coronal mass ejections, but they clearly involved at least the rearrangement and, possibly, the gradual expulsion of material;

(d) Type III storms tended to occur where the coronal structure appeared to be bundles of small, discrete rays;

(e) Generally, the corona was brighter after a radio noise storm than before; it was suggested that the eruption of new flux at the base of the corona created the proper conditions for the noise storm and carried relatively denser plasma laterally, and upward to greater heights as well, thereby brightening the corona.

16. The preparation of synoptic charts, which showed coronal brightness at one limb as an entire rotation brought 360 deg of longitude to the limb, gave a pseudo-image presentation of global coronal structure. This format allowed for the study of evolution and the association of coronal structures with other solar features such as the base of the heliospheric current sheet. The analysis of such displays was only begun during the Workshop (Section 6.6.3.1).

6.7.3 Suggestions for Future Research

As always happens in a vigorously advancing field, the observations and analyses reported by the Coronal Structures team members raised as many questions as they answered. The evolution of the corona and the relation between its structures and the underlying photospheric and chromospheric features has been a neglected area of study. The long series of SOLWIND coronagraph observations, the accumulating Mauna Loa Mark III K-Coronameter data, and the repaired SMM Coronagraph/Polarimeter instrument (now repaired and operating again at fairly rapid cadence) have given us the necessary observations to explore these questions. Another area begging for future investigation is the nature of the large-scale X-ray emitting structures, both the moving structures associated with visible light coronal mass ejections and the gigantic post-flare arches. The energy sources, the magnetic configurations, and the relation of these features to other forms of solar activity will lead to a substantially improved understanding of solar activity in the low corona.

The major issue still confronting us, an issue pointed up by the list of results given in Section 6.7.2, is the inadequacy of our present physical understanding of why and how coronal mass ejections occur. Both analytical and numerical modelling are as toddlers, ready to grow, to improve, and to become more realistic. Basically, we lack insight into the physics of the initiating processes of coronal mass ejection. Though we can be relatively successful at modelling a particular event, we do not possess an over-arching understanding of the causes and mechanisms which give rise to coronal mass ejections in the first place. During the Workshop, phenomena associated with CMEs were discovered which must be integrated into our conceptual picture. The relationship of post-flare arches must be considered. To be satisfactory, an overall picture must also accommodate the growing body of observations that coronal reconfiguration occurs on all time scales; should CMEs be distinguished from slightly slower reconfigurations, or are they just the more energetic members of the reconfiguration spectrum? Also, the discovery of soft X-ray pulses coincident with CME onsets, prior to flares, will affect our understanding of the initiation of coronal mass ejections. If the rapid movement of hot (Ca XIX and Fe XXV-emitting) plasma during the impulsive phase of flares is related to coronal mass ejections, that too will lead to deeper understanding.

It is widely believed that the magnetic field holds the key to understanding the observed structure of the corona and its variation. The radio observations give us our best hope to infer the strength of the magnetic field in the corona. These observations and their analyses should be pursued vigorously. Another type of observation, whose enormous value is only glimpsed as yet, is the "stereoscopic" examination of coronal mass ejections. The zodiacal light photometers aboard Helios were never intended for coronal mass ejection observations, but the CME-related information wrested from their records with great difficulty is intriguing and important, for it suggests that coronal mass ejections are not loop-like. Indeed, they are not even symmetric about a central axis, despite their frequent loop-like appearance when viewed in projection from ground-based and near-Earth vantage points. An instrument designed specifically to view coronal mass ejections traversing interplanetary space, sited to give a perspective far removed from Earth's, would yield data of exceptional value to our understanding of CME morphology and evolution. The interplanetary manifestations and consequences of coronal mass ejections are still a puzzle. Coronal mass ejections are often high-contrast disruptions of the pre-event corona, but in most cases they appear to be low-contrast perturbations of the 1 AU solar wind. The association between energetic coronal mass ejections and interplanetary shocks at Helios is encouraging, but it leaves unanswered the question of the appearance of the slower coronal mass ejections in the interplanetary medium. The association between coronal mass ejections and prompt proton events is understood not at all, nor is the lack of association between coronal mass ejections and ^{3}He-rich energetic particle events understood. It is tempting to think that the association (or lack of it) between CMEs and interplanetary particle events is a clue to the nature of energetic particle acceleration and release on the one hand and to the nature of CME initiation on the other.

6.8 ACKNOWLEDGEMENTS

With great pleasure, the editor of this chapter acknowledges and thanks the members of the Coronal Structures Team for their enthusiastic participation in the SMM Workshop and for their contributions which are reported here. The organizers of the chapter have been very helpful, even though it cost some of them considerable labor. The editor thanks S. W. Kahler and R. M. MacQueen for their reviews of an earlier draft of the chapter; their comments led to numerous improvements and modifications. To Ms. Leila Reed goes the editor's deepest appreciation for her exceptionally competent and cheerful clerical assistance through the long process of entry, revision, and subsequent re-revisions of the text of this chapter. Finally, thanks go to the SMM Principal Investigators, to the Workshop organizers, and to the Workshop's financial supporters; they brought the Workshop into existence and created the opportunity for such stimulating and fruitful interaction with colleagues engaged in similar research.

6.9 REFERENCES

Anzer, U.: 1980, in *Solar and Interplanetary Dynamics, IAU Symp. No. 91*, (eds., M. Dryer and E. Tandberg-Hanssen) (Reidel Publ. Co.: Dordrecht), p. 263.

Anzer, U., and Pneuman, G. W.: 1982, *Solar Phys. 79*, 129.

Barenblatt, G. I., and Zel'dovich, Ya. B.: 1972, *Ann. Rev. Fluid Mech. 4*, 285.

Bassi, J., Dulk, G. A., and Wagner, W. J.: 1985, in preparation.

Bentley, R. D., Lemen, J. R., Phillips. K. J. H., and Culhane, J. L.: 1984, *Solar Phys.* submitted.

Benz, A., and Wentzel, D. G.: 1981, *Astron. Astrophys.* 94, 100.

Bernstein, I. B., Friedman, E. A., Kruskal, M. D., and Kulsrud, R. M.: 1958, *Proc. Roy. Soc. Lon. A244*, 17.

Borrini, G., Gosling, J. T., Bame, S. J., and Feldman, W. C.: 1982, *J. Geophys. Res. 87*, 7370.

Cane, H. V.: 1984, *Astron. Astrophys. 140*, 205.

Cargill, P. J., and Priest, E. R.: 1982, *Solar Phys. 76*, 357.

Carrington, R. C.: 1859, *Monthly Not. Roy. Astron. Soc. 20*, 13.

Dryer, M.: 1982 *Space Sci. Rev. 33*, 233.

Dulk, G. A., Smerd, S. F., MacQueen, R. M., Gosling, J. T., Magun, A., Stewart, R. T., Sheridan, K. V., Robinson, R. D., and Jacques, S.: 1976, *Solar Phys. 49*, 369.

Dulk, G. A., and Suzuki, S.: 1980, *Astron. Astrophys. 88*, 203.

Duncan, R. A.: 1983, *Solar Phys. 89*, 63.

Fisher, R. R., Garcia, C. J., and Seagraves, P.: 1981, *Astrophys. J.* (Letters) *246*, L161.

Fisher, R. R., and Poland, A. I.: 1981, *Astrophys. J. 246*, 1004.

Fisher, R. R., Lee, R. H., MacQueen, R. M., and Poland, A. I.: 1981, *Appl. Opt. 20*, 1094.

Gary, D. E.: Radio emission from solar and stellar coronae. Ph.D. thesis, University of Colorado, 1982.

Gary, D. E., Dulk, G. A., House, L. L., Illing, R. M. E., Sawyer, C., Wagner, W. J., McLean, D. J., and Hildner, E.: 1984, *Astron. Astrophys., 134*, 222.

Gary, D. E., Dulk, G. A., House, L. L., Illing, R. M. E., Wagner, W. J., and McLean, D. J.: 1985, *Astron. Astrophys.*, submitted.

Gergely, T. E.: 1984, this workshop.

Gergely, T. E., Kundu, M. R., Erskine, F. T., III, Sawyer, C., Wagner, W. J., Illing, R. M. E., House, L. L., McCabe, M. K., Stewart, R. T., Nelson, G. J., Koomen, M. J., Michels, D., Howard, R., and Sheeley, N.: 1984, *Solar Phys. 90*, 161.

Gosling, J. T., Hildner, E., MacQueen, R. M., Munro, R. H., Poland, A. I., and Ross, C. L.: 1975, *Solar Phys. 40*, 439.

Gosling, J. T., Hildner, E., MacQueen, R. M., Munro, R. H., Poland, A. I. and Ross, C. L.: 1976, *Solar Phys. 48*, 389.

Gosling, J. T., Hildner, E., Asbridge, J. R., Bame, S. J., and Feldman, W. C.: 1977, *J. Geophys. Res. 82*, 5005.

Harrison, R. A., Simnett, G. M., Hoyng, P., LaFleur, H., and van Beek, H. F.: 1984, in *Proc. STIP Symposium on Solar-Interplanetary Intervals*, p. 287.

Harrison, R. A., Waggett, P. W., Bentley, R. D., Phillips, K. J. H., Bruner, M., Dryer, M., and Simnett, G. M.: 1985, *Solar Phys.*, submitted.

Heyvaerts, J., Priest, E. R., and Rust, D. M.: 1977, *Astrophys. J. 216*, 123.

Hildner, E.: 1977, in *Studies of Travelling Interplanetary Phenomena*, (eds., M. A. Shea *et al.*) p. 3.

Hildner, E., Gosling, J. T., MacQueen, R. M., Munro, R. H., Poland, A. I., and Ross, C. L.: 1975a, *Solar Phys. 42*, 163.

Hildner, E., Gosling, J. T., Hansen, T. R., Bohlin, J. D.: 1975b, *Solar Phys. 45*, 363.

Hildner, E., Gosling, J. T., MacQueen, R. M., Munro, R. H., Poland, A. I., Ross, C. L.: 1976, *Solar Phys. 48*, 127.

Hoeksema, J. T., Wilcox, J. M., Scherrer, P. H.: 1983, *J. Geophys. Res. 88*, 9910.

Howard, R. A., Michels, D. J., Sheeley, N. R., Jr., Koomen, M. J.: 1982, *Astrophys. J. 263*, L101.

Howard, R. A., Sheeley, N. R., Jr., Koomen, M. J., Michels, D. J.: 1984, in Advances in Space Research (Pergamon Press), ed. P. Simon, in press.

Howard, R. A.: 1984, private communication.

Howard, R. A., Sheeley, N. R., Jr., Koomen, M. J., and Michels, D. J.: 1985, *J. Geophys. Res.*, in press.

Hundhausen, J. R., Hundhausen, A. J. and Zweibel, E. G. 1981: *J. Geophys. Res. 86*, 11117.

Hundhausen, A. J., Hansen, R. T., Hansen, S. F.: 1981, *J. Geophys. Res. 86*, 2079.

Hundhausen, A. J., Sawyer, C. B., House, L., Illing, R. M. E., Wagner, W. J.: 1984a, *J. Geophys Res., 89*, 2639.

Hundhausen, A. J. *et. al.*: 1984b, in *Solar-Terrestrial Physics: Present and Future*, NASA Ref. Publ. 1120, eds. D. M. Butler and K. Papadopoulos, Chapter 6.

Illing, R. M. E.: 1984, *Astrophys. J. 280*, 399.

Illing, R. M. E., and Hundhausen, A. J.: 1983, *J. Geophys. Res.* 88, 10210.

Illing, R. M. E., Hundhausen, A. J., and Fisher, R. R.: 1985, in preparation.

Jackson, B. V.: 1981, *Solar Phys. 73*, 133.

Jackson, B. V., and Hildner, E.: 1978, *Solar Phys. 60*, 155.

Jackson, B. V., Howard, R. A., Sheeley, N. R., Jr., Michels, D. J., and Koomen, M. J.: 1985a, *Solar Phys.*, submitted.

Jackson, B. V., Howard, R. A., Sheeley, N. R., Jr., Michels, D. J., Koomen, M. J., and Illing, R. M. E.: 1985b, in preparation.

Jackson, B. V., and Leinert, C.: 1985, submitted to JGR.

Kahler, S. W.: 1982, *J. Geophys. Res. 87*, 3439.

Kahler, S. W., Hildner, E., van Hollebeke, M. A. I.: 1978, *Solar Phys. 57*, 429.

Kahler, S. W., Sheeley, N. R., Jr., Howard, R. A., Koomen, M. J., and Michels, D. J.: 1984a, *Solar Phys. 93*, 133.

Kahler, S. W., Sheeley, N. R., Jr., Howard, R. A., Koomen, M. J., Michels, D. J., McGuire, R. E., von Rosenvinge, T. T., and Reames, D. V.: 1984b, *J. Geophys. Res. 89*, 9683.

Kahler, S., Cliver, E. W., Sheeley, N. R., Jr., Howard, R. A., Koomen, M. J., Michels, D. J.: 1985a, *J. Geophys. Res. 90*, 177.

Kahler, S. W., Reames, D. V., Sheeley, N. R., Jr., Howard, R. A., Koomen, M. J., and Michels, D. J.: 1985b, *Astrophys. J.*, in press.

Kerdraon, A., Pick, M., Trottet, G., Sawyer, C., Illing, R., Wagner, W., House, L.: 1983, *Astrophys. J. 265*, L19.

Klein, L. W., and Burlaga, L. F.: 1982, *J. Geophys. Res. 87*, 613.

Kopp, R. A., and Pneuman, G. W.: 1976, *Solar Phys. 50*, 85.

Lantos, P.: 1984, in *Proc. International Workshop on Solar Physics and Interplanetary Travelling Phenomena*, Kunming, China, November 1983, in press.

Lantos, P., Kerdraon, A., Rapley, G. G., and Bentley, R. D.: 1981, *Astron. Astrophys. 101*, 33.

Lantos, P., and Kerdraon, A.: 1984, *Solar Phys.*, submitted.

Leinert, C., Link, H, Pitz, E., Salm, N., and Kuppelberg, D.: 1975, *Raumfahrtforschung 19*, 264.

Leinert, C., Pitz, E., Link, H., and Salm, N.: 1981, *J. Space Sci. Instr. 5*, 257.

Lin, R. P., and Hudson, H. S.: 1976, *Solar Phys. 50*, 153.

Low, B. C.: 1981, *Astrophys. J. 251*, 352.

Low, B. C.: 1982, *Astrophys. J. 254*, 796.

Low, B. C.: 1984a, *Astrophys. J., 281*, 392.

Low, B. C.: 1984b, *Astrophys. J., 286*, 772.

Low, B. C.: Munro, R. H., and Fisher, R. R. 1982, *Astrophys. J. 255*, 335.

Low, B. C., Munro, R. H., and Fisher, R. R.: 1982, *Astrophys. J. 254*, 335.

Low, B. C., Hundhausen, A. J., and Hu, Y. Q.: 1985, *J. Geophys. Res.*, submitted.

MacQueen, R. M.: 1980, *Phil. Trans. Roy. Soc. Lon. A297*, 605.

MacQueen, R. M., and Poland, A. I.: 1977, *Solar Phys. 55*, 143.

MacQueen, R. M., Csoeke-Poeckh, A., Hildner, E., House, L., Reynolds, R., Stanger, A., Tepoel, H., and Wagner, W.: 1980, *Solar Phys. 65*, 91.

MacQueen, R. M., and Fisher, R. R.: 1983, *Solar Phys. 89*, 89.

Martin, S. F., and Ramsey, H. E.: 1972, *Prog. Astronaut. Aeronaut. 30*, 371.

Maxwell, A., and Dryer, M.: 1982, Space Sci. Rev., *32*, 11.

McCabe, M. K., Svestka, Z., Howard, R. A., Jackson, B. V., and Sheeley, N. R., submitted to *Solar Phys.*

Melrose, D. B.: 1980, *Solar Phys. 67*, 357.

Michalitsanos, A. G., and Kupferman, P.: 1974, *Solar Phys. 36*, 304.

Moore, R. L., McKenzie, D. L., Svestka, Z., Widing, K. G., Krieger, A. S., Mason, H. E., Petrasso, R. D., Pneuman, G. W., Silk, J. K., Vorpahl, J. A., and Withbroe, G. L.: 1980, in *Solar Flares*, Skylab Solar Workshop II Monograph (ed., P. A. Sturrock) (Colorado Assoc. University Press: Boulder), p. 341.

Munro, R. H., Gosling, J. T., Hildner, E., MacQueen, R. M., Poland, A. I., and Ross, C. L.: 1979, *Solar Phys. 61*, 201.

Nolte, J. T., Gerassimenko, M. Krieger, A. S., Petrasso, R. D., and Svestka, Z.: 1979, *Solar Phys. 62*, 123.

Pallavicini, R., Serio, S., and Vaiana, G. S.: 1977 *Astrophys. J. 216*, 108.

Pallavicini, R., and Vaiana, G. S.: 1980, *Solar Phys. 67*, 127.

Parker, E. N.: 1958, *Astrophys. J. 128*, 664.

Parker, E. N.: 1963, *Interplanetary Dynamical Process* (Interscience: New York).

Payne-Scott, R., Yabsley, D. E., and Bolton, J. G.: 1947, *Nature 160*, 697.

Pick, M., Trottett, G., MacQueen, R. M.: 1980, *Solar Phys. 63*, 369.

Pneuman, G. W.: 1980, in *Solar Flare Magnetohydrodynamics* (ed., E. Priest).

Pneuman, G. W.: 1982, *Solar Phys. 78*, 229.

Pneuman, G. W.: 1983, *Solar Phys. 88*, 219.

Reames, D. V., and von Rosenvinge, T. T.: 1983, *in Proc. 18th Int. Cosmic Ray Conf. (Bangalore) 4*, p. 48.

Richter, I., Leinert, C., and Planck, B.: 1982, *Astron. Astrophys. 110*, 115.

Rosner, R., Low, B. C. and Holzer, T. E.: 1984, in *Physics of the Sun* (eds., P. A. Sturrock, T. E. Holzer, and D. Michels) (to be published by the National Academy of Science).

Rust, D., and Hildner, E.: 1976, *Solar Phys. 48*, 381.

Rust, D. M., and Webb, D. F.: 1977, *Solar Phys. 54*, 403.

Rust, D. M., Hildner, E., Dryer, M., Hansen, R. T., McClymont, A. N., McKenna-Lawlor, S. M. P., McLean, D. J., Schmahl, E. J., Steinolfson, R. S., Tandberg-Hanssen, E., Tousey, R., Webb, D. F. and Wu, S. T.: 1980, in *Solar Flares*, Skylab Solar Workshop II Monograph (ed., P. A. Sturrock) (Colorado Assoc. University Press: Boulder), p. 273.

Saito, K., Poland, A. I., and Munro, R. H.: 1977, *Solar Phys. 55*, 121.

Sawyer, C., Wagner, W. J., House, L. H., and Illing, R. W.: 1984, *J. Geophys. Res.*, in preparation.

Schmahl, E., and Hildner, E.: 1977, *Solar Phys. 55*, 473.

Sheeley, N. R., Bohlin, J. D., Brueckner, G. E., Purcell, J. D., Scherrer, V. E., Tousey, T., Smith, J. B., Speich, D. M., Tandberg-Hanssen, E., Wilson, R. M., deLoach, A. C., Hoover, R. B., and McGuire, J. P.: 1975, *Solar Phys. 45*, 377.

Sheeley, N. R., Jr., Howard, R. A., Michels, D. J., Koomen, D. J.: 1980, in IAU Symp. 91, *Solar and Interplanetary Dynamics*, Dryer and Tandberg-Hanssen, eds., D.-Reidel.

Sheeley, N. R., Jr., Stewart, R. T., Robinson, R. D., Howard, R. A., Koomen, M. J., Michels, D. J.: 1984, *Astrophys. J., 279*, 839.

Sheeley, N. R., Jr., Howard, R. A., Koomen, M. J., Michels, D. J.: 1983a, *Astrophys. J., 272*, 349.

Sheeley, N. R., Jr., Howard, R. A., Koomen, M. J., Michels, D. J., Schwenn., R., Muhlhauser, K. H., and Rosenbauer, H.: 1983b, in *Solar Wind Five*, (ed., M. Neugebauer) NASA Conf. Publ. 2280, p. 693.

Sheeley, N. R., Jr., Howard, R. A., Koomen, M. J., Michels, D. J., Schwenn, R., Muhlhauser, K. H., and Rosenbauer, H.: 1985, *J. Geophys. Res. 90*, 163.

Sime, D. G., MacQueen, R. M., and Hundhausen, A. J.: 1984, *J. Geophys. Res. 89*, 2113.

Simnett, G. M., and Harrison, R. A.: 1985, *Solar Phys.*, in press.

Stewart, R. T., Dulk, G. A., Sheridan, K. V., House, L. L., Wagner, W. J., Sawyer, C., Illing, R.: 1982, *Astron. Astrophys., 116*, 217.

Stewart, R. T.: 1983, private communication.

Stewart, R. T.: 1984, *Solar Phys., 94*, 379.

Sturrock, P. A., and Smith, S. M.: 1968, *Solar Phys. 5*, 87.

Svestka, Z.: 1976, in *Solar Flares*, (Reidel Publ. Co.: Dordrecht) p. 241.

Svestka, Z.: 1983, *Space Sci. Rev. 35*, 259.

Svestka, Z.: 1984, *Solar Phys. 94*, 171.

Svestka, Z., and Fritzova-Svestkova, L.: 1974, *Solar Phys. 36*, 417.

Svestka, Z., Martin, S. F., and Kopp, R. A.: 1980, in *Solar and Interplanetary Dynamics, IAU Symp. 91*, (eds., M. Dryer and E. Tandberg-Hanssen), p. 216.

Svestka, Z., Stewart, R. T., Hoyng, P., van Tend, W., Acton, L. W., Gabriel, A. H., Rapley, C. G., and 8 co-authors: 1982a *Solar Phys. 75*, 305.

Svestka, Z., Dodson-Prince, H. W., Martin, S. F., Mohler, O. C., Moore, R. L., Nolte, J. T., and Petrasso, R. D.: 1982b, *Solar Phys. 78*, 271.

Tousey, R.: 1973, The solar corona, in *Space Research XIII*, (eds., M. J. Rycroft and S. K. Runcorn) (Akademie-Verlag: Berlin) p. 713.

Trottet, G., and MacQueen, R. M.: 1980, *Solar Phys. 68*, 177.

Trottet, G., Pick, M., House, L., Illing, R., Sawyer, C., Wagner, W.: 1982 *Astron. Astrophys. 111*, 306.

Uchida, Y., and Low, B. C.: 1981, *J. Ap. Astr. 2*, 405.

van Beek, H. F., Hoyng, P., LaFleur, H., and Simnett, G. M.: 1980, *Solar Phys. 65*, 39.

Wagner, W. J.: 1983, *Adv. Space Sci.* 2, 203.

Wagner, W. J.: 1984, Ann. Rev. of Astron. and Astrophys., *22*, 267.

Wagner, W. J., Hildner, E., House, L. L., Sawyer, C., Sheridan, K. V., and Dulk, G. A.: 1981, *Astrophys. J. Letters 244*, L123.

Wagner, W. J., and MacQueen, R. M.: 1983, *Astron. Astrophys.*, *120*, 36.

Wang, S., Hu, Y, Q, and Wu, S. T.: 1982, Scientia Sinica (Series A) *25*, 1305.

Webb, D., Krieger, A. S., and Rust, D. M.: 1976, *Solar Phys. 48*, 159.

Webb, D. F., and Kundu, M. R.: 1978, *Solar Phys. 57*, 155.

Webb, D. F., Cheng, C.-C., Dulk, G. A., Edberg, S. J., Martin, S. F., McKenna-Lawlor, S., and McLean, D. J.: 1980, in *Solar Flares*, (ed., P. A. Sturrock) (Colorado Assoc. University Press: Boulder) p. 471.

Webb, D. F., and Hundhausen, A. J.: 1985, JGR, in preparation.

Weiss, A., A.: 1963, *Australian J. Phys. 16*, 240.

Wild, J. P., Roberts, J. A., and Murray, J. D.: 1954, *Nature 173*, 532.

Wilson, R. M., and Hildner, E.: 1984, *Solar Phys. 91*, 169.

Wolfson, R. L. T.: 1982, *Astrophys. J. 255*, 774.

Wu, S. T., Wang, S., Dryer, M., Poland, A. I., Sime, D. G., Wolfson, C. J., Orwig, L. E., and Maxwell, A.: 1983, *Solar Phys. 85*, 351.

Wu, S. T., Wang, S., Hu, Y. Q., Michels, D. J., Howard, R., and Sheeley, N.: 1985. *Astrophys. J.*, to be submitted.